Recent trends and variability in the oceanic storage of dissolved inorganic carbon

Lydia Keppler[1], Peter Landschützer[2], Siv K Lauvset[3], and Nicolas Gruber[4]

[1]Scripps Institution of Oceanography
[2]Flanders Marine Institute (VLIZ)
[3]NORCE Norwegian Research Centre
[4]ETH Zürich

December 21, 2022

Abstract

\justify Several methods have been developed to quantify the oceanic accumulation of anthropogenic carbon dioxide (CO$_2$) in response to rising atmospheric CO$_2$. Yet, we still lack a corresponding estimate of the changes in the total oceanic dissolved inorganic carbon (DIC). In addition to the increase in anthropogenic CO$_2$, changes in DIC also include alterations of natural CO$_2$. Once integrated globally, changes in DIC reflect the net oceanic sink for atmospheric CO$_2$, complementary to estimates of the air-sea CO$_2$ exchange based on surface measurements. Here, we extend the MOBO-DIC machine learning approach by \citeA{keppler_mapped_2020} to estimate global monthly fields of DIC at 1° resolution over the top 1500 m from 2004 through 2019. We find that over these 16 years and extrapolated to cover the whole global ocean down to 4000 m, the oceanic DIC pool increased close to linearly at an average rate of 3.2$\pm$0.7 Pg C yr^{-1}. This trend is statistically indistinguishable from current estimates of the oceanic uptake of anthropogenic CO$_2$ over the same period. Thus, our study implies no detectable net loss or gain of natural CO$_2$ by the ocean, albeit the large uncertainties could be masking it. Our reconstructions suggest substantial internal redistributions of natural oceanic CO$_2$, with a shift from the mid-latitudes to the tropics and from the surface to below $\sim$200 m. Such redistributions correspond with the Pacific Decadal Oscillation and the Atlantic Multidecadal Oscillation. The interannual variability of DIC is strongest in the tropical Western Pacific, consistent with the El Ni$\tilde{n}$o Southern Oscillation.

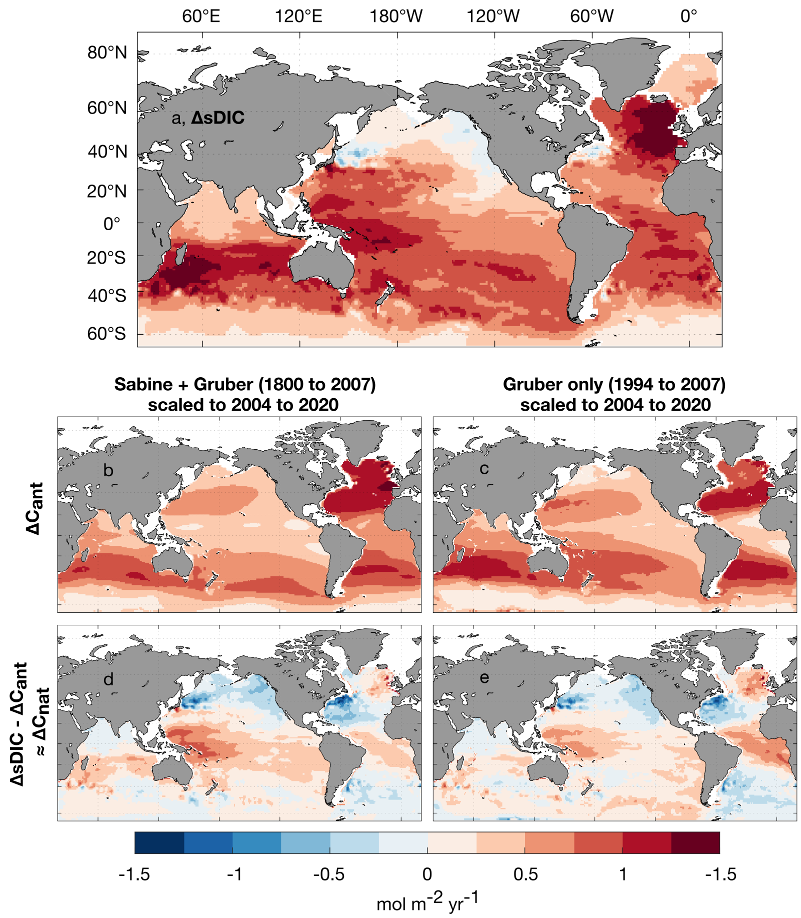
60°E
120°E
180°W
120°W
60°W
0°
80°N
60°N
40°N
20°N
0°
20°S
40°S
60°S
a, ΔsDIC
Sabine + Gruber (1800 to 2007)
scaled to 2004 to 2020
Gruber only (1994 to 2007)
scaled to 2004 to 2020
ΔCant
b
c
ΔsDIC - ΔCant
≈ ΔCnat
d
e
-1.5
-1
-0.5
0
0.5
1
-1.5
mol m-2 yr-1

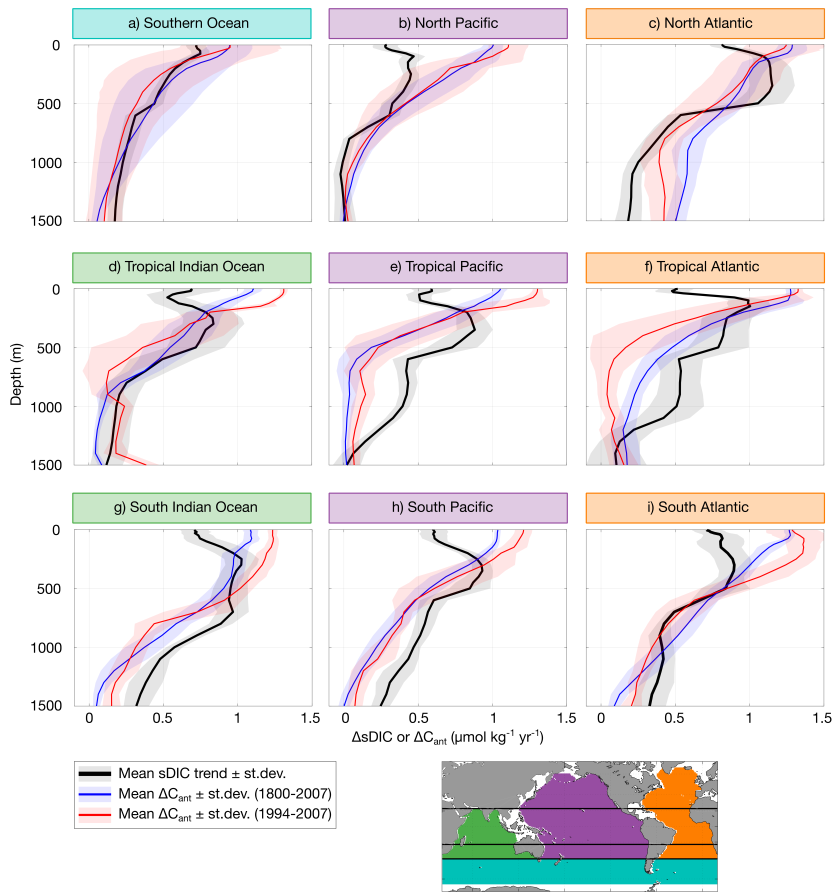
a) Southern Ocean
b) North Pacific
c) North Atlantic
d) Tropical Indian Ocean
e) Tropical Pacific
f) Tropical Atlantic
g) South Indian Ocean
h) South Pacific
i) South Atlantic
Depth (m)
0
500
1000
1500
0.5
1
1.5
ΔsDIC or ΔC_{ant} (μmol kg^{-1} yr^{-1})
Mean sDIC trend ± st.dev.
Mean ΔC_{ant} ± st.dev. (1800-2007)
Mean ΔC_{ant} ± st.dev. (1994-2007)

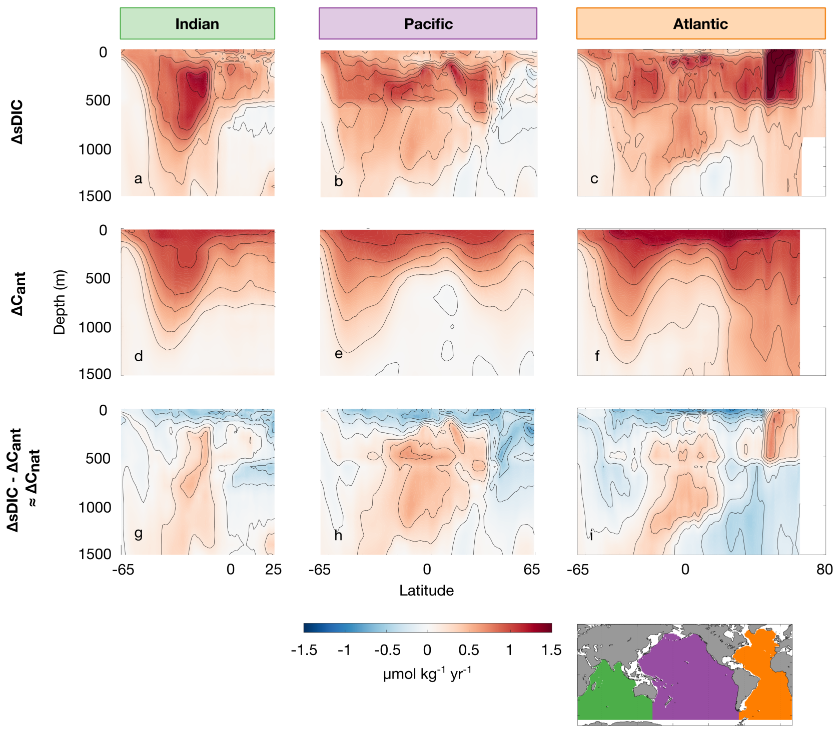

Indian
Pacific
Atlantic
ΔsDIC
ΔC_ant
ΔsDIC - ΔC_ant ≈ ΔC_nat
Depth (m)
0
500
1000
1500
a
b
c
d
e
f
g
h
i
-65
0
25
65
80
Latitude
-1.5
-1
-0.5
0.5
1
1.5
μmol kg^-1 yr^-1

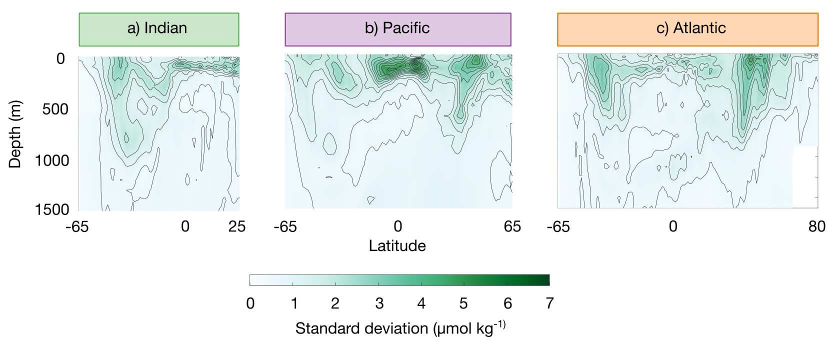

a) Indian
b) Pacific
c) Atlantic
Depth (m)
0
500
1000
1500
-65
0
25
65
80
Latitude
0
1
2
3
4
5
6
7
Standard deviation (μmol kg^-1)

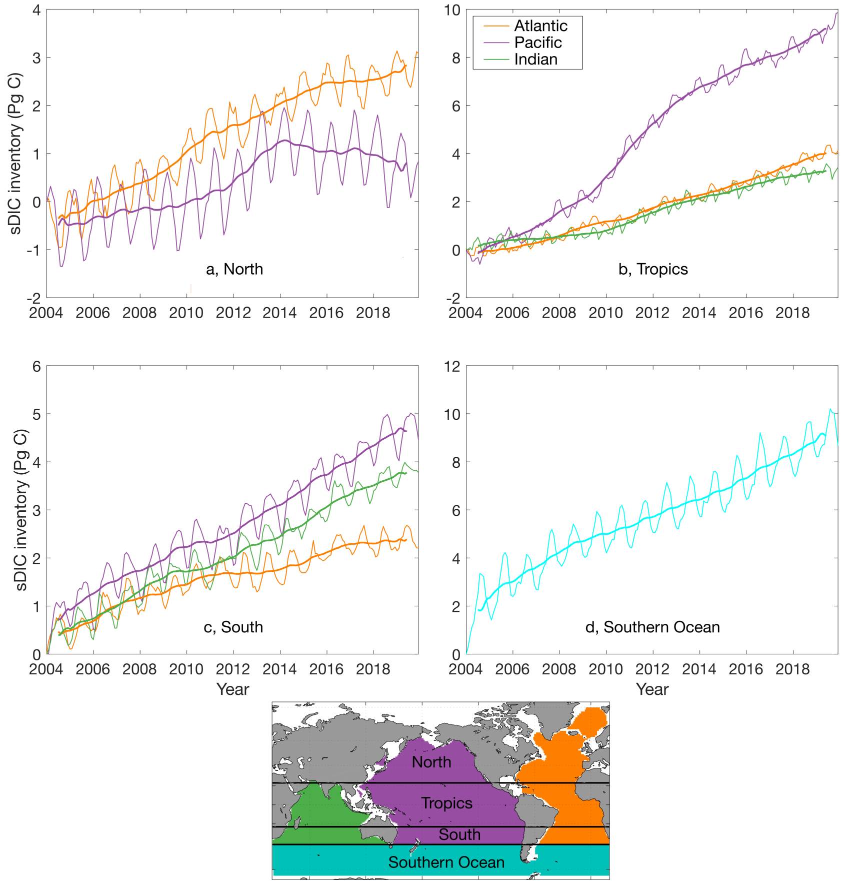

Compared data set	Type of data	Bias (μmol kg^{-1})	RMSD (μmol kg^{-1})	MOBO-DIC uncertainty (μmol kg^{-1})	Comparison uncertainty (μmol kg^{-1})
GLODAPv2.2021	Ship data, without interpolation or mapping (used to train the network)	0	16	18	2
Lauvset climatology	Global climatology (optimal interpolation)	7	17	18	7
Broullón climatology	Global monthly climatology (single-step neural network)	10	17	18	N/A
MOBO-DIC$_{clim}$	Global monthly climatology (cluster-regression)	11	20	18	9
HAMOCC	Synthetic data	-1	12	18	N/A
BATS	Time-series station	12	17	17	2
HOT	Time-series station	-4	15	17	2
Drake Passage	Time-series station (surface)	16	42	18	1
SOCCOM floats	Calculated DIC from BGC floats (pH) with LIAR algorithm	-5	14	17	6
OceanSODA-ETHZ	Global surface estimate (cluster-regression)	4	15	18	21

	Compared data set → / Depth ↓	BATS	MOBO-DIC at BATS	HOT	MOBO-DIC at HOT	Drake Passage (surface)	MOBO-DIC at Drake Passage	SOCCOM floats	MOBO-DIC at SOCCOM floats
Trend	20 – 40 m	1	7	5	2	8	1	-20	-9
	100 – 150 m	3	8	13	6	N/A	N/A	3	1
	600 -800 m	16	5	4	5	N/A	N/A	19	26
IAV	20 – 40 m	5	2	11	4	9	5	4	3
	100 – 150 m	4	2	6	2	N/A	N/A	2	2
	600 -800 m	4	1	3	1	N/A	N/A	3	3

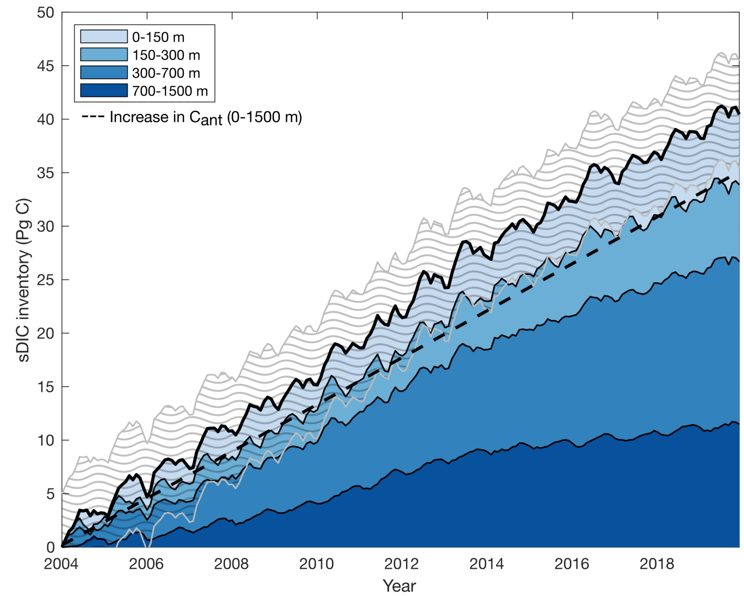

Recent trends and variability in the oceanic storage of dissolved inorganic carbon

L. Keppler[1,2,3], P. Landschützer[2,4], S.K. Lauvset[5], N. Gruber[6]

[1]Scripps Institution of Oceanography, University of California San Diego, La Jolla, CA, USA
[2]Max Planck Institute for Meteorology, Hamburg, Germany
[3]International Max Planck Research School on Earth System Modelling, Hamburg, Germany
[4]Flanders Marine Institute (VLIZ), Ostend, Belgium
[5]NORCE Norwegian Research Centre, Bjerknes Centre for Climate Research, Bergen, Norway
[6]Environmental Physics, Institute of Biogeochemistry and Pollutant Dynamics, ETH Zurich, Zurich, Switzerland

Key Points:

- From 2004 through 2019, the global oceanic dissolved inorganic carbon (DIC) pool increased at an average rate of 3.2±0.7 Pg C yr^{-1}
- Most of this increase is associated with the uptake of anthropogenic CO_2, while natural CO_2 is mostly redistributed within the ocean
- The interannual variability of DIC is largest in the tropical Pacific Ocean

Corresponding author: Lydia Keppler, lkeppler@ucsd.edu

Abstract

Several methods have been developed to quantify the oceanic accumulation of anthropogenic carbon dioxide (CO_2) in response to rising atmospheric CO_2. Yet, we still lack a corresponding estimate of the changes in the total oceanic dissolved inorganic carbon (DIC). In addition to the increase in anthropogenic CO_2, changes in DIC also include alterations of natural CO_2. Once integrated globally, changes in DIC reflect the net oceanic sink for atmospheric CO_2, complementary to estimates of the air-sea CO_2 exchange based on surface measurements. Here, we extend the MOBO-DIC machine learning approach by Keppler et al. (2020a) to estimate global monthly fields of DIC at 1° resolution over the top 1500 m from 2004 through 2019. We find that over these 16 years and extrapolated to cover the whole global ocean down to 4000 m, the oceanic DIC pool increased close to linearly at an average rate of 3.2±0.7 Pg C yr^{-1}. This trend is statistically indistinguishable from current estimates of the oceanic uptake of anthropogenic CO_2 over the same period. Thus, our study implies no detectable net loss or gain of natural CO_2 by the ocean, albeit the large uncertainties could be masking it. Our reconstructions suggest substantial internal redistributions of natural oceanic CO_2, with a shift from the mid-latitudes to the tropics and from the surface to below ∼200 m. Such redistributions correspond with the Pacific Decadal Oscillation and the Atlantic Multidecadal Oscillation. The interannual variability of DIC is strongest in the tropical Western Pacific, consistent with the El Niño Southern Oscillation.

1 Introduction

The global oceanic dissolved inorganic carbon (DIC) pool is a powerful recorder of changes in the net exchange of carbon dioxide (CO_2) across the air-sea interface, i.e., the strength of the net oceanic carbon sink. This net sink is the sum of a flux of natural carbon that reflects the exchange driven by changes in solubility, ocean circulation, mixing, and biological processes, and the flux of anthropogenic carbon that corresponds to the anomalous flux of CO_2 driven by the human-induced rise in atmospheric CO_2 (McNeil & Matear, 2013; Gruber et al., 2023). When integrated globally, the sources and sinks of natural CO_2 fluxes cancel each other out in a steady state as the ocean strives towards equilibrium with the overlaying atmosphere (Landschützer et al., 2022). On the contrary, the observed increase in the net air-sea CO_2 exchange is caused by anthropogenic CO_2 emissions, (Friedlingstein et al., 2022). An important exception is residual outgassing that reflects the balance between the input of carbon by rivers and the deposition of carbon on the seafloor (Sarmiento & Sundquist, 1992; Regnier et al., 2022). As long as this balance is maintained, this latter (i.e., natural) component does not leave an imprint on changes in DIC, so that changes in this pool are then directly attributable to the ocean interior accumulation or loss of both natural and anthropogenic CO_2.

Knowing the magnitude of the net oceanic sink for CO_2 is crucial for closing the global carbon budget and its anthropogenic perturbation (Sarmiento & Gruber, 2002; Friedlingstein et al., 2022). The need is heightened by efforts such as the United Nations' global stocktake efforts (`https://unfccc.int/topics/science/workstreams/global-stocktake`), which require a more refined estimate of the changing ocean carbon content, connecting the surface and interior ocean, and demonstrating the total changes in DIC, as well as its spatial distribution. Finally, better global-scale constraints on the changes in oceanic DIC are of great interest to better document the progression of ocean acidification and better establish the connection between changes in seawater chemistry and biological impacts (Doney et al., 2009; Orr et al., 2005; Feely et al., 2004).

In terms of observations, the net oceanic CO_2 sink is at present primarily determined using observations of the surface ocean partial pressure of CO_2 (pCO_2), which are mapped to the globe using various data interpolation methods (Landschützer et al., 2014; Rödenbeck et al., 2015; Fay et al., 2021; Gregor & Gruber, 2021). The mapped pCO_2 is then used, in combination with the atmospheric pCO_2 and the gas transfer velocity, to estimate the air-sea CO_2 flux. However, this approach is subject to various uncertainties, such as data sparsity (Fay & McKinley, 2013), an ill-constrained gas transfer coefficient (Wanninkhof et al., 2009; Roobaert et al., 2019), and a potential offset in the pCO_2 measurements as they are not directly taken at the cool skin surface (Watson et al., 2020). Furthermore, the steady-state outgassing of river-derived carbon needs to be subtracted from the inferred flux to obtain the anthropogenic flux relevant to the global carbon budget. Estimates for this riverine flux range from 0.23 Pg C yr^{-1} (Lacroix et al., 2020) and 0.45±0.18 Pg C yr^{-1} (Jacobson et al., 2007) to 0.78±0.41 Pg C yr^{-1} (Resplandy et al., 2018), with the most recent review by Regnier et al. (2022) suggesting a value of 0.65±0.3 Pg C yr^{-1}. This range and the associated uncertainties add further uncertainty to the pCO_2 derived estimates of the net carbon uptake by the global ocean.

Confidence in quantifying this net uptake could be strengthened if constrained independently through the direct determination of changes in the global ocean DIC content. Nevertheless, this is a challenging task, owing to the sparsity of observations, the substantial background DIC pool of ∼37,000 Pg C (Keppler et al., 2020b), and the many physical and biological processes that govern the distribution of DIC in the ocean (Sarmiento & Gruber, 2006). A very successful approach to overcome this challenge has been to only focus on the interior ocean's accumulation of the anthropogenic CO_2 (C_{ant}) component (Wallace, 1995; Tanhua et al., 2007). Under the assumption that either the ocean is in a near steady state or that the contribution of natural carbon (C_{nat}) to global-scale changes in DIC is small, several methods have been developed to determine the changes in C_{ant} either from single surveys of DIC (Brewer, 1978; Chen & Millero, 1979; Gruber et al., 1996), or from repeat hydrography programs (Friis et al., 2005; Clement & Gruber, 2018; Carter et al., 2019). The application of these methods has permitted the oceanographic community to quantify the increase in the C_{ant} inventory, both since preindustrial times (Gruber, 1998; Sabine et al., 1999) and for the past few decades (Friis et al., 2005; Wanninkhof et al., 2010; Carter et al., 2019), with the global studies providing invaluable constraints for the global budget of C_{ant} (Sabine et al., 2004; Gruber et al., 2019).

Although these global C_{ant} estimates have proven to be extremely valuable for constraining the global carbon budget and hence the fate of the emitted anthropogenic CO_2, they have not been able to fully address whether the steady-state assumption or the assumption of a small natural CO_2 signal is justified. Questions were raised early on, especially in the context of ocean warming (Keeling, 2005; Sabine & Gruber, 2005), which many models suggest will lead to a loss of CO_2 from the ocean (Joos et al., 1999; Sarmiento et al., 1998; Matear & Hirst, 1999). Later, using a combination of different model and observation-based methods, McNeil and Matear (2013) invoked the presence of a decadal-scale outgassing signal of natural CO_2, but without being able to support this conjecture with direct observations. Dedicated modeling studies also suggest that the ocean might have lost natural CO_2 in recent decades, e.g., in response to the trends in the Southern Annular Mode (Le Quéré et al., 2007; Lenton & Matear, 2007; Zickfeld et al., 2007; Hauck et al., 2013; Lovenduski et al., 2008, 2007). In their global study on the increase in anthropogenic CO_2 between 1994 and 2007, Gruber et al. (2019) speculated that perhaps as much as 5 Pg C of natural CO_2 might have been lost from the ocean over this period. Conversely, enhanced lateral transport of natural carbon from the land could yield a gain of C_{nat} in the ocean (Regnier et al., 2022). Similarly, changes in the circulation or biological productivity could cause an anomalous uptake or release of CO_2 from the atmosphere, altering the total stock of C_{nat}.

As the arguments for potential changes in C_{nat} accumulate, the need to constrain the changes in the total DIC pool increases, as this permits to assess the changes in both natural and anthropogenic CO_2. When doing so, one needs to also consider that even if the global-scale changes in the natural CO_2 pool might be small, this pool is subject to strong redistributions within the ocean, associated with changes in circulation, shifts in ocean fronts, and changes in biological productivity, causing locally large changes in DIC (Clement & Gruber, 2018). Such changes are commonly seen when comparing the DIC distributions between two occupations of a particular hydrographic section (Wanninkhof et al., 2010; Carter et al., 2019). They are also expected in the context of interannual variability, especially in regions with large vertical undulations of the thermocline, and hence also the "carbocline," i.e., the strong vertical gradient in DIC. Such redistributions of DIC within the ocean not only pose a challenge for the detection of global-scale changes in the DIC pool, but they also potentially threaten organisms, as spatial redistributions of DIC might cause more rapid local changes in ocean acidification and, perhaps, a more rapid reaching of critical thresholds (McNeil & Sasse, 2016).

Currently, no sensor technology exists that can operationally measure DIC in situ. Thus, we must rely on physical seawater samples collected and analyzed during ship-based surveys and programs (Talley et al., 2016; Bates et al., 2014), strongly limiting the coverage and the sampling frequency. Most of these DIC measurements and the associated ancillary data are compiled and subjected to secondary quality control by the Global Ocean Data Analysis Project (GLODAP; Olsen et al. (2016); Key et al. (2004)). A recent version (GLODAPv2.2021) contains over one million measurements from across the global ocean, spanning measurements from 1972 to 2020 (Lauvset et al., 2021). Most of the measurements contained within GLODAP stem from repeat hydrography programs, where the same set of stations along long lines are revisited at roughly decadal intervals (Talley et al., 2016). In addition to GLODAP, some long-term time-series stations provide information on the temporal variability in the interior ocean at a few locations, including the Hawaii Ocean Timeseries (HOT; Dore et al. (2009)) and the Bermuda Atlantic Timeseries Study (BATS; Bates et al. (2014)). More recently, Argo floats equipped with biogeochemical (BGC) sensors that measure pH, salinity, and other variables, supplement the ship data. Using these float measurements and some empirical relationships to infer alkalinity, DIC can be estimated (Carter et al., 2018; van Heuven et al., 2011). However, this method has much larger uncertainties than the ship data (Bittig et al., 2018), and to date, the available BGC-Argo float data are largely limited to the Southern Ocean, as part of the Southern Ocean Carbon and Climate Observations and Modelling project (SOCCOM, Talley et al. (2019)), while the global ocean BGC-Argo array is still in its early stages (Bittig et al., 2019).

In parallel to the efforts in combining and unifying carbon cycle observations (Olsen et al., 2016; Bakker et al., 2016), a second branch related to big data analysis based on machine learning has emerged. Keppler et al. (2020b) adopted a cluster-regression approach previously applied to reconstruct the air-sea CO_2 exchange (Landschützer et al., 2013, 2014) and extended it to map a monthly climatology of DIC in the upper 2000 m of the near-global ocean, i.e., Mapped Observation-Based Oceanic DIC (MOBO-DIC, Keppler et al. (2020a)). Similarly, Broullón et al. (2020) developed a single-step machine learning approach to map the monthly climatology of interior DIC at a global scale. In addition, a recent study has mapped out the temporal evolution of DIC globally (Gregor & Gruber, 2021), but this approach was limited to the documentation of variations at the sea surface. These studies revealed the feasibility of reconstructing the DIC content from observations at the global scale. In addition, using CMIP6 models and synthetic Argo data, Turner et al. (2022) demonstrated very recently that interior temperature and salinity data are well suited to reconstruct interior DIC fields and their variability. However, they have not yet mapped the interior ocean DIC with real-world Argo observations. Further, Sharp et al. (2022) successfully mapped monthly fields of interior ocean dissolved oxygen at a global scale, using a machine learning approach. However, mapped estimates of interior observation-based DIC remain limited to seasonal climatologies (Keppler et al., 2020b; Broullón et al., 2020) or the surface (Gregor & Gruber, 2021), and reconstructions of the trend and interannual variability of the upper ocean total DIC at the global scale based on direct observations are still lacking.

To fill this gap, we use the MOBO-DIC approach and extend the monthly climatology of DIC by Keppler et al. (2020b) to resolve monthly global DIC fields from 2004 through 2019 (i.e., January 2004 through December 2019). The temporal extent of our reconstructions is primarily determined by the availability of temperature and salinity fields from the Argo program that we use as key predictors. Our new DIC product is mapped at a monthly resolution on a 1°x1° grid, from 65°N to 65°S, and reaching 80°N in the Atlantic (see Supporting Information Fig. S1), extending from 2.5 m to 1500 m depth. Subsequently, we investigate the trend and interannual variability of the interior oceanic DIC at a global scale and put these changes into the context of the ongoing accumulation of anthropogenic CO_2 in the ocean's interior and from this, infer the changes in the natural CO_2 pool.

2 Data and Methods

2.1 Cluster-regression

We adopt the two-step neural network MOBO-DIC approach introduced by Keppler et al. (2020b) to map the sparse DIC observations to the (near) global ocean at monthly resolution for the period January 2004 through December 2019. Here, we present a summary of the most important features and the main changes compared to the climatological approach taken by Keppler et al. (2020b). Our approach first clusters the ocean into regions of similar properties using self-organizing maps (SOM) and then applies a feed-forward neural network (FFN) in each cluster to reconstruct a physical relationship between a set of driver variables and the target DIC data. This cluster-regression approach does not require information about the measurement location, a feature that separates it from many other mapping approaches (Sasse et al., 2013; Gregor et al., 2017; Bittig et al., 2018; Broullón et al., 2019, 2020). Thus, our regression method is solely based on the physical and biogeochemical relations between the predictor and target variables. Not using the measurement location as a predictor permits our method to benefit from information obtained in other places within each cluster, where predictor and target data are similarly related. Due to data availability and the presence of different processes near the surface and below, we run the method separately for two depth slabs: from 2.5 m to 500 m and from 500 m to 1500 m. We take the mean of the two estimates at 500 m to minimize boundary problems between the two depth slabs. This approach does not eliminate all discontinuities, but they are well within the uncertainty limits of the method.

In the first step, we use a SOM, i.e., a type of unsupervised machine learning, to determine clusters. Following Keppler et al. (2020b), we use six clusters in the upper 500 m and four between 500 m and 1500 m. This number of clusters leads to the smallest overall error in the DIC reconstruction. To avoid boundary problems inherent in cluster-regression approaches, we adjust the original method by creating an ensemble of SOM clusters, following the approach introduced by Gregor and Gruber (2021). To this end, we performed the SOM-step three times, where the DIC input has a different weight ranging from 2 to 4 in each run. The resulting SOM clusters vary mostly around the boundaries (see Supporting Information Fig. S2). In the second step, we run an FFN for each SOM cluster. Our FFN network architecture consists of 8 neurons in the hidden layer of the FFN, as this setup results in the most robust output based on a comparison between the mapped output and the original training data.

To avoid overfitting, we use 80% of the input data to train the network and the remaining 20% for internal cross-validation. As the training and validation data are separated randomly, the output from the FFN is slightly different each time it is run. For each SOM setup, we run the FFN five times, where each time, the data is separated differently into training and validation data to create an ensemble of outputs. Thus, our ensemble comprises 15 members (three SOM setups, each with five FFN runs). The final reported data are the mean across the ensemble, and the standard deviation across the ensemble (hereafter ensemble spread) represents the uncertainty linked to the weighting of the SOM clusters and the random assignment of training and validation data. We smooth the ensemble mean fields at each depth level by taking the running mean with a window size of three grid cells in each horizontal direction (latitude and longitude) and in the temporal dimension.

Some runs produced outputs with unlikely values, e.g., considerably larger or smaller than the measured variables in GLODAP. We attribute this to the random assignment of training and validation data, where some data subsets are unsuitable for training. Such runs with unlikely values occurred both with the GLODAP training data and with synthetic data, so it cannot be attributed to noise in the observations. We have tried many different setups of the network to eliminate this issue. However, with the current training data, we were unable to resolve it. Thus, when an output results in values that are more than 5 standard deviations larger or smaller than the observed data in GLODAP (i.e., outside of the range 1639 to 2575 μmol kg^{-1} and 1898 to 2629 μmol kg^{-1}, for the upper and lower depth slab, respectively), the entire ensemble member was discarded and re-run with the same setup, but with a different sub-set of training data. We trust that removing the runs with unlikely values, in addition to the bootstrapping approach, yields a robust estimate.

2.2 Data and Domain

As input to the SOM, we use monthly mapped fields of temperature and salinity based on Argo float measurements (Roemmich & Gilson, 2009) and an annual-mean climatology of DIC (Lauvset et al., 2016). We weigh the DIC input stronger than the physical predictors so that the clusters largely represent the climatological mean DIC and, to a lesser extent, the physical water masses, following Landschützer et al. (2013).

For the FFN step, we use the ship measurements of DIC from GLODAPv2.2021 between January 2004 and December 2019 (Lauvset et al., 2021) as the target data. We only retain GLODAP data with a WOCE quality control of 0 or 2 and a secondary quality control flag of 1. As predictors, we use the same Argo-based temperature and salinity fields that we used during the SOM step. In addition, we use monthly climatologies of mapped dissolved oxygen, nitrate, and silicic acid from the World Ocean Atlas 2018 (WOA18; Boyer et al. (2018)). These climatologies are based on ship measurements from 1955 through 2017 and were interpolated to the global ocean using optimal interpolation. As the nitrate and silicic acid from WOA only extend until 500 m, they were not used as predictors in the deeper slab, while dissolved oxygen extends to 1500 m in WOA and is thus a predictor variable in both depth slabs. Deviating from the approach taken to produce the monthly climatology of MOBO-DIC (Keppler et al., 2020b), we use atmospheric pCO_2 as an additional predictor in the upper depth slab (0 to 500 m) to be able to represent the long-term trend in the atmospheric CO_2 concentration. Atmospheric pCO_2 at each grid cell was computed from the GlobalView marine boundary layer product of the mole fraction of CO_2 (xCO_2; GlobalView-CO2 (2011)) and converted to pCO_2 following Landschützer et al. (2013). In the deeper slab below 500 m, we use Julian days as a predictor to represent any long-term trend in the data. Thus, the predictors between the surface and 500 m are temperature, salinity, dissolved oxygen, nitrate, silicic acid, and atmospheric pCO_2. Between 500 m and 1500 m, we use temperature, salinity, dissolved oxygen, and Julian day as predictors. A more detailed discussion on the choice of predictors can be found in Keppler et al. (2020b).

Note that we use the mapped monthly mean fields as predictors, as opposed to the co-measured data from GLODAP during the training step of the FFN. We tested both approaches but found the results were very noisy when using the co-measured data as predictors. This noisy output may be partially caused by the WOA monthly gridded fields being smoother than the point measurements in GLODAP. Furthermore, using the co-measured predictors leads to a substantial loss of training data, as in ∼60,000 data points out of ∼440,000 (i.e., ∼14%), and the training data do not have usable co-measured predictors.

The availability of the data limits the domain and resolution of our mapping approach. For example, we limit the vertical extent of the multi-year product here to 1500 m (as opposed to 2000 m used for the MOBO-DIC climatology) as the DIC observations are very sparse below 1500 m and only temperature and salinity are available as physical or biogeochemical predictors there. This lack of predictors below 1500 m prevents a robust estimate of the DIC variations and trends at these depths. Temporally and spatially, the limits tend to be set by the predictor data. The Argo-based data products used here extend from 65°N to 65°S globally, to 80°N in the Atlantic Ocean, with shallow coastal regions being masked, marking the horizontal extent of our domain. As the mapped Argo-dataset starts in 2004, and GLODAPv2.2021 includes cruise data until January 2020, the temporal extent of MOBO-DIC is from January 2004 through December 2019.

All predictors have a monthly resolution on 1°x1° grids, and we interpolate them onto 28 uneven depth levels between 2.5 m and 1500 m. Note that due to an update to the Argo data, the domain of this study is slightly larger than in the monthly climatology of MOBO-DIC (Keppler et al., 2020b): it extends further north in the Atlantic (until 80°N instead of 65°N), and some more coastal and shallow regions are included (see Supporting Information Fig. S1). As the domain covers most of the global ocean, we refer to our domain as global in-text but want to note that it is technically only near-global.

2.3 Calculation of the trend and inventory changes

We estimate the trend in DIC over our period based on the slope of a linear regression of the deseasonalized DIC at each grid cell. The data were deseasonalized by applying a 12-month running mean at each grid cell. To calculate the trends in the inventories, we first normalize DIC for salinity (hereafter sDIC) to remove any effects from potential changes in the salinity, following Friis et al. (2003). For this normalization, we use the same monthly Argo-based salinity product as above (Roemmich & Gilson, 2009), using the temporal mean salinity from 2004 through 2019 at each grid cell as reference salinity. We convert sDIC from gravimetric (unit: μmol kg^{-1}) to volumetric (unit: μmol m^{-3}), and then vertically integrate the volumetric trend in the whole domain (upper 1500 m). To estimate the uncertainty in the trend, we calculate it with each of the 15 ensemble members and take the standard deviation range as the uncertainty range. Note that the uncertainty of the trend only includes the ensemble spread (i.e., the prediction uncertainty) and does not consider other sources of error, for example, those associated with measurements or representation uncertainty. We trust that there should not be a trend in measurement or representation uncertainty in the data, yielding a robust estimate of the overall trend uncertainty. We then conduct an upscaling to estimate the global changes in sDIC that includes regions beyond our domain, i.e., the high latitudes, coastal regions, and below 1500 m (see Supporting Information S3).

2.4 Comparison with C_{ant}

We compare the trend in MOBO-DIC with an estimate of the change in anthropogenic CO_2 (ΔC_{ant}). For this comparison, we use two estimates of C_{ant} and scale them to our study period. The two estimates are (i) the total change in C_{ant} between 1800 and 2007 and (ii) the change in C_{ant} between 1994 and 2007. The former is estimated by adding the total C_{ant} up to 1994 estimated by Sabine et al. (2004) to the change in C_{ant} between 1994 and 2007 estimated by Gruber et al. (2019). For the latter, we use the ΔC_{ant} by Gruber et al. (2019).

To scale C_{ant} to our period, we apply the transient steady-state approach described by Mikaloff Fletcher et al. (2006) and Gruber et al. (2019), which relies on the assumption that the change in C_{ant} scales with the change in atmospheric CO_2:

$$\Delta C_{ant}^{t_3-t_2} = \alpha(t_0,t_1,t_2,t_3) \cdot \Delta C_{ant}^{t_1-t_0} \tag{1}$$

where t_0 and t_1 are the bounds of the periods used to determine ΔC_{ant} (either 1800 through 2006 or 1994 through 2006) and t_2 and t_3 bound the period to which the scaling should be applied to (here: 2004 through 2019). The scaling factor α is specific for each pair of periods, i.e., is a function of t_0, t_1, t_2, and t_3, and can be estimated from the relative changes in atmospheric CO_2, also considering changes in the Revelle factor (Sarmiento et al., 1995) and the changes in the air-sea disequilibrium (Gruber et al., 1996; Matsumoto & Gruber, 2005):

$$\alpha(t_0,t_1,t_2,t_3) = \frac{\Delta_t pCO_2^{atm}(t_3-t_2)}{\Delta_t pCO_2^{atm}(t_1-t_0)} \cdot \frac{\xi(t_2..t_3)}{\xi(t_0..t_1)} \cdot \frac{\gamma(t_2..t_3)}{\gamma(t_0..t_1)} \tag{2}$$

where the first factor on the right-hand side is the relative change in atmospheric CO_2, the second factor is the relative change in the disequilibrium ξ, and the third factor is the relative change in the Revelle factor γ.

In the first case, i.e., for the base period 1800 through 2006, inserting the observed values in atmospheric CO_2 in the respective years ($t_0 = 1800$, 280 ppm; $t_1 = 2006$, 381 ppm; $t_2 = 2004$; 377 ppm, $t_3 = 2019$, 410 ppm) gives a value of 0.33 for the first factor on the right-hand side of Eq. 2. For the disequilibrium, we take the same estimate Gruber et al. (2019) used when scaling from 1800 through 1993 to 1994 through 2006. They estimated a change in the disequilibrium of about 6 μatm between 1800 and 1994, and about 3 μatm between 1994 and 2007, yielding a ratio of 0.94. Similarly, we also take the estimate by Gruber et al. (2019) of 0.94 for the third factor, i.e., the ratio of the Revelle factors. Entering these three ratios, we obtain an overall scaling factor α of 0.29 ($0.33 \cdot 0.94 \cdot 0.94$) when comparing the period 1800 to 2007 with the period from 2004 through 2019.

In the second case, the base period for the scaling factor goes from 1994 (t_0, 358 ppm) through 2006 (t_1, 381 ppm), yielding a relative change in atmospheric CO_2 of 1.45 compared to the period 2004 (t_2, 377 ppm) through 2019 (t_3, 410 ppm). As the two periods are largely overlapping in this case, we assume that the ratio of the disequilibrium and the ratio of the Revelle factors are very close to 1 and thus set their values to 1, yielding an overall scaling factor α of 1.45 when comparing the period 1994 to 2007 with the period from 2004 through 2019.

This scaling is based on many assumptions, especially the assumption of a transient steady-state. While the large-scale distribution of C_{ant} has been demonstrated to follow this prediction rather closely, Gruber et al. (2019) pointed out that the reconstructed distribution of the change in C_{ant} between 1994 and 2007 differs in a few places considerably from that reconstructed for the period up to 1994. In particular, they found a meridional shift in the accumulation within the Atlantic Ocean, with a reduction in the North Atlantic storage being compensated by an increase in the temperate latitudes of the South Atlantic. Using two different base periods, we attempt to quantify the potential impact of such changes on our conclusions. Direct estimates of the accumulation of C_{ant} over the same period as analyzed here would be preferable to our scaling approach but are not published to date.

3 Uncertainty Assessment

3.1 Calculation of the overall uncertainty

We identify three main sources of uncertainties that contribute to the total uncertainty of our DIC estimate, following Gregor and Gruber (2021): the uncertainties linked to the measurements (M), the representation (R), and the prediction (P). The overall uncertainty of our DIC estimate (DIC_{err}) can then be estimated with standard error propagation:

$$DIC_{err} = \sqrt{M^2 + R^2 + P^2} \tag{3}$$

The uncertainty M linked to the measurements stems from sampling errors and imprecisions in the measurement system. While GLODAP currently does not report measurement uncertainties, they include a measure of spatial consistency based on inter-cruise comparisons, which amounts to 2.4 μmol kg^{-1} for DIC (Lauvset et al., 2021). We assume that this uncertainty is the same at all grid points.

The representation uncertainty R results from the fact that the discrete measurements in GLODAPv2.2021 that are used as target data to train the network are taken at one point in time and space and thus might not represent the true monthly mean of the 1°x1° grid cell and the depth bin it falls in. Especially problematic are regions where the spatiotemporal variability is high and the number of observations in a grid cell and depth bin is low. It is not straightforward to quantify the representation error as this requires full knowledge of the spatiotemporal variability of DIC. Gregor and Gruber (2021) estimated the representation error of total alkalinity of about 16 μmol kg^{-1} at the sea surface of the open ocean. As the density and spatial distribution of total alkalinity and DIC measurements in GLODAP are similar, and regions with high spatiotemporal variability in total alkalinity tend to be regions of high variability in DIC as well, we adopt this estimate for all grid cells and depth bins. The representation error is expected to be larger near the coast than in the open ocean due to more variability near the coasts and is also expected to decrease with depth(Torres et al., 2021), adding some uncertainty to our uncertainty estimate.

The prediction uncertainty P represents how well our method can map DIC in time and space. We take the standard deviation across the 15-member ensemble of our bootstrapping approach as our estimate of the prediction error. The differences in the ensemble members are linked to both the ensemble of SOM clusters and the different subsets of training and validation data, as described in Section 2.1. The global mean prediction uncertainty is 7 μmol kg^{-1}, but with a large spread. We find the highest prediction error in the northern Indian Ocean (up to $\sim$80 μmol kg^{-1}), where the observations are particularly sparse and where our estimate is heavily extrapolated (Supporting Information Fig. S3). Such large local uncertainties illustrate that our approach can reconstruct global fields, but care must be taken when evaluating regional changes, as the uncertainties on a regional level are quite high. Combining the three uncertainty contributions (Eq. 3) yields an overall global mean uncertainty of 18 μmol kg^{-1}.

3.2 Quality of fit

During our mapping approach, we estimate the target data at all grid points. Thus, unlike in an interpolation, there is a difference between the target data (i.e., GLODAPv2.2021) and the mapped estimate (i.e., MOBO-DIC). In Supporting Information Fig. S4, we present these residuals to get a better handle on the quality of our fits. This analysis intends to examine if there are any systematic offsets in different regions of depth levels. It also highlights the magnitude of the differences between the training data and MOBO-DIC. We find that there is no systematic under- or overestimation compared to the training data, and the global mean bias cancels out to be 0, while the global mean root mean square difference (RMSD) is 16 μmol kg^{-1} (see Table 1 and Supporting Information Fig. S4), slightly less than our global mean uncertainty of 18 μmol kg^{-1}.

4 Evaluation

We evaluate the quality of the mapped MOBO-DIC product with various independent observations and using a synthetic dataset derived from a model for which we know the true value. Independence means here that these data were not used for the training of MOBO-DIC.

To evaluate our method with the synthetic data, we subsample the simulated DIC in the biogeochemical component of the Ocean General Circulation Model HAMOCC (Ilyina et al., 2013; Mauritsen et al., 2019) when and where we have observations in GLODAPv2.2021. We then run our MOBO-DIC method with these synthetic data to reconstruct the simulated DIC fields. We can then compare our reconstructed fields with the actual DIC in HAMOCC. For a more detailed description of the evaluation with synthetic data, see Supporting Information S6.1.

For the observations, we use three different sources: First, we use a suite of mapped DIC climatologies, all of which are based on GLODAP data (Lauvset et al., 2016; Keppler et al., 2020b; Broullón et al., 2020). Second, we compare MOBO-DIC with observations from time-series stations and biogeochemical Argo floats. Third, we use the mapped surface DIC product contained in OceanSODA-ETHZ (Gregor & Gruber, 2021), allowing us to compare the monthly 1°x1° fields at the surface when and where the two datasets overlap (January 2004 to December 2018).

We first evaluate the climatological mean, then the trend, and the interannual variability, for each of these evaluation data where the temporal resolution allows. Note that we use DIC and not sDIC in the evaluation with observations, as salinity is not always co-measured, and using monthly 1-degree gridded salinity fields could introduce errors. In contrast, our comparison of synthetic MOBO-DIC and the HAMOCC model uses sDIC, as here we have both salinity and DIC as monthly 1-degree gridded fields. For a more in-depth analysis of the evaluation, see Supporting Information S6, and for a summary, see Table 1.

4.1 Evaluation of climatological mean

The evaluation of the MOBO-DIC method with the synthetic data from HAMOCC illustrates that the method is well-equipped to reconstruct the mean DIC fields in HAMOCC well (see Table 1). MOBO-DIC reconstructs the simulated climatological mean DIC fields with a negligible bias of -1 μmol kg^{-1} and with an RMSD of 12 μmol kg^{-1}.

The evaluation with the observational climatological constraints also reveals good performance of MOBO-DIC. The mean differences relative to the MOBO-DIC, Lauvset, and Broullón climatologies, are between 7 and 11 μmol kg^{-1}, with an RMSD of 17 to 20 μmol kg^{-1}. This is within the combined uncertainties of the MOBO-DIC and the comparison data sets (see Table 1 and Supporting Information Fig. S5 and S6). It also needs to be noted that the Lauvset climatology is normalized to the year 2002, while the Broullón monthly climatology is normalized to 1995, and the MOBO-DIC monthly climatology by Keppler et al. (2020b) is centered around the years 2010/2011. In comparison, this study is centered around 2012. Thus, the positive biases compared to these climatologies may largely stem from the differences in the period and the increase in anthropogenic carbon in the ocean.

The bias between MOBO-DIC and the comparison data sets from time-series stations and floats ranges from -5 to 16 μmol kg^{-1}. As the biases are both positive and negative, there is no indication of MOBO-DIC having a systematic bias towards over/underestimating the global carbon content (see Table 1 and Supporting Information Fig. S9 and S10). The RMSD between MOBO-DIC and these data range from 14 μmol kg^{-1} for the SOCCOM floats to 42 μmol kg^{-1} for Drake Passage but are mostly between 15 and 20 μmol kg^{-1}, i.e., comparable to the mean global uncertainty of MOBO-DIC (18 μmol kg^{-1}). In all cases except for Drake Passage, the RMSD is within the combined uncertainties of MOBO-DIC at the location of the compared data set and the uncertainty of the compared data set, using standard error propagation. The disagreement at Drake Passage, a well-observed time-series

Table 1. Summary of the bias and RMSD between MOBO-DIC and the comparison data sets. Also displayed are the mean uncertainty of MOBO-DIC at the time and location of the compared data set and the uncertainty of the comparison data sets.

Compared data set	Type of data	Bias (µmol kg^{-1})	RMSD (µmol kg^{-1})	MOBO-DIC uncertainty (µmol kg^{-1})	Comparison uncertainty (µmol kg^{-1})
GLODAPv2.2021	Ship data, without interpolation or mapping (used to train the network)	0	16	18	2
Lauvset climatology	Global climatology (optimal interpolation)	7	17	18	7
Broullón climatology	Global monthly climatology (single-step neural network)	10	17	18	N/A
MOBO-DIC$_{clim}$	Global monthly climatology (cluster-regression)	11	20	18	9
HAMOCC	Synthetic data	-1	12	18	N/A
BATS	Time-series station	12	17	17	2
HOT	Time-series station	-4	15	17	2
Drake Passage	Time-series station (surface)	16	42	18	1
SOCCOM floats	Calculated DIC from BGC floats (pH) with LIAR algorithm	-5	14	17	6
OceanSODA-ETHZ	Global surface estimate (cluster-regression)	4	15	18	21

station, is associated with large local variabilities that are not captured in MOBO-DIC and are further discussed in Section 4.3.

Comparing MOBO-DIC at the surface with the surface DIC from OceanSODA-ETHZ, we find that the magnitude and spatial patterns of the mean DIC agree very well, considering they are based on independent data (SOCAT pCO_2 vs. GLODAP DIC; Bakker et al. (2016); Lauvset et al. (2021)). The global mean RMSD between the two data sets is 15 μmol kg^{-1}, and there is a mean bias of approximately 4 μmol kg^{-1}, which is well within the uncertainties (see Table 1 and Supporting Information Fig. S11 a-c).

4.2 Evaluation of trends

Our synthetic MOBO-DIC generally reconstructs both the spatial distribution and magnitude of the trend of sDIC in HAMOCC well, with no indication of a systemic over- or underestimation of the trend (see Supporting Information Fig. S7). An exception is the deep eastern equatorial Pacific, where MOBO-DIC overestimates the trend. This could be the result of overfitting or of challenges of MOBO-DIC to fit the trends in a region with very large lateral gradients and where data coverage is intermittent. We do not see similarly large trends in the reconstructions with observations, possibly because the observed lateral gradients are smaller than those in the model. Still, this mismatch in the synthetic data suggests that the MOBO-DIC reconstructed trends are likely somewhat less robust than the climatologies and that care must be taken to avoid an overinterpretation of the results.

The sDIC trends at the time-series stations are comparable to MOBO-DIC at the times and locations of these independent observations (see Table 2 and Supporting Information Fig. S9). For example, we observe a mean trend in the water column at BATS of 7 μmol kg^{-1} decade^{-1}, while the mean trend in the water column in MOBO-DIC at the grid cell closest to BATS is 5 $\pm$2 μmol kg^{-1} decade^{-1}. However, some quantitative differences exist, with the largest difference in the trend found at depths between 600 and 800 m at BATS. There, MOBO-DIC, with an estimated trend of only 5$\pm$2 μmol kg^{-1} decade^{-1} underestimates the observed trend of 16 μmol kg^{-1} decade^{-1} quite substantially. With BATS being one of the best-constrained time-series sites, the observed trend is very robust. The trend is much better reconstructed in the shallower waters at BATS, indicating that this is not a general issue but an issue specifically associated with the intermediate water masses in the North Atlantic.

MOBO-DIC also underestimates the trend seen in the biogeochemical Argo floats in the Southern Ocean (SOCCOM floats) between 20 and 40 m (see Table 2 and Supporting Information Fig. S10). The observed trend is -20 μmol kg^{-1} decade^{-1}, while the trend estimate in MOBO-DIC at the same grid cells is only -9$\pm$2 μmol kg^{-1} decade^{-1}. There is a known difference between ship-based DIC measurements and DIC derived from float pH measurements (Gray et al., 2018). However, this offset is thought to be relatively steady and should not affect the trend. Nevertheless, the time series is short and spatially sparse, so it is not entirely clear whether the issue is with MOBO-DIC or with the SOCCOM-derived DIC trend.

The trend of MOBO-DIC at the surface has a similar spatial distribution but is slightly smaller than the trend of the mapped surface DIC from Gregor and Gruber (2021), with a global mean trend between January 2004 and December 2018 of 0.6$\pm$0.1 μmol kg^{-1} yr^{-1} and 0.8 μmol kg^{-1} yr^{-1}, respectively (see Supporting Information Fig. S11 d-f). As OceanSODA-ETHZ is based on considerably more surface measurements than MOBO-DIC, it is likely that MOBO-DIC slightly underestimates the trend of the surface DIC.

4.3 Evaluation of Interannual variability

Similar to the trend, our synthetic MOBO-DIC reconstructs the spatial distribution and magnitude of the interannual variability, defined here as the standard deviation across the ensemble, of sDIC in HAMOCC well (see Supporting Information Fig. S8). However, we also find an artifact in the deep eastern equatorial Pacific, i.e., the same region where we had difficulties with the trend. There, the interannual variability is too large in the synthetic MOBO-DIC reconstruction. Again, no such artifact exists in the MOBO-DIC reconstructions with observations, but smaller artifacts cannot be ruled out.

MOBO-DIC tends to underestimate the observed interannual variability of sDIC at the time-series stations and the locations of the SOCCOM floats (see Table 2 and Supporting Information Figs. S9 and S10). The biggest difference in the interannual variability is between 20 and 40 m at HOT, where MOBO-DIC estimates a variability of only 4 μmol kg^{-1}, while the observations suggest a value of 11 μmol kg^{-1}, As above, such differences can be at least partially explained by the observations containing a lot of noise and not necessarily being representative of the mean monthly 1° fields. At Drake Passage, the comparison data displays considerably more variability than our gridded product and may include outliers. Thus, there are instances where the discrepancies between MOBO-DIC and the comparison data sets are beyond the uncertainty limits. We expect that this is mostly due to large local variabilities that are smoothed out in the monthly mean 1°x1° fields in MOBO-DIC.

The interannual variability of MOBO-DIC at the surface also has a similar distribution and is slightly smaller than the interannual variability of the mapped surface DIC from Gregor and Gruber (2021) (see Table 2 and Supporting Information Fig. S11 g-i). Here, we observe global mean standard deviations of 3 and 4 μmol kg^{-1}, respectively (see Supporting Information Fig. S11 g-i). An explanation for their slightly higher variability could lie in the fact that OeanSODA-ETHZ uses satellite-based sea surface temperature (SST) as a predictor while we use float data for temperature and salinity. Satellite-based SST estimates are known to display more variability than float-based estimates (Roemmich & Gilson, 2009). Further, OceanSODA-ETHZ has less interannual variability in pCO_2 than other surface

Table 2. Comparison of the trends (in μmol kg^{-1} decade^{-1}) and interannual variability (IAV, in μmol kg^{-1}), defined as the standard deviation in time (seasonal cycle and trend removed), from independent DIC estimates, and from MOBO-DIC at the time and locations of the independent data. Due to data sparsity in the observational data, we average the fields over depth slabs (20 to 40 m, 100 to 150 m, 600 to 800 m). The locations of the Stations are illustrated in Supporting Information Fig. S1.

	Compared data set → / Depth ↓	BATS	MOBO-DIC at BATS	HOT	MOBO-DIC at HOT	Drake Passage (surface)	MOBO-DIC at Drake Passage	SOCCOM floats	MOBO-DIC at SOCCOM floats
Trend	20 – 40 m	1	7	5	2	8	1	-20	-9
	100 – 150 m	3	8	13	6	N/A	N/A	3	1
	600 -800 m	16	5	4	5	N/A	N/A	19	26
IAV	20 – 40 m	5	2	11	4	9	5	4	3
	100 – 150 m	4	2	6	2	N/A	N/A	2	2
	600 -800 m	4	1	3	1	N/A	N/A	3	3

products such as SOM-FFN by Landschützer et al. (2016). Thus, the available evidence suggests that MOBO-DIC tends to underestimate the interannual variability.

5 Results and Discussion

5.1 Global changes in the DIC inventory

The reconstructed (near) global sDIC inventory between 0 and 1500 m increased steadily from 2004 through 2019, with a total increase of 42±5 Pg C over this period (Fig. 1). All depth ranges contribute to this trend, with ∼16% of the increase in sDIC having occurred in the upper 150 m, 18% between 150 and 300 m, 38% between 300 and 700 m, and 28% between 700 and 1500 m. Superimposed onto this strong positive trend, we observe the effect of the seasonal cycle on the total inventory (order of ∼2 Pg C), some interannual variations, and a weakening of the trend in the second half of the record, most strongly visible in the deepest depth slice analyzed, i.e., below 700 m.

By adding an estimate of the sDIC changes in the shallow coastal regions and the high latitudes (3±0.4 Pg C) and in the ocean below 1500 m (6±6 Pg C; see Supporting Information S3), we arrive at a global sDIC inventory change of 51±11 Pg C. Over the 16 years of our analysis, this corresponds to a rate of increase of 3.2±0.7 Pg C yr^{-1}. We interpret this increase in sDIC to be mostly of atmospheric origin, i.e., reflecting a net uptake of CO_2 from the atmosphere, although we cannot exclude a small contribution coming from other sources, such as a trend in the input from rivers and sediment sources, or an imbalance with the marine organic carbon pool.

Our interior ocean data-based net ocean uptake estimate of 3.2±0.7 Pg C yr^{-1} is comparable with surface pCO_2 observation-based estimates of the net carbon flux from the atmosphere into the ocean. The latest update of the net air-sea CO_2 flux estimate by Landschützer et al. (2016), which includes both the open and coastal ocean, suggests a global uptake of 2.1±0.5 Pg C yr^{-1} from 2004 through 2019. Adding a riverine outgassing of CO_2 of 0.6±0.4 Pg C yr^{-1} (Friedlingstein et al., 2022; Regnier et al., 2022), these surface ocean data suggest a net uptake of 2.7±0.6 Pg C yr^{-1}. This is 0.5 Pg C yr^{-1} less than our estimate based on the increase in ocean interior sDIC but within the uncertainty bounds. Our estimate would be closer to the surface-based estimates if we used the higher-end

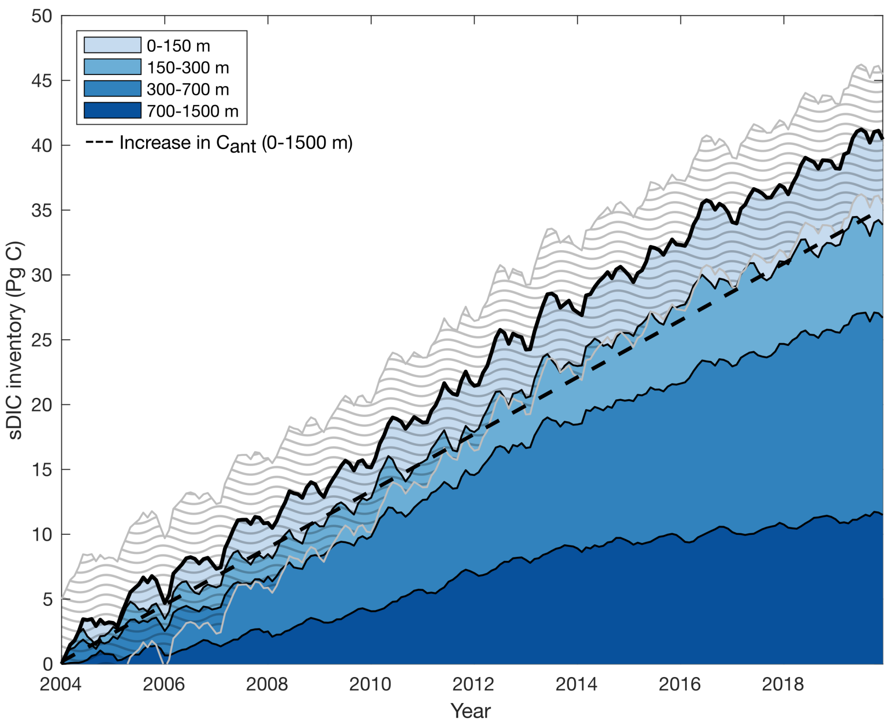

Figure 1. a) Temporal change in the global sDIC inventory derived from MOBO-DIC from 2004 through 2019, relative to January 2004, for different depth slabs: 0 to 150 m, 150 to 300 m, 300 m to 700 m, 700 m to 1500 m (from light blue to dark blue). The gray shading marks the uncertainty around the upper 1500 m. The dashed black line illustrates the estimated increase in C_{ant} based on ΔC_{ant} from 1800 to 2007 scaled to the same period, using a scaling factor α of 0.29.

riverine carbon flux estimate of 0.8±0.4 Pg C yr^{-1} by Resplandy et al. (2018). An even better agreement would be achieved if the recently proposed temperature corrections were applied to the surface-based estimates (Dong et al., 2022; Watson et al., 2020). Specifically, Dong et al. (2022) suggested that the proper accounting of all temperature-related issues (e.g., skin correction) would increase the ocean uptake of the commonly used surface pCO_2 based products by +35% (0.6 Pg C yr^{-1}) for the period 1982 to 2020.

Our estimate of the total increase in ocean sDIC of 51±11 Pg C implies that from 2004 through 2019, the ocean sink accounted for ∼31±7% of the total anthropogenic CO_2 emissions (here: from fossil fuel emissions and land-use change, Friedlingstein et al. (2022)). This uptake fraction is larger but within the uncertainties compared to the fraction reported by the Global Carbon Project based on ocean models and surface ocean pCO_2 products during the decade 2011 to 2020 (26±4%, Friedlingstein et al. (2022)). As pointed out by Friedlingstein et al. (2022), within the Global Carbon Budget estimates, it is particularly the hindcast model-based estimates that indicate a smaller uptake. Similarly, Terhaar et al. (2022) used an emergent constraint approach to demonstrate that most CMIP models tend to take up too little CO_2 from the atmosphere. Although CMIP models differ from the hind-cast models used in the Global Carbon Budget, these findings further indicate that the models underestimate the oceanic carbon uptake, as also discussed by Hauck et al. (2020). Our interior ocean-based estimate thus supports the higher-end (mostly observation-based) estimates of the ocean carbon sink in the Global Carbon Budget, albeit within large uncertainties.

Another reference point is the oceanic accumulation of C_{ant} between 2004 and 2020. Lacking an estimate of the C_{ant} accumulation over the same period, we scale the estimates of Sabine et al. (2004) and Gruber et al. (2019) to this period, assuming a transient steady-state (see Section 2.4). We obtain a global increase of 44±6 Pg C (2.8±0.4 Pg C yr^{-1}) in C_{ant} (1800-2007 scaled to 2004-2019 with a scaling factor of 0.29) and 49±6 Pg C (3.1±0.4 Pg C yr^{-1}) in C_{ant} (1994-2007, scaled to 2004-2019 with a scaling factor of 1.45). The estimates are remarkably close to our estimate of the increase in total sDIC (51±11 Pg C, i.e., 3.2±0.7 Pg C yr^{-1}). This suggests that we can largely attribute the reconstructed increase in the sDIC to the uptake of anthropogenic CO_2 from the atmosphere. Similarly, when only considering the domain of MOBO-DIC and without upscaling, we also find that the trend in MOBO-DIC (40±5 Pg C, i.e., 2.5±0.3 Pg C yr^{-1}) is close to the increase in C_{ant} over the same period and domain (35±4 Pg C, i.e., 2.2±0.2 Pg C yr^{-1}, dashed line in Fig. 1), and also well within the uncertainties. Considering the proposed outgassing signal of C_{nat}, this would have been reflected in a weaker trend in total sDIC than in C_{ant}; however, we do not observe this during our study period.

Superimposed onto this positive long-term trend of sDIC, the reconstructions reveal substantial interannual variations and a weakening of the trend after ∼2012, especially in the deeper waters. The following sections will further discuss these variations and the weakening trend. We also dive deeper into the differences between the anthropogenic component and the total sDIC in the water column, revealing changes in the natural DIC pool. Additionally, we find a strong seasonal signal, most pronounced near the surface. We do not discuss the seasonal variations near the surface, as the seasonal cycle of DIC was explored in Keppler et al. (2020b).

5.2 Regional distribution of trends in sDIC

The rate of the depth-integrated accumulation of sDIC is regionally strongly structured (Fig. 2a), with the highest rates of accumulation found in the North Atlantic south of Iceland, i.e., the Subpolar Gyre. There, the linear trend exceeds 1.5 mol m^{-2} yr^{-1}. An additional region with elevated rates of increase can be identified in the southern hemisphere between about 20°S and 45°S with typical accumulation rates of ∼1 mol m^{-2} yr^{-1}. The higher latitudes of the Southern Ocean, the tropical regions, the northern Indian, and particularly the North Pacific have considerably weaker depth-integrated changes in sDIC, typically 0.5 mol m^{-2} yr^{-1} or less. In some regions of the North Pacific, the depth-integrated sDIC even decreases over our study period. This vertical integral turns out to be a robust feature of our analyses as it is only weakly changing when removing trends within the water column that are not significant (compare Supporting Information Fig. S12 with Fig. 2a).

At each depth level, most of the trends in sDIC are statistically significant (95% confidence interval, see Supporting Information S7). In addition, the vertical integral does not change considerably when removing trends that are not significant (compare Supporting Information Fig. S12 with Fig. 2a). This is also the case for the negative trends in the North Pacific. Further support comes from the existence of a comparable negative trend in the surface DIC reconstructions of the OceanSODA-ETHZ product (Gregor & Gruber, 2021), as demonstrated in Section 4.2 and Supporting Information Fig. S11. Thus, this negative signal in the North Pacific appears robust within our period and is not an artifact of our method.

The similarity between the rate of depth-integrated accumulation of sDIC and C_{ant} becomes even more evident when they are put side by side, irrespective of how we estimated the expected change in C_{ant} from 2004 through 2019. The patterns and magnitude of the depth-integrated accumulation of sDIC (Fig. 2a) and the two different estimates of C_{ant}

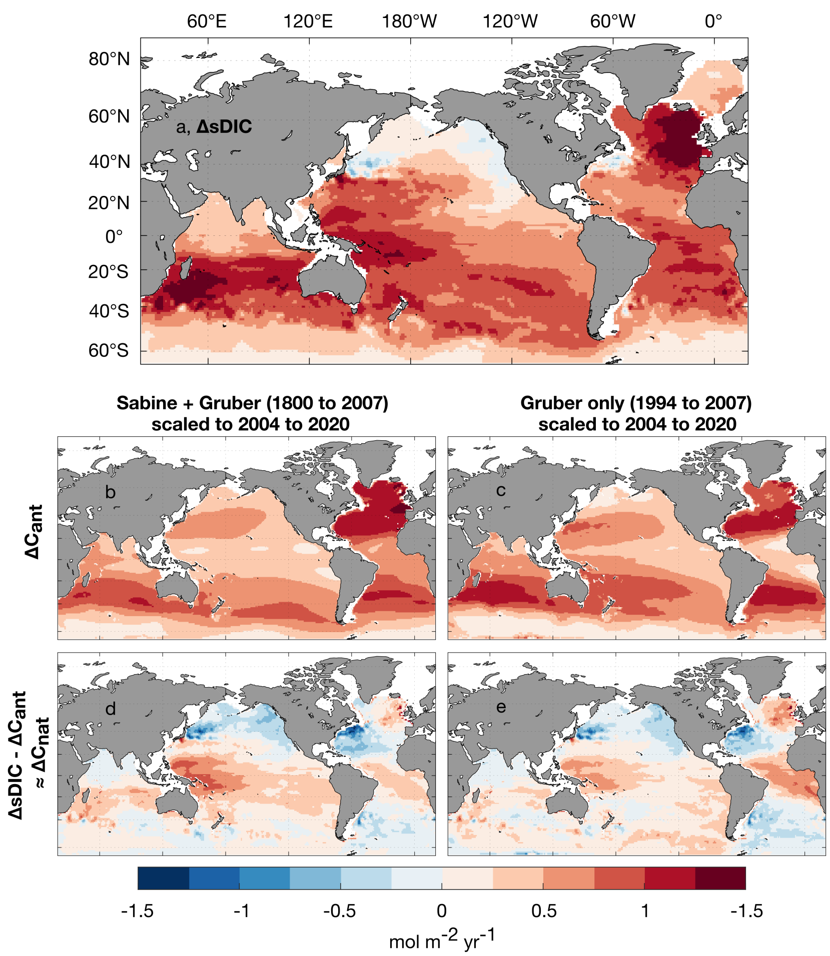

Figure 2. Maps of the column-integrated (upper 1500 m) (a) change in sDIC from 2004 through 2019 based on the linear trend, (b,c) change in C_{ant} scaled to the same period (2004 through 2019), and(d,e) the anomalous change (i.e., approximately the change in C_{nat}) from 2004 through 2019, estimated from the difference between the change in the MOBO-DIC inventory [illustrated in (a)], and the change in the C_{ant} inventory, scaled to the same period as (a) [illustratedin (b and c)]. For the combined estimate of C_{ant} by Sabine et al. (2004) (1800 to 1994) and Gruber et al. (2009) (1994 to 2007) (b,d) and for the estimate of C_{ant} by Gruber et al. (2009) (1994 to 2007; c,e). Scaling on the basis of the transient steady-state model (anom = ΔMOBO-DIC $-$ $\alpha \cdot \Delta C_{ant}$, $\alpha = 0.29$ for the period 1800-2007 and $\alpha = 1.45$ for the period 1994-2007). See Supporting Information Fig. S12 for the trends in MOBO-DIC on individual depth levels.

(Fig. 2b,c) are to the first order approximately the same, as also evidenced by their high pattern correlation coefficient c = 0.56 and 0.63, between the trend in MOBO-DIC and the scaled ΔC_{ant} from the combined estimate by Sabine et al. (2004) and Gruber et al. (2019), and the estimate by Gruber et al. (2019), respectively. For example, we observe in all fields a large increase in the North Atlantic and a broad band of enhanced accumulation in the mid-latitudes of the Southern hemisphere. Also present in all fields is the weaker signal in the mid-latitude Southern Ocean. This further supports the conclusion that most of the column-integrated change in sDIC can be attributed to the increase in C_{ant} during this period.

However, there are also several notable differences, discernible when we subtract the estimated anthropogenic component (i.e., ΔC_{ant}) from the reconstructed change in sDIC (Fig. 2d,e). This difference can be interpreted as the change in the natural oceanic CO_2 component of DIC, i.e., ΔC_{nat}, although given our steady-state assumption when estimating ΔC_{ant}, this difference can also contain an element of the non-steady-state, i.e., climate variability induced, component of ΔC_{ant}. The North Pacific stands out as the region with the biggest loss in C_{nat}. In addition, C_{nat} is lost in the upwelling region of the Atlantic sector of the Southern Ocean and the Subtropical Gyre of the North Atlantic. These losses of C_{nat} are counter-balanced by gains of C_{nat} in the tropics and the Indo-Pacific sector of the Southern Ocean. Furthermore, in the North Atlantic Subpolar Gyre, a region of strong uptake of C_{ant}, we also observe an increase in C_{nat}. Integrating ΔC_{nat} yields a total increase of 0.4±0.8 Pg C yr^{-1}, and 0.1±0.8 Pg C yr^{-1}, for C_{nat} based on the combined estimate (Sabine et al., 2004; Gruber et al., 2019), and the estimate by Gruber et al. (2019), respectively. Given the lack of statistical significance, we conclude that we cannot detect a global change in C_{nat} during our study period.

Nonetheless, the reduction of ΔC_{nat} in the North Pacific stands out. We link this change to the phasing of the Pacific Decadal Oscillation (PDO) as it shifted between 2004 and 2019 from positive to negative. While negative PDO regimes are associated with a shallow thermocline in the Kuroshio Extension, which results in deep mixing and cooler SSTs in the North Pacific, positive PDO regimes are associated with warmer SSTs (Mantua & Hare, 2002). Thus, we speculate that during our analysis period, the shoaling of the thermocline in the North Pacific brought DIC stored at depth to the surface, allowing it to outgas, leading to an overall loss of DIC in this region. We expect that the opposite would occur during positive phases of the PDO, so that the net change over multiple decades would be close to zero, and thus not impact the long-term trend. To test this hypothesis, we plotted the trend in the surface sDIC from OceanSODA-ETHZ (Gregor & Gruber, 2021) over their entire study period (1985 through 2018). Over that extended period, we do not observe negative trends in surface sDIC in the North Pacific (not shown), indicating that the observed negative trend in the North Pacific sDIC and C_{nat} between 2004 and 2019 is not a long-term signal. The loss of C_{nat} in the North Pacific during our analysis period is partially balanced by a gain in C_{nat} in most parts of the Indo-Pacific, especially in the Western tropical Pacific. We find that this signal is associated with the phasing of the El Niño Southern Oscillation (ENSO), as further discussed in Supporting Information Fig. S13. We speculate that over a longer period than our 16 years, this signal of increased C_{nat} in the Western tropical Pacific would also be dampened.

Similarly, we link the changes in C_{nat} in the North Atlantic to the phasing of the Atlantic Multidecadal Oscillation (AMO; Kerr (2000) as between 2004 and 2019, the AMO index moved from positive to negative (see `https://climatedataguide.ucar.edu/climate-data/atlantic-multi-decadal-oscillation-amo`). Negative AMO phases are associated with increased vertical mixing in the North Atlantic Subpolar Gyre, and thus, an increase of upper ocean DIC and C_{nat} in this region (Breeden & McKinley, 2016). Concurrently, in the North Atlantic Subtropical Gyre, negative AMO phases are associated with a decrease in DIC and C_{nat} in this region due to changes in the temperature affecting the solubility of CO_2. In the tropical Atlantic, the increase in C_{nat} during our study period might be associated with teleconnections from the AMO phasing. The loss of C_{nat} in the South Atlantic is in line with the findings by Keppler and Landschützer (2019) who reported a weakening of the Southern Ocean carbon sink in the Atlantic sector since ~2012. They linked this weakening to shifts in sea level pressure and associated changes in surface winds. We note that these links between changes in C_{nat} and the PDO and the AMO are speculative at this point, as the relatively short temporal extent of MOBO-DIC (16 years) prevents us from robustly concluding on the effect of multi-decadal modes of variability.

Fig. 3 reveals how the trend in sDIC varies with depth at the scale of entire ocean basins split into latitude bands (black line). Near the surface, sDIC is reconstructed to have increased, on average by about 0.6 μmol kg^{-1} yr^{-1}, with some regions having a higher accumulation (e.g., 0.8 μmol kg^{-1} yr^{-1} in the North Atlantic) and other regions less (e.g., 0.3 μmol kg^{-1} yr^{-1} in the North Pacific). In all regions, the trend in sDIC increases between the mixed layer and the intermediate waters and then decreases with depth below that, reaching values of around 0.2 μmol kg^{-1} yr^{-1} at 1500 m. We observe the largest increase in sDIC in the Atlantic between ∼200 m and 500 m (∼0.9 μmol kg^{-1} yr^{-1}).

Comparing the temporal trends in sDIC with the estimated changes in C_{ant} (blue and red lines in Fig. 3) highlights strong similarities but also distinct differences. Near the surface, sDIC increased less than C_{ant} during our study period. This difference is significant in all regions except for the Southern Ocean and North Atlantic. In the deeper ocean, the difference between the trend in sDIC and ΔC_{ant} is not significant in the Southern Ocean, North Pacific, tropical Indian Ocean, and the South Atlantic, while in the other regions, the trend in sDIC tends to be larger than the two estimates of ΔC_{ant}. The differences between the trends in sDIC compared to those in C_{ant} imply a loss of $C_n at$ in the upper ocean, and a gain of $C_n at$ in the ocean's interior below a few hundred meters depth. Combined with the lack of an overall change in C_{ant}, this suggests a strong internal redistribution of oceanic $C_n at$ over our analysis period.

The similarities and differences in the vertical distribution of the trends in sDIC, C_{ant}, and C_{nat} become even more evident when analyzing zonal mean sections of these components (Fig. 4). Due to methodological constraints, there are some discontinuities at 500 m in the MOBO-DIC derived sDIC (Fig. 4a-c), which are associated with boundaries generated by the depth slabs. Aside from that, the trend in sDIC and ΔC_{ant} (Fig. 4d-f) are very similar, as noted above for the mean profiles. This figure again highlights the loss of C_{nat} (Fig. 4g-i) at the surface, except in the North Atlantic. We also observe a loss of C_{nat} in the North Pacific, extending down to 1500 m but most pronounced in the upper ∼800 m. The northern high latitudes tend to lose C_{nat} at depth, while the low latitudes tend to gain C_{nat} at depth. Overall, the redistribution of C_{nat} occurs both horizontally, as demonstrated in Fig. 2, and vertically (Fig. 3 and 4), but as pointed out above, the signal in C_{nat} is within the uncertainty bounds.

We cannot identify the potential reasons for this redistribution, but the upper ocean loss of C_{nat} may be at least partially driven by the warming of the ocean, which is strongest in the upper ocean (IPCC, 2021). In addition, such a redistribution pattern is reminiscent of the impact of the ocean's biological pump, where an increased efficiency of this pump would lead to a depletion of $C_n at$ in the upper ocean and an accumulation at depth. As we observe this pattern most prominently in the tropics, we speculate that biology may be driving the change in sDIC here. Conversely, as we already hypothesized above, the other regions, including the North Pacific, North Atlantic, and Southern Ocean are likely driven by physical changes.

It should also be noted that the vertical profile in the trend is strongly influenced by interannual variations, such as variations in the thermocline and surface outgassing. Thus, the signal in the mixed layer is prone to large interannual to decadal variations, which are especially dominant in the Southern Ocean (Le Quéré et al., 2007; Landschützer et al., 2015; Keppler & Landschützer, 2019). Therefore, the observed trends in the mixed layer depend greatly on the start and end year and should be interpreted with care. A longer time series would yield a more robust result.

5.3 Interannual variability at global and basin-scale

The interannual variability of sDIC, defined here as the standard deviation in time (seasonal cycle and trend removed), is in our product rather small, especially when compared to the magnitude of the trend (previous section) and the amplitude of the seasonal cycle

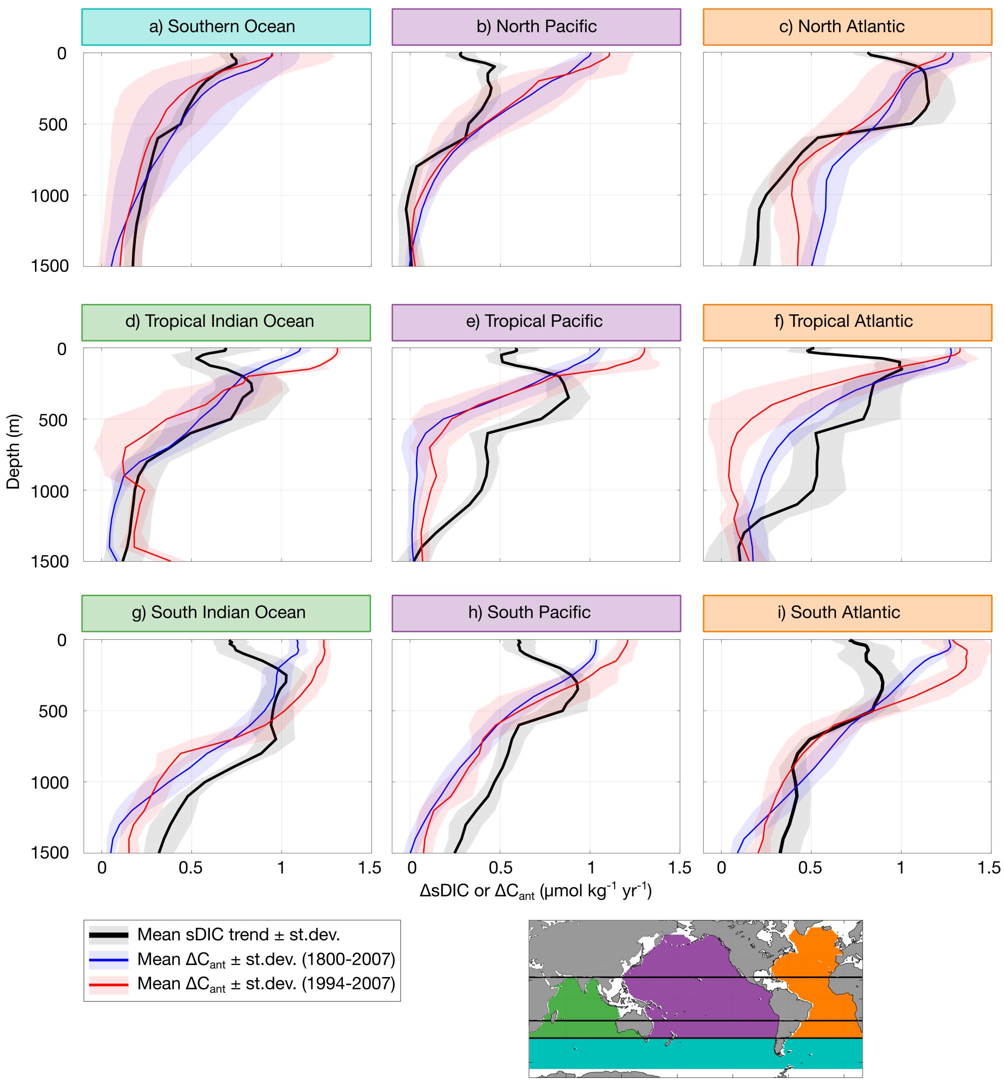

Figure 3. Vertical profiles of the mean trend in subregions for sDIC estimated by MOBO-DIC (black) and ΔC_{ant} from 1800 to 2007 scaled to the period 2004 through 2019 (blue), and from 1994 to 2007, scaled to 2004 through 2019 (red). The uncertainty of the trend in sDIC, based on the standard deviation across the trend in the 15 ensemble members, is illustrated in shading. The uncertainty of the trend in ΔC_{ant}, based on the standard deviation in the latitude-longitude space, is illustrated in shading. Separately for the Southern Ocean (a), Indian Ocean (d,g), Pacific (b,e,h), Atlantic (c,f,i), in the northern temperate regions (until 23°N, b,c), the tropics (23°N to 23°S, d-f), and in the southern temperate regions (from 23°S to 40°S, g-i). The map at the bottom indicates the limits of the ocean basins in color, and the climatic regions are delimited by black lines.

(Keppler et al., 2020b). With a global mean temporal standard deviation of 2 μmol kg^{-1} at 150 m (the depth level with the largest mean standard deviation), compared to a global mean uncertainty of 18 μmol kg^{-1} at 150 m, the interannual variability is well within the product uncertainty of MOBO-DIC in most parts of the ocean. However, as highlighted in Section 4.3, MOBO-DIC likely underestimates the interannual variability.

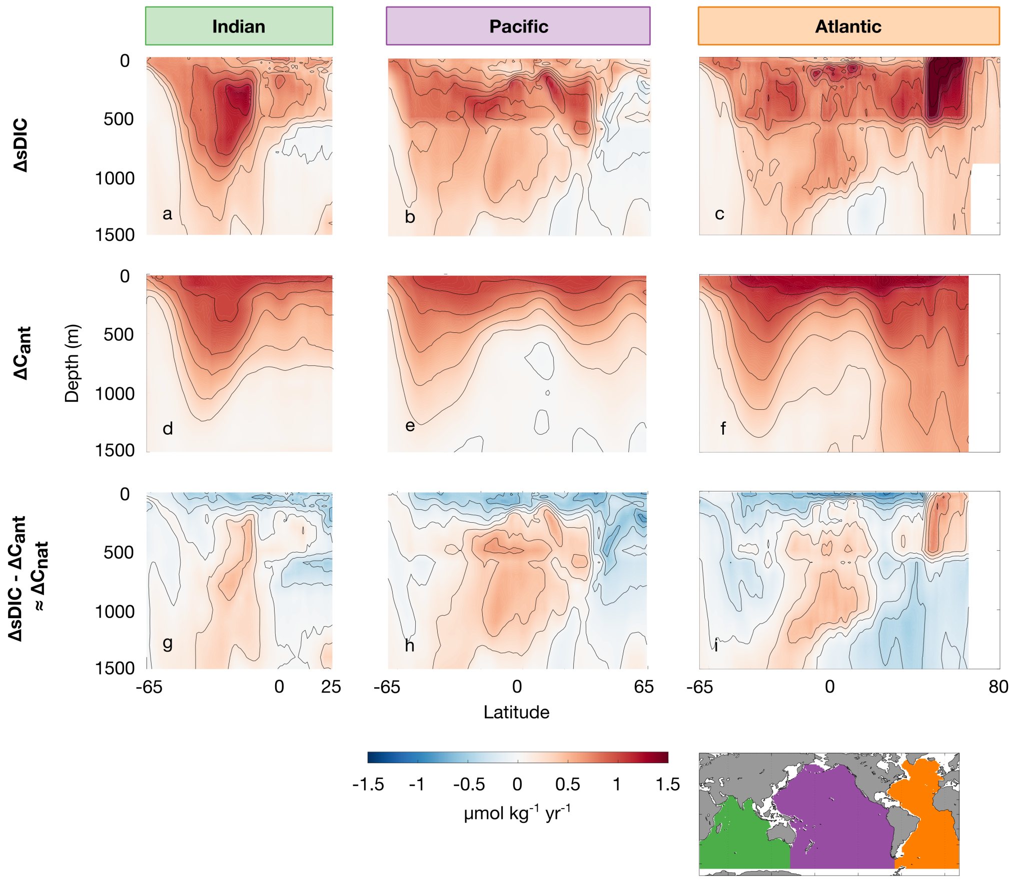

Figure 4. Zonal mean sections of the trend in sDIC from 2004 through 2019 (a-c), of ΔC_{ant} from 1800 to 2007, scaled to our period (d-f), and the difference between the two, i.e., ΔC_{nat} (g-i), for the Indian Ocean (a,d,g), Pacific (b,e,h), and the Atlantic (c,f,i). The map at the bottom right illustrates the boundaries of the basins.

Nevertheless, some clear regional signals of the interannual variability emerge (Fig. 5): the largest interannual signal is generally in the thermocline region (∼150 m), while in the mixed layer and below 700 m, the interannual variability is minimal. The equatorial Pacific stands out as a region with the largest variance, while we observe very little interannual variability in the Southern Ocean, a region with large decadal variability in the air-sea CO_2 flux estimates (Le Quéré et al., 2007; Landschützer et al., 2015; Keppler & Landschützer, 2019). A recent study has suggested that the decadal variations of the air-sea CO_2 fluxes in the Southern Ocean may be overestimated in the mapped surface estimates (Gloege et al., 2021); however, the strongest variations occur around the year 2000 (see, e.g., Friedlingstein et al. (2022)), i.e., before the start of our time-series here.

We further illustrate the nature of the mean vacillations of the vertically integrated sDIC (upper 1500 m) for large subregions in Fig. 6. The most dominant interannual variations are found in the Pacific, where we see a steep increase in sDIC between 2010 and 2014 in the tropics. The northern temperate Pacific also stands out: Here, the trend in sDIC is initially weak until 2010, increases until 2014, and then we observe a negative trend until the end of the time series in December 2019. Both in the northern and southern temperate regions of the Atlantic, the sDIC trend has weakened since around 2012. In contrast, averaged over the

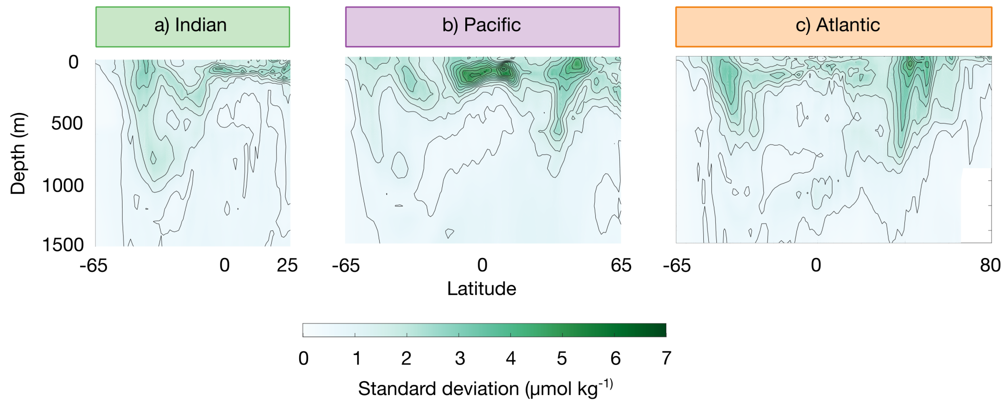

Figure 5. Zonal mean sections of the interannual variability of sDIC, defined as the standard deviation of the time-dimension of sDIC (detrended, seasonal cycle smoothed with a 12-month running mean) for the Indian (a), Pacific (b), and Atlantic Oceans (c). See the map at the bottom right of Fig. 4 for the boundaries of the basins.

whole Southern Ocean, we find very few interannual variations here. Similarly, the Indian Ocean, the South Pacific, and the tropical Atlantic all vary little interannually in the upper 1500 m when averaging over these areas.

We link the sDIC increase in the tropical Pacific at least partially to a shift from La Niñas (especially in 2008 and 2011) to El Niños (especially in 2015 and 2019, see Supporting Information Fig. S13). The other ENSO-related signals during our study period are considerably weaker and seem mostly dampened when considering the whole tropical Pacific. The large variation in the North Pacific is likely to be influenced by the phasing of the PDO, but may also have an ENSO-related teleconnection. We find that the weakening of the vertically integrated sDIC around 2012, illustrated in Fig. 1, stems largely from the high latitude South Atlantic and the tropical Pacific. The weakening of the sink in the high latitude South Atlantic is in line with the findings by Keppler and Landschützer (2019), who report a weakening of the CO_2 uptake in the Atlantic sector of the Southern Ocean around 2012. While this signal is not dominant when averaging over the whole Southern Ocean, this weakening sink around 2012 is also visible in the global changes in sDIC (Fig. 1), highlighting the important role of the Southern Ocean carbon uptake (here: specifically its Atlantic sector) globally. A longer time series is needed to investigate if this is a long-term decline or part of multi-decadal oscillations, such as the AMO. We know from previous studies that this weakening may be due to changes in the circulation, as suggested by DeVries et al. (2017) or linked to atmospheric circulation, as proposed by Keppler and Landschützer (2019). An alternative hypothesis for these changes is that volcanoes are the driving force for such sudden changes (McKinley et al., 2020). However, during our study period, no large volcanic eruptions occurred that may explain the observed signals.

6 Caveats and Uncertainties

Given the sparsity of DIC observations, our product fills substantial observational gaps in time and space. However, our evaluation with independent data provides confidence in the robustness of the presented numbers within the uncertainty limits. Nonetheless, there are good reasons to conclude that MOBO-DIC tends to underestimate the trend and interannual variability. Although this underestimation is within the uncertainty limits, it

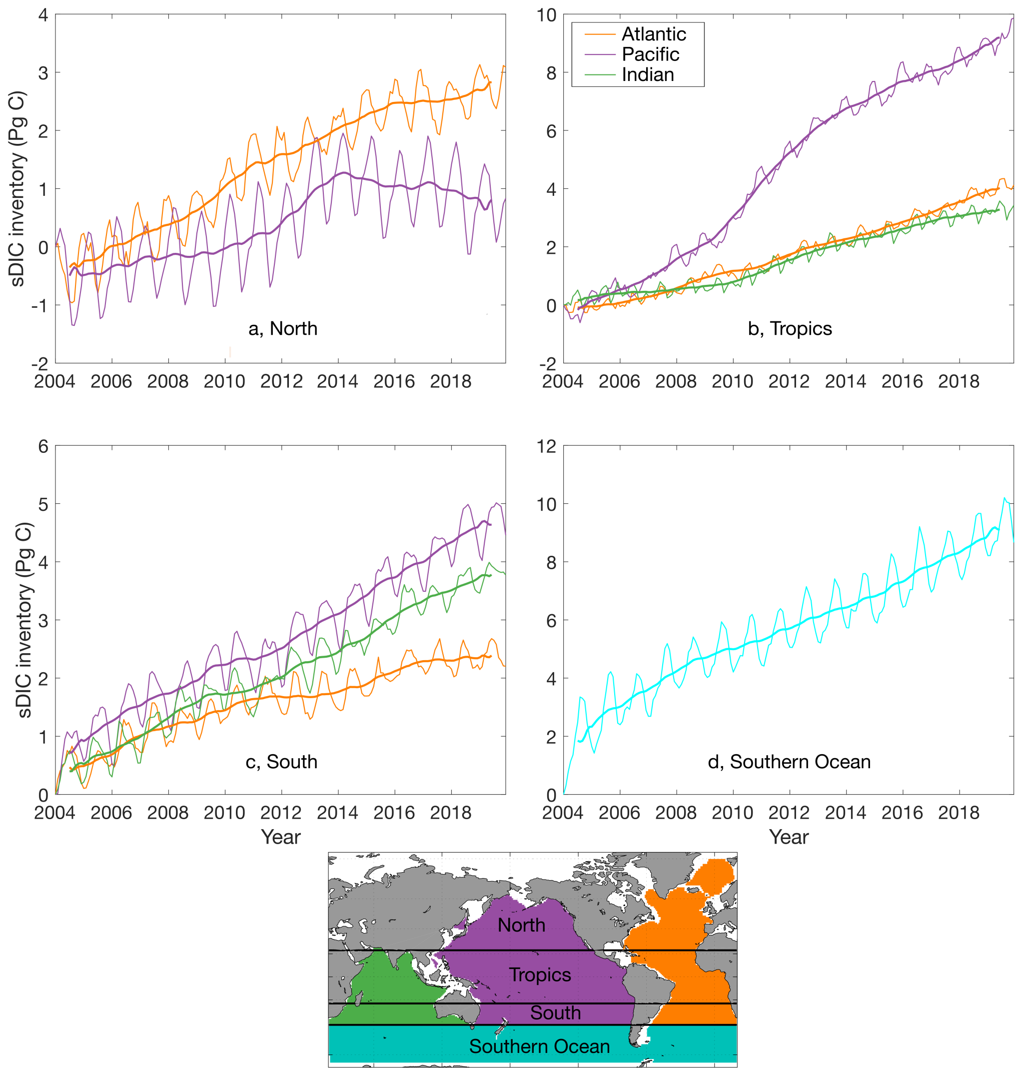

Figure 6. Timeline of the vertical integral (upper 1500 m) of sDIC relative to January 2004 (think solid lines) in the northern temperate regions (a), tropics (b), southern temperate regions (c), and the Southern Ocean. In a-c, separately for the Atlantic (orange), Pacific (purple), and Indian Ocean (green). Note that the y-axes differ in each subplot. Thick solid lines have the seasonal cycle smoothed with a 12-month moving average (first and last six months removed). The inserted map illustrates the boundaries of the subregions.

could be significant when integrating in the water column (see Section 4 and Supporting Information S5 and S6). Further research should be conducted on this, especially as more data becomes available with new GLODAP releases and BGC Argo data.

The uncertainties of the MOBO-DIC estimated sDIC at the level of a single grid cell are relatively large (global mean of 18 μmol kg^{-1}) and are often larger than the signal in the trend or variability. As our mapping method minimizes the overall bias between the target data (i.e., the GLODAP DIC measurements) and the mapped estimate, we can assume that any local imprecisions average out when integrating or averaging over large areas. This means that MOBO-DIC is most robust when considering large areas, while analyses at single grid cells should be interpreted carefully. In this study, we present such integrals and averages over whole ocean basins.

We want to note that the linear trend analysis used to quantify and assess the long-term changes in DIC has its limitations, too. First, it is not a given that the increase in oceanic carbon is, in fact, linear. Second, the linear trends are based on a relatively short period of 16 years, and thus, the conditions of the start and end years tend to considerably affect the trend over such a short period (Fay & McKinley, 2013). Furthermore, decadal variations might also affect the linear trends. We found that, locally, some trends are not robust (see Supporting Information Fig. S12) but anticipate that our global trend estimate is robust within the uncertainty, as overestimates of the trend in some regions are likely to be balanced by underestimates elsewhere.

Our comparison with C_{ant} also relies on many assumptions. First, as there is not yet a published estimate of C_{ant} for the current period, we scaled previous estimates to our period, assuming a steady state (see Section 2.4). Further, our estimate of C_{nat} is based on the difference in the change in total sDIC and ΔC_{ant}. However, due to the steady-state assumption when estimating ΔC_{ant}, the difference may also contain an element of the non-steady-state component of anthropogenic ΔC_{ant}. Thus, the analyses with C_{ant} and C_{nat} could be improved in the future by using a C_{ant} estimate of the same period.

7 Summary and Conclusions

This release of the Mapped Observation-Based Oceanic Dissolved Inorganic Carbon (MOBO-DIC) extends the climatological estimate by Keppler et al. (2020b) in time, thus giving insights into the spatiotemporal evolution of the ocean DIC stock at a monthly resolution from January 2004 through December 2019. With a spatial resolution of 1°, extending from 65°N to 65°S, and until 80°N in the Atlantic, and covering the entire upper and middle ocean (depths from 2.5 m to 1500 m on 28 uneven depth levels) this dataset provides a near-global view. We conducted an in-depth validation of our new data product, which considers sources of uncertainties from the measurements, representation errors, and uncertainties stemming from our mapping method. We trust that our estimate of DIC is robust within the uncertainty ranges provided (global mean uncertainty of 18 μmol kg^{-1}).

Our analysis of the trend in sDIC provides the first direct assessment of the changes in the total sDIC stock (natural + anthropogenic) based on observations. It should be noted that at large scales, the changes in sDIC and DIC are numerically equal because the trend in salinity is negligible once integrated vertically and over large regions (Cheng et al., 2020). Our estimate of the global increase of sDIC during our study period (3.2±0.7 Pg C yr^{-1}) is approximately 31±7% of the anthropogenic CO_2 emissions from fossil fuels and land use change during our study period (Friedlingstein et al., 2022). We find that this increase in sDIC is largely associated with the increase in anthropogenic carbon (C_{ant}) during this period (2.8±0.4 Pg C yr^{-1} or 3.1±0.4 Pg C yr^{-1}, depending on the method).

MOBO-DIC also allows for the first assessment of changes in natural oceanic carbon (ΔC_{nat}) by subtracting ΔC_{ant} from the changes in the total sDIC, yielding a statistically insignificant global mean ΔC_{nat} of 0.4±0.8 Pg C yr^{-1} or 0.1±0.8 Pg C yr^{-1}, depending on the method used to estimate C_{ant}. Previous studies had suggested a potential outgassing of C_{nat} due to elevated sea surface temperatures (McNeil & Matear, 2013), which would affect the global climate. While the large uncertainties in MOBO-DIC and C_{ant} do not rule out such a net outgassing signal of C_{nat}, we observe no statistically detectable change in C_{nat} between 2004 and 2020. Instead, our analysis reveals a redistribution of C_{nat} - a phenomenon that had not been previously investigated at a global scale. During our study period, the upper ocean appears to have mostly lost C_{nat}, while below that, large parts of the ocean increased in C_{nat}. The loss of C_{nat} near the surface could be driven by increased ocean temperatures, as proposed by IPCC (2021). The redistributions in the

Pacific correspond to the phasing of the El Niño Southern Oscillation (ENSO) and the Pacific Decadal Oscillation (PDO), while the redistributions in the North Atlantic correspond to the phasing of the Multidecadal Atlantic Oscillation (AMO). However, at this stage, our study period from 2004 through 2019 is too short to robustly conclude on (multi-) decadal signals.

The interannual variability in sDIC is substantially weaker than the seasonal cycle and temporal trend in most parts of the ocean. However, it should be noted that MOBO-DIC likely underestimates the interannual variability. We find a mean standard deviation in time of detrended, deseasonalized sDIC at the depth level with the largest variability (150 m) is 2 μmol kg^{-1}. We find that most of the global-scale variations in sDIC stem from the North and tropical Pacific, in correspondence with ENSO and the PDO, and to a lesser extent from the high latitude South Atlantic. We find a weakening of the positive trend in the high-latitude South Atlantic around the year 2012. This signal is also visible in the global integral of the sDIC, and future studies should examine the continued evolution of this signal as well as its drivers. The interannual variations are comparably weak in the other sectors of the Southern Ocean and the Indian Ocean.

We can now constrain the ocean carbon sink from surface measurements in combination with riverine flux estimates (previous studies) and based on the direct DIC measurements that reflect the changes in the DIC pool (this study). While the surface-based estimates benefit from more observations, large uncertainties are associated with such an indirect approach. The interior perspective suffers from considerably less data but, due to the direct approach, does not need a riverine flux adjustment or gas transfer parametrization. The two perspectives each have their strengths and weaknesses, so having both perspectives substantially improves our understanding and the quantification of the global ocean carbon sink. The two estimates are in good agreement (3.2±0.7 Pg C yr^{-1} and 2.7±0.6 Pg C yr^{-1} for the interior and surface perspective, respectively), despite being based on independent data (SOCAT vs. GLODAP). However, the surface-based estimates would be larger (i.e., closer to our estimate) when considering a higher-end riverine flux estimate (e.g., 0.8±0.4 Pg C yr^{-1} by Resplandy et al. (2018), compared to 0.6±0.4 Pg C yr^{-1} by Friedlingstein et al. (2022) used in this study). In addition, the agreement between the surface-based estimates and our interior ocean estimate would be even higher if the proposed temperature corrections were applied to the surface estimates. Specifically, Dong et al. (2022) estimated that accounting for these corrections would increase the ocean uptake of the surface pCO_2 based products by 0.6 Pg C yr^{-1} from 1982 through 2020.

Further, within the Global Carbon Budget (Friedlingstein et al., 2022), the observation-based methods that estimate the carbon fluxes based on surface measurements are higher than the model-based estimates. Our analysis from the interior ocean perspective suggests that the true value likely lies closer to the observation-based surface estimates in the Global Carbon Budget than to the model-based estimates, as also suggested by Terhaar et al. (2022). Thus, the current approach of averaging all ocean carbon sink estimates from observations and models in the Global Carbon Budget could be revisited and improved to obtain the best estimate, e.g., by weighting the observation-based estimates stronger than the models.

Our new data product is available for the scientific community and can be used to further investigate the temporal changes in DIC and its effect on marine organisms. Potential further insights into the processes and drivers could be gained by prolonging the timespan and investigating the multi-decadal variations. Additionally, our product provides the basis to compare the decadal variations of observation-based DIC to the changes in the upper Meridional Overturning Circulation, which weakened in the 1980s, strengthened in the 1990s, and weakened again in the 2000s (DeVries et al., 2017). Similarly, further comparing the decadal variations of the Southern Ocean carbon sink (Le Quéré et al., 2007; Landschützer et al., 2015; Keppler & Landschützer, 2019) to the variations in the DIC pool in this region could lead to important new insights on the global carbon cycle.

Acknowledgments

The research leading to these results has received funding from the European Community's Horizon 2020 Project under grant agreement no. 821003 (4C). This work was also sponsored by NSF's Southern Ocean Carbon and Climate Observations and Modeling (SOCCOM) Project under the NSF Awards PLR-1425989 and OPP-1936222, with additional support from NOAA and NASA. The authors are grateful for the Argo data collected and made freely available by the International Argo Program and the national programs that contribute to it (https://www.argo.ucsd.edu and https://argo.jcommops.org). The Argo Program is part of the Global Ocean Observing System. This publication uses Hawaii Ocean Time-series observations supported by the U.S. National Science Foundation under Grant OCE-1260164. It also used data from the Southern Ocean Carbon and Climate Observations and Modeling project (SOCCOM). Data were collected and made freely available by SOCCOM, funded by the National Science Foundation, Division of Polar Programs (NSF PLR-1425989), supplemented by NASA and by the International Argo Program and the NOAA programs that contribute to it. This work benefited from discussions with Birgit Klein (BSH), Jochem Marotzke (MPI-M), Johanna Baehr (UHH), and Jens D. Müller (ETHZ).

Data availability

The data product created during this study are freely available from NCEI/OCADS: **XXX** and should be cited as **XXX TBC**.

The GLODAP DIC ship measurements are available at https://www.ncei.noaa.gov/data/oceans/ncei/ocads/data/0237935/. The mapped Argo-based fields of temperature and salinity are available at http://sio-argo.ucsd.edu/RG_Climatology.html. The WOA-mapped climatologies of silicic acid, nitrate, and dissolved oxygen are available at https://www.nodc.noaa.gov/OC5/woa18/woa18data.html. The atmospheric pCO_2 based on the GlobalView xCO_2 is available at https://www.nodc.noaa.gov/ocads/oceans/SPCO2_1982_present_ETH_SOM_FFN.html. The mapped annual climatology of DIC is available at https://www.ncei.noaa.gov/data/oceans/ncei/ocads/data/0162565/mapped/. The time-series data from HOT, BATS, and Drake Passage are available at http://hahana.soest.hawaii.edu/hot/hot-dogs/bextraction.html, http://bats.bios.edu/bats-data/, and https://www.nodc.noaa.gov/archive/arc0118/0171470/2.2/data/0-data/, respectively. The DIC estimated based on BGC-Argo floats in the Southern Ocean (SOCCOM floats) is available at http://soccompu.princeton.edu/www/index.html. The OceanSODA surface DIC fields are available at https://www.ncei.noaa.gov/access/metadata/landing-page/bin/iso?id=gov.noaa.nodc:0220059. The MOBO-DIC monthly climatology is available at https://www.ncei.noaa.gov/access/metadata/landing-page/bin/iso?id=gov.noaa.nodc\%3A0221526. The monthly climatology of DIC by Broullón et al. (2020) is available at https://doi.org/10.20350/digitalCSIC/10551. The data for C_{ant} are available at https://www.ncei.noaa.gov/access/ocean-carbon-data-system/oceans/ndp_100/ndp100.html and https://www.ncei.noaa.gov/access/metadata/landing-page/bin/iso?id=gov.noaa.nodc:0001644 for the periods 1800 to 1994 and 1994 to 2007, respectively. We use the bathymetry from Etopo2 (2001), and the Multivariate El Niño Index (MEI; Wolter and Timlin (2011); https://psl.noaa.gov/enso/mei/).

References

Bakker, D. C. E., Pfeil, B., Landa, C. S., Metzl, N., O'Brien, K. M., Olsen, A., ... Xu, S. (2016). A multi-decade record of high-quality fCO2 data in version 3 of the Surface Ocean CO2 Atlas (SOCAT). *Earth System Science Data*, *8*(2), 383–413. doi: 10.5194/essd-8-383-2016

Bates, N. R., Astor, Y. M., Church, M. J., Currie, K., Dore, J. E., Gonzalez-Davila, M., ... Magdalena Santana-Casiano, J. (2014). A Time-Series View of Changing Surface Ocean Chemistry Due to Ocean Uptake of Anthropogenic CO2 and Ocean Acidification. *Oceanography*, *27*(1), 126–141. doi: 10.5670/oceanog.2014.16

Bittig, H. C., Maurer, T. L., Plant, J. N., Schmechtig, C., Wong, A. P. S., Claustre, H., ... Xing, X. (2019). A BGC-Argo Guide: Planning, Deployment, Data Handling and Usage. *Frontiers in Marine Science*, *6*. doi: 10.3389/fmars.2019.00502

Bittig, H. C., Steinhoff, T., Claustre, H., Fiedler, B., Williams, N. L., Sauzède, R., ... Gattuso, J.-P. (2018). An Alternative to Static Climatologies: Robust Estimation of Open Ocean CO2 Variables and Nutrient Concentrations From T, S, and O2 Data Using Bayesian Neural Networks. *Frontiers in Marine Science*, *5*. doi: 10.3389/fmars.2018.00328

Boyer, T. P., Garcia, H., Locarnini, R., Zweng, M., Mishonov, A. V., Reagan, J., ... Smolyar, I. (2018). *World Ocean Atlas 2018.* NOAA National Centers for Environmental Information. Dataset. Retrieved from `https://www.ncei.noaa.gov/archive/accession/NCEI-WOA18`

Breeden, M. L., & McKinley, G. A. (2016). Climate impacts on multidecadal $p\mathrm{CO}_2$ variability in the North Atlantic: 1948–2009. *Biogeosciences*, *13*(11), 3387–3396. doi: 10.5194/bg-13-3387-2016

Brewer, P. G. (1978). Direct observation of the oceanic CO2 increase. *Geophysical Research Letters*, *5*(12), 997–1000. doi: 10.1029/GL005i012p00997

Broullón, D., Pérez, F. F., Velo, A., Hoppema, M., Olsen, A., Takahashi, T., ... van Heuven, S. M. A. C. (2019). A global monthly climatology of total alkalinity: a neural network approach. *Earth System Science Data*, *11*(3), 1109–1127. doi: 10.5194/essd-11-1109-2019

Broullón, D., Pérez, F. F., Velo, A., Hoppema, M., Olsen, A., Takahashi, T., ... Kozyr, A. (2020). A global monthly climatology of oceanic total dissolved inorganic carbon: a neural network approach. *Earth System Science Data*, *12*(3), 1725–1743. doi: 10.5194/essd-12-1725-2020

Carter, B. R., Feely, R. A., Wanninkhof, R., Kouketsu, S., Sonnerup, R. E., Pardo, P. C., ... Bullister, J. L. (2019). Pacific Anthropogenic Carbon Between 1991 and 2017. *Global Biogeochemical Cycles*, *33*(5), 597–617. doi: 10.1029/2018GB006154

Carter, B. R., Feely, R. A., Williams, N. L., Dickson, A. G., Fong, M. B., & Takeshita, Y. (2018). Updated methods for global locally interpolated estimation of alkalinity, pH, and nitrate. *Limnology and Oceanography: Methods*, *16*(2), 119–131. doi: 10.1002/lom3.10232

Chen, G.-T., & Millero, F. J. (1979). Gradual increase of oceanic CO 2. *Nature*, *277*(5693), 205–206. doi: 10.1038/277205a0

Cheng, L., Trenberth, K. E., Gruber, N., Abraham, J. P., Fasullo, J. T., Li, G., ... Zhu, J. (2020). Improved Estimates of Changes in Upper Ocean Salinity and the Hydrological Cycle. *American Meteorological Society Section: Journal of Climate*, *33*(23), 10357–10381. doi: 10.1175/JCLI-D-20-0366.1

Clement, D., & Gruber, N. (2018). The eMLR(C*) Method to Determine Decadal Changes in the Global Ocean Storage of Anthropogenic CO2. *Global Biogeochemical Cycles*, *32*(4), 654–679. doi: 10.1002/2017GB005819

DeVries, T., Holzer, M., & Primeau, F. (2017). Recent increase in oceanic carbon uptake driven by weaker upper-ocean overturning. *Nature*, *542*(7640), 215–218. doi: 10.1038/nature21068

Doney, S. C., Fabry, V. J., Feely, R. A., & Kleypas, J. A. (2009). Ocean Acidification: The Other CO2 Problem. *Annual Review of Marine Science*, *1*(1), 169–192. doi:

10.1146/annurev.marine.010908.163834
Dong, Y., Bakker, D. C. E., Bell, T. G., Huang, B., Landschützer, P., Liss, P. S., & Yang, M. (2022). Update on the Temperature Corrections of Global Air-Sea CO2 Flux Estimates. *Global Biogeochemical Cycles*, *36*(9), e2022GB007360. doi: 10.1029/2022GB007360
Dore, J. E., Lukas, R., Sadler, D. W., Church, M. J., & Karl, D. M. (2009). Physical and biogeochemical modulation of ocean acidification in the central North Pacific. *Proceedings of the National Academy of Sciences of the United States of America*, *106*(30), 12235–12240. doi: 10.1073/pnas.0906044106
Etopo2. (2001). ETOPO2, Global 2 Arc-minute Ocean Depth and Land Elevation from the US National Geophysical Data Center (NGDC). *National Geophysical Data Center/NESDIS/NOAA/U.S. Department of Commerce*. (Research Data Archive at the National Center for Atmospheric Research, Computational and Information Systems Laboratory [dataset]) doi: 10.5065/D6668B75
Fay, A. R., Gregor, L., Landschützer, P., McKinley, G. A., Gruber, N., Gehlen, M., ... Zeng, J. (2021). SeaFlux: harmonization of air–sea CO_2 fluxes from surface $p CO_2$ data products using a standardized approach. *Earth System Science Data*, *13*(10), 4693–4710. doi: 10.5194/essd-13-4693-2021
Fay, A. R., & McKinley, G. A. (2013). Global trends in surface ocean pCO2 from in situ data. *Global Biogeochemical Cycles*, *27*(2), 541–557. doi: 10.1002/gbc.20051
Feely, R. A., Sabine, C. L., Lee, K., Berelson, W., Kleypas, J., Fabry, V. J., & Millero, F. J. (2004). Impact of Anthropogenic CO2 on the CaCO3 System in the Oceans. *Science*, *305*(5682), 362–366. doi: 10.1126/science.1097329
Friedlingstein, P., Jones, M. W., O'Sullivan, M., Andrew, R. M., Bakker, D. C. E., Hauck, J., ... Zeng, J. (2022). Global Carbon Budget 2021. *Earth System Science Data*, *14*(4), 1917–2005. doi: 10.5194/essd-14-1917-2022
Friis, K., Körtzinger, A., Pätsch, J., & Wallace, D. W. R. (2005). On the temporal increase of anthropogenic CO2 in the subpolar North Atlantic. *Deep Sea Research Part I: Oceanographic Research Papers*, *52*(5), 681–698. doi: 10.1016/j.dsr.2004.11.017
Friis, K., Körtzinger, A., & Wallace, D. W. R. (2003). The salinity normalization of marine inorganic carbon chemistry data. *Geophysical Research Letters*, *30*(2). doi: 10.1029/2002GL015898
GlobalView-CO2. (2011). *Cooperative Atmospheric Data Integra- tion Project – Carbon Dioxide. Dataset.* Retrieved from `https://gml.noaa.gov/ccgg/globalview/`
Gloege, L., McKinley, G. A., Landschützer, P., Fay, A. R., Frölicher, T. L., Fyfe, J. C., ... Takano, Y. (2021). Quantifying Errors in Observationally Based Estimates of Ocean Carbon Sink Variability. *Global Biogeochemical Cycles*, *35*(4), e2020GB006788. doi: 10.1029/2020GB006788
Gray, A. R., Johnson, K. S., Bushinsky, S. M., Riser, S. C., Russell, J. L., Talley, L. D., ... Sarmiento, J. L. (2018). Autonomous biogeochemical floats detect significant carbon dioxide outgassing in the high-latitude Southern Ocean. *Geophysical Research Letters*. doi: 10.1029/2018GL078013
Gregor, L., & Gruber, N. (2021). OceanSODA-ETHZ: a global gridded data set of the surface ocean carbonate system for seasonal to decadal studies of ocean acidification. *Earth System Science Data*, *13*(2), 777–808. doi: 10.5194/essd-13-777-2021
Gregor, L., Kok, S., & Monteiro, P. M. S. (2017). Empirical methods for the estimation of Southern Ocean CO2: support vector and random forest regression. *Biogeosciences*, *14*(23), 5551–5569. doi: 10.5194/bg-14-5551-2017
Gruber, N. (1998). Anthropogenic CO2 in the Atlantic Ocean. *Global Biogeochemical Cycles*, *12*(1), 165–191. doi: 10.1029/97GB03658
Gruber, N., Bakker, D. C. E., DeVries, T., Gregor, L., Hauck, J., Landschützer, P., ... Mueller, J. D. (2023). Trends and variability in the ocean carbon sink. *Nature Reviews Earth and Environment*. doi: 10.1038/s43017-022-00381-x
Gruber, N., Clement, D., Carter, B. R., Feely, R. A., Heuven, S. v., Hoppema, M., ... Wanninkhof, R. (2019). The oceanic sink for anthropogenic CO2 from 1994 to 2007.

Science, *363*(6432), 1193–1199. doi: 10.1126/science.aau5153

Gruber, N., Gloor, M., Fletcher, S. E. M., Doney, S. C., Dutkiewicz, S., Follows, M. J., … Takahashi, T. (2009). Oceanic sources, sinks, and transport of atmospheric CO2. *Global Biogeochemical Cycles*, *23*(1). doi: 10.1029/2008GB003349

Gruber, N., Sarmiento, J. L., & Stocker, T. F. (1996). An improved method for detecting anthropogenic CO2 in the oceans. *Global Biogeochemical Cycles*, *10*(4), 809–837. doi: 10.1029/96GB01608

Hauck, J., Völker, C., Wang, T., Hoppema, M., Losch, M., & Wolf-Gladrow, D. A. (2013). Seasonally different carbon flux changes in the Southern Ocean in response to the southern annular mode. *Global Biogeochemical Cycles*, *27*(4), 1236–1245. doi: 10.1002/2013GB004600

Hauck, J., Zeising, M., Le Quéré, C., Gruber, N., Bakker, D. C. E., Bopp, L., … Séférian, R. (2020). Consistency and Challenges in the Ocean Carbon Sink Estimate for the Global Carbon Budget. *Frontiers in Marine Science*, *7*, 852. doi: 10.3389/fmars.2020.571720

Ilyina, T., Six, K. D., Segschneider, J., Maier-Reimer, E., Li, H., & Núñez-Riboni, I. (2013). Global ocean biogeochemistry model HAMOCC: Model architecture and performance as component of the MPI-Earth system model in different CMIP5 experimental realizations. *Journal of Advances in Modeling Earth Systems*, *5*(2), 287–315. doi: 10.1029/2012MS000178

IPCC. (2021). *Climate Change 2021: The Physical Science Basis. Contribution of Working Group I to the Sixth Assessment Report of the Intergovernmental Panel on Climate Change* (V. Masson-Delmotte et al., Eds.). Cambridge University Press.

Jacobson, A. R., Mikaloff Fletcher, S. E., Gruber, N., Sarmiento, J. L., & Gloor, M. (2007). A joint atmosphere-ocean inversion for surface fluxes of carbon dioxide: 1. Methods and global-scale fluxes. *Global Biogeochemical Cycles*, *21*(1). doi: 10.1029/2005GB002556

Joos, F., Plattner, G.-K., Stocker, T. F., Marchal, O., & Schmittner, A. (1999). Global Warming and Marine Carbon Cycle Feedbacks on Future Atmospheric CO2. *Science*, *284*(5413), 464–467. doi: 10.1126/science.284.5413.464

Keeling, R. (2005). Comment on "The Ocean Sink for Anthropogenic CO2". *Science*, *308*(5729), 1743c–1743c. doi: 10.1126/science.1109620

Keppler, L., & Landschützer, P. (2019). Regional Wind Variability Modulates the Southern Ocean Carbon Sink. *Scientific Reports*, *9*(1), 1–10. doi: 10.1038/s41598-019-43826-y

Keppler, L., Landschützer, P., Gruber, N., Lauvset, S. K., & Stemmler, I. (2020a). Mapped Observation-Based Oceanic dissolved inorganic carbon (DIC), monthly climatology, from January to December (based on observations between 2004 and 2017), from the Max-Planck-Institute for Meteorology (MOBO-DIC_mpim). Dataset. *NOAA National Centers for Environmental Information*, *NCEI Accession 0221526*. Retrieved from https://www.ncei.noaa.gov/access/metadata/landing-page/bin/iso?id=gov.noaa.nodc%3A0221526

Keppler, L., Landschützer, P., Gruber, N., Lauvset, S. K., & Stemmler, I. (2020b). Seasonal Carbon Dynamics in the Near-Global Ocean. *Global Biogeochemical Cycles*, *34*(12), e2020GB006571. doi: 10.1029/2020GB006571

Kerr, R. A. (2000). A North Atlantic Climate Pacemaker for the Centuries. *Science*, *288*(5473), 1984–1985. doi: 10.1126/science.288.5473.1984

Key, R. M., Kozyr, A., Sabine, C. L., Lee, K., Wanninkhof, R., Bullister, J. L., … Peng, T.-H. (2004). A global ocean carbon climatology: Results from Global Data Analysis Project (GLODAP). *Global Biogeochemical Cycles*, *18*(4). doi: 10.1029/2004GB002247

Lacroix, F., Ilyina, T., & Hartmann, J. (2020). Oceanic CO_2 outgassing and biological production hotspots induced by pre-industrial river loads of nutrients and carbon in a global modeling approach. *Biogeosciences*, *17*(1), 55–88. doi: 10.5194/bg-17-55-2020

Landschützer, P., Gruber, N., & Bakker, D. C. E. (2016). Decadal variations and trends of the global ocean carbon sink. *Global Biogeochemical Cycles*, *30*(10), 1396–1417. doi: 10.1002/2015GB005359

Landschützer, P., Gruber, N., Bakker, D. C. E., & Schuster, U. (2014). Recent variability of the global ocean carbon sink. *Global Biogeochemical Cycles*, *28*(9), 927–949. doi: 10.1002/2014GB004853

Landschützer, P., Gruber, N., Bakker, D. C. E., Schuster, U., Nakaoka, S., Payne, M. R., … Zeng, J. (2013). A neural network-based estimate of the seasonal to inter-annual variability of the Atlantic Ocean carbon sink. *Biogeosciences*, *10*(11), 7793–7815. doi: 10.5194/bg-10-7793-2013

Landschützer, P., Gruber, N., Haumann, A., Rödenbeck, C., Bakker, D. C. E., van Heuven, S., … Wanninkhof, R. (2015). The reinvigoration of the Southern Ocean carbon sink. *Science*, *349*(6253), 1221–1224. doi: 10.1126/science.aab2620

Landschützer, P., Keppler, L., & Ilyina, T. (2022). Chapter 13: Ocean Systems. In *Balancing Greenhouse Gas Budgets - Accounting for Natural and Anthropogenic Flows of CO2 and other Trace Gases* (1st ed.). Elsevier.

Lauvset, S. K., Key, R. M., Olsen, A., van Heuven, S., Velo, A., Lin, X., … Watelet, S. (2016). A new global interior ocean mapped climatology: the 1° × 1° GLODAP version 2. *Earth System Science Data*, *8*(2), 325–340. doi: 10.5194/essd-8-325-2016

Lauvset, S. K., Lange, N., Tanhua, T., Bittig, H. C., Olsen, A., Kozyr, A., … Key, R. M. (2021). An updated version of the global interior ocean biogeochemical data product, GLODAPv2.2021. *Earth System Science Data*, *13*(12), 5565–5589. doi: 10.5194/essd-13-5565-2021

Lenton, A., & Matear, R. J. (2007). Role of the Southern Annular Mode (SAM) in Southern Ocean CO2 uptake. *Global Biogeochemical Cycles*, *21*(2), GB2016. doi: 10.1029/2006GB002714

Le Quéré, C., Rödenbeck, C., Buitenhuis, E. T., Conway, T. J., Langenfelds, R., Gomez, A., … Heimann, M. (2007). Saturation of the Southern Ocean CO2 sink due to recent climate change. *Science*, *316*(5832), 1735–1738. doi: 10.1126/science.1136188

Lovenduski, N. S., Gruber, N., & Doney, S. C. (2008). Toward a mechanistic understanding of the decadal trends in the Southern Ocean carbon sink. *Global Biogeochemical Cycles*, *22*(3), GB3016. doi: 10.1029/2007GB003139

Lovenduski, N. S., Gruber, N., Doney, S. C., & Lima, I. D. (2007). Enhanced CO2 outgassing in the Southern Ocean from a positive phase of the Southern Annular Mode. *Global Biogeochemical Cycles*, *21*(2), GB2026. doi: 10.1029/2006GB002900

Mantua, N. J., & Hare, S. R. (2002). The Pacific Decadal Oscillation. *Journal of Oceanography*, *58*(1), 35–44. doi: 10.1023/A:1015820616384

Matear, R. J., & Hirst, A. C. (1999). Climate change feedback on the future oceanic CO2 uptake. *Tellus B: Chemical and Physical Meteorology*, *51*(3), 722–733. doi: 10.3402/tellusb.v51i3.16472

Matsumoto, K., & Gruber, N. (2005). How accurate is the estimation of anthropogenic carbon in the ocean? An evaluation of the DeltaC* method. *Global Biogeochemical Cycles*, *19*(3). doi: 10.1029/2004GB002397

Mauritsen, T., Bader, J., Becker, T., Behrens, J., Bittner, M., Brokopf, R., … Roeckner, E. (2019). Developments in the MPI-M Earth System Model version 1.2 (MPI-ESM1.2) and Its Response to Increasing CO2. *Journal of Advances in Modeling Earth Systems*, *11*(4), 998–1038. doi: 10.1029/2018MS001400

McKinley, G. A., Fay, A. R., Eddebbar, Y. A., Gloege, L., & Lovenduski, N. S. (2020). External Forcing Explains Recent Decadal Variability of the Ocean Carbon Sink. *AGU Advances*, *1*(2), e2019AV000149. doi: 10.1029/2019AV000149

McNeil, B. I., & Matear, R. J. (2013). The non-steady state oceanic CO_2 signal: its importance, magnitude and a novel way to detect it. *Biogeosciences*, *10*(4), 2219–2228. doi: 10.5194/bg-10-2219-2013

McNeil, B. I., & Sasse, T. P. (2016). Future ocean hypercapnia driven by anthropogenic amplification of the natural CO2 cycle. *Nature*, *529*(7586), 383–386. doi: 10.1038/nature16156

Mikaloff Fletcher, S. E. M., Gruber, N., Jacobson, A. R., Doney, S. C., Dutkiewicz, S., Gerber, M., … Sarmiento, J. L. (2006). Inverse estimates of anthropogenic CO2 uptake, transport, and storage by the ocean. *Global Biogeochemical Cycles*, *20*(2), GB2002. doi: 10.1029/2005GB002530

Olsen, A., Key, R. M., Heuven, S. v., Lauvset, S. K., Velo, A., Lin, X., … Suzuki, T. (2016). The Global Ocean Data Analysis Project version 2 (GLODAPv2) – an internally consistent data product for the world ocean. *Earth System Science Data*, *8*(2), 297–323. doi: 10.5194/essd-8-297-2016

Orr, J. C., Fabry, V. J., Aumont, O., Bopp, L., Doney, S. C., Feely, R. A., … Yool, A. (2005). Anthropogenic ocean acidification over the twenty-first century and its impact on calcifying organisms. *Nature*, *437*(7059), 681–686. doi: 10.1038/nature04095

Regnier, P., Resplandy, L., Najjar, R. G., & Ciais, P. (2022). The land-to-ocean loops of the global carbon cycle. *Nature*, *603*(7901), 401–410. doi: 10.1038/s41586-021-04339-9

Resplandy, L., Keeling, R. F., Rödenbeck, C., Stephens, B. B., Khatiwala, S., Rodgers, K. B., … Tans, P. P. (2018). Revision of global carbon fluxes based on a reassessment of oceanic and riverine carbon transport. *Nature Geoscience*, 1. doi: 10.1038/s41561-018-0151-3

Roemmich, D., & Gilson, J. (2009). The 2004-2008 mean and annual cycle of temperature, salinity, and steric height in the global ocean from the Argo Program. *Progress in Oceanography*, *82*(2), 81–100. doi: 10.1016/j.pocean.2009.03.004

Roobaert, A., Laruelle, G. G., Landschützer, P., Gruber, N., Chou, L., & Regnier, P. (2019). The Spatiotemporal Dynamics of the Sources and Sinks of CO2 in the Global Coastal Ocean. *Global Biogeochemical Cycles*, *33*(12), 1693–1714. doi: 10.1029/2019GB006239

Rödenbeck, C., Bakker, D. C. E., Gruber, N., Iida, Y., Jacobson, A. R., Jones, S., … Zeng, J. (2015). Data-based estimates of the ocean carbon sink variability – first results of the Surface Ocean pCO2 Mapping intercomparison (SOCOM). *Biogeosciences*, *12*(23), 7251–7278. doi: 10.5194/bg-12-7251-2015

Sabine, C. L., Feely, R. A., Gruber, N., Key, R. M., Lee, K., Bullister, J. L., … Rios, A. F. (2004). The oceanic sink for anthropogenic CO2. *Science*, *305*(5682), 367–371. doi: 10.1126/science.1097403

Sabine, C. L., & Gruber, N. (2005). Response to Comment on "The Ocean Sink for Anthropogenic CO2". *Science*, *308*(5729), 1743–1743. doi: 10.1126/science.1109949

Sabine, C. L., Key, R. M., Johnson, K. M., Millero, F. J., Poisson, A., Sarmiento, J. L., … Winn, C. D. (1999). Anthropogenic CO2 inventory of the Indian Ocean. *Global Biogeochemical Cycles*, *13*(1), 179–198. doi: 10.1029/1998GB900022

Sarmiento, J. L., & Gruber, N. (2002). Sinks for Anthropogenic Carbon. *Physics Today*, *55*(8), 30–36. doi: 10.1063/1.1510279

Sarmiento, J. L., & Gruber, N. (2006). Carbon Cycle, CO2, and Climate; the Anthropogenic Perturbation. In *Ocean Biogeochemical Dynamics* (pp. 399–417). Princeton University Press.

Sarmiento, J. L., Hughes, T. M. C., Stouffer, R. J., & Manabe, S. (1998). Simulated response of the ocean carbon cycle to anthropogenic climate warming. *Nature*, *393*(6682), 245–249. doi: 10.1038/30455

Sarmiento, J. L., Le Quéré, C., & Pacala, S. W. (1995). Limiting future atmospheric carbon dioxide. *Global Biogeochemical Cycles*, *9*(1), 121–137. doi: 10.1029/94GB01779

Sarmiento, J. L., & Sundquist, E. T. (1992). Revised budget for the oceanic uptake of anthropogenic carbon dioxide. *Nature*, *356*(6370), 589–593. doi: 10.1038/356589a0

Sasse, T. P., McNeil, B. I., & Abramowitz, G. (2013). A novel method for diagnosing seasonal to inter-annual surface ocean carbon dynamics from bottle data using neural networks. *Biogeosciences*, *10*(6), 4319–4340. doi: 10.5194/bg-10-4319-2013

Sharp, J. D., Fassbender, A. J., Carter, B. R., Johnson, G. C., Schultz, C., & Dunne, J. P. (2022). GOBAI-O_2: temporally and spatially resolved fields of ocean interior dissolved oxygen over nearly two decades. *Earth System Science Data Discussions*, 1–46. doi: 10.5194/essd-2022-308

Talley, L., Feely, R., Sloyan, B., Wanninkhof, R., Baringer, M., Bullister, J., … Zhang, J.-Z. (2016). Changes in Ocean Heat, Carbon Content, and Ventilation: A Review of the First Decade of GO-SHIP Global Repeat Hydrography. *Annual Review of Marine Science*, *8*(1), 185–215. doi: 10.1146/annurev-marine-052915-100829

Talley, L., Rosso, I., Kamenkovich, I., Mazloff, M. R., Wang, J., Boss, E., . . . Sarmiento, J. L. (2019). Southern Ocean Biogeochemical Float Deployment Strategy, With Example From the Greenwich Meridian Line (GO-SHIP A12). *Journal of Geophysical Research: Oceans*, *124*(1), 403–431. doi: 10.1029/2018JC014059

Tanhua, T., Körtzinger, A., Friis, K., Waugh, D. W., & Wallace, D. W. R. (2007). An estimate of anthropogenic CO2 inventory from decadal changes in oceanic carbon content. *Proceedings of the National Academy of Sciences*, *104*(9), 3037–3042. doi: 10.1073/pnas.0606574104

Terhaar, J., Frölicher, T. L., & Joos, F. (2022). Observation-constrained estimates of the global ocean carbon sink from Earth System Models. *Biogeosciences Discussions*, 1–49. doi: 10.5194/bg-2022-134

Torres, O., Kwiatkowski, L., Sutton, A. J., Dorey, N., & Orr, J. C. (2021). Characterizing Mean and Extreme Diurnal Variability of Ocean CO2 System Variables Across Marine Environments. *Geophysical Research Letters*, *48*(5), e2020GL090228. doi: 10.1029/2020GL090228

Turner, K. E., Smith, D. M., Katavouta, A., & Williams, R. G. (2022). Reconstructing ocean carbon storage with CMIP6 models and synthetic Argo observations. *Biogeosciences Discussions*, 1–29. doi: 10.5194/bg-2022-166

van Heuven, S., Pierrot, D., Rae, J., Lewis, E., & Wallace, D. (2011). *MATLAB Program Developed for CO2 System Calculations.* Oak Ridge, Tennessee: ORNL/CDIAC-105b. Carbon Dioxide Information Analysis Center, Oak Ridge National Laboratory, U.S. Department of Energy,.

Wallace, D. W. (1995). Monitoring global ocean carbon inventories. In *Scientific Design for the Common Module of the Global Ocean Observing System and the Global Climate Observing System: An Ocean Observing System for Climate : Final Report of the Ocean Observing System Development Panel.* Texas A&M University.

Wanninkhof, R., Asher, W. E., Ho, D. T., Sweeney, C., & McGillis, W. R. (2009). Advances in Quantifying Air-Sea Gas Exchange and Environmental Forcing. *Annual Review of Marine Science*, *1*(1), 213–244. doi: 10.1146/annurev.marine.010908.163742

Wanninkhof, R., Doney, S. C., Bullister, J. L., Levine, N. M., Warner, M., & Gruber, N. (2010). Detecting anthropogenic CO2 changes in the interior Atlantic Ocean between 1989 and 2005. *Journal of Geophysical Research: Oceans*, *115*(C11). doi: 10.1029/2010JC006251

Watson, A. J., Schuster, U., Shutler, J. D., Holding, T., Ashton, I. G. C., Landschützer, P., . . . Goddijn-Murphy, L. (2020). Revised estimates of ocean-atmosphere CO2 flux are consistent with ocean carbon inventory. *Nature Communications*, *11*(1), 4422. doi: 10.1038/s41467-020-18203-3

Wolter, K., & Timlin, M. S. (2011). El Niño/Southern Oscillation behaviour since 1871 as diagnosed in an extended multivariate ENSO index (MEI.ext). *International Journal of Climatology*, *31*(7), 1074–1087. doi: 10.1002/joc.2336

Zickfeld, K., Fyfe, J. C., Saenko, O. A., Eby, M., & Weaver, A. J. (2007). Response of the global carbon cycle to human-induced changes in Southern Hemisphere winds. *Geophysical Research Letters*, *34*(12). doi: 10.1029/2006GL028797

Figure 1.

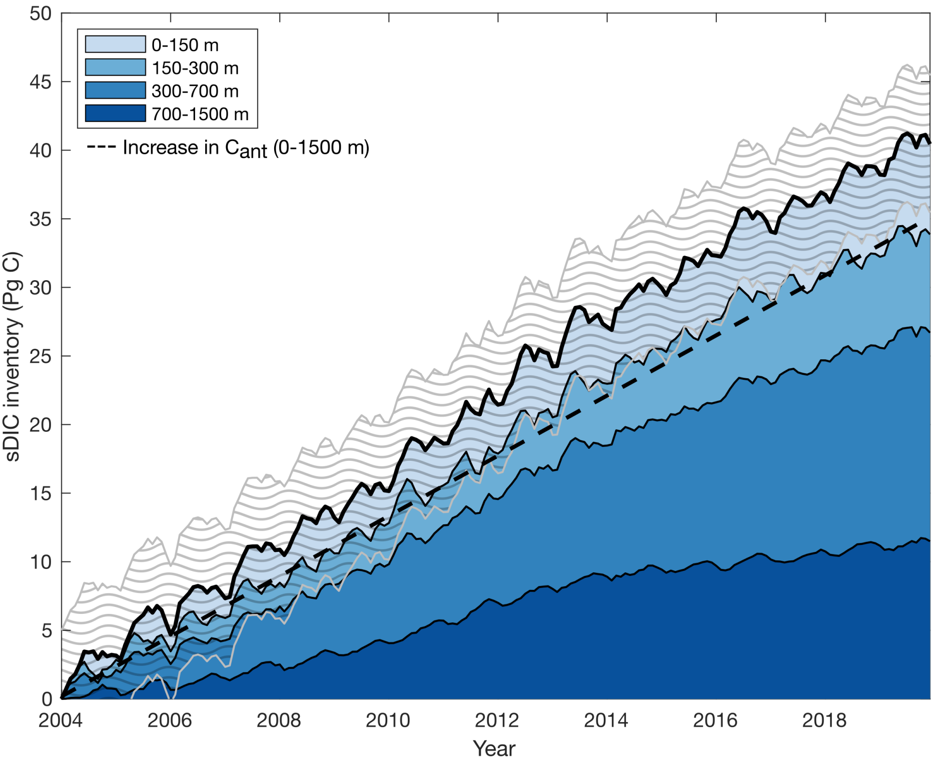
0-150 m
150-300 m
300-700 m
700-1500 m
Increase in C_{ant} (0-1500 m)
sDIC inventory (Pg C)
Year
0
5
10
15
20
25
30
35
40
45
50
2004
2006
2008
2010
2012
2014
2016
2018

Figure 2.

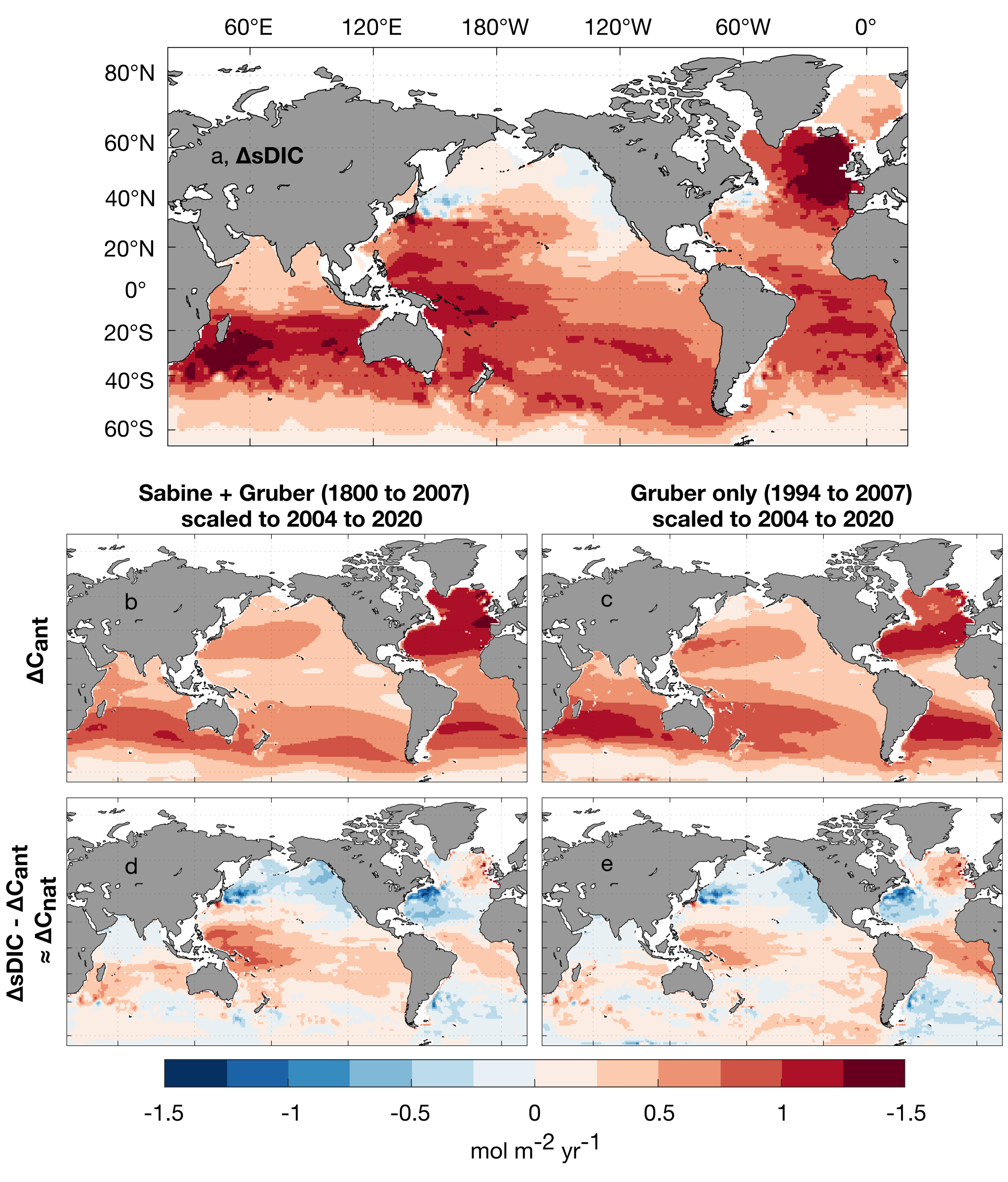
60°E
120°E
180°W
120°W
60°W
0°
80°N
60°N
40°N
20°N
0°
20°S
40°S
60°S
a, ΔsDIC
Sabine + Gruber (1800 to 2007)
scaled to 2004 to 2020
Gruber only (1994 to 2007)
scaled to 2004 to 2020
ΔC_{ant}
b
c
$\Delta sDIC - \Delta C_{ant}$
$\approx \Delta C_{nat}$
d
e
-1.5
-1
-0.5
0
0.5
1
-1.5
mol m^{-2} yr^{-1}

Figure 3.

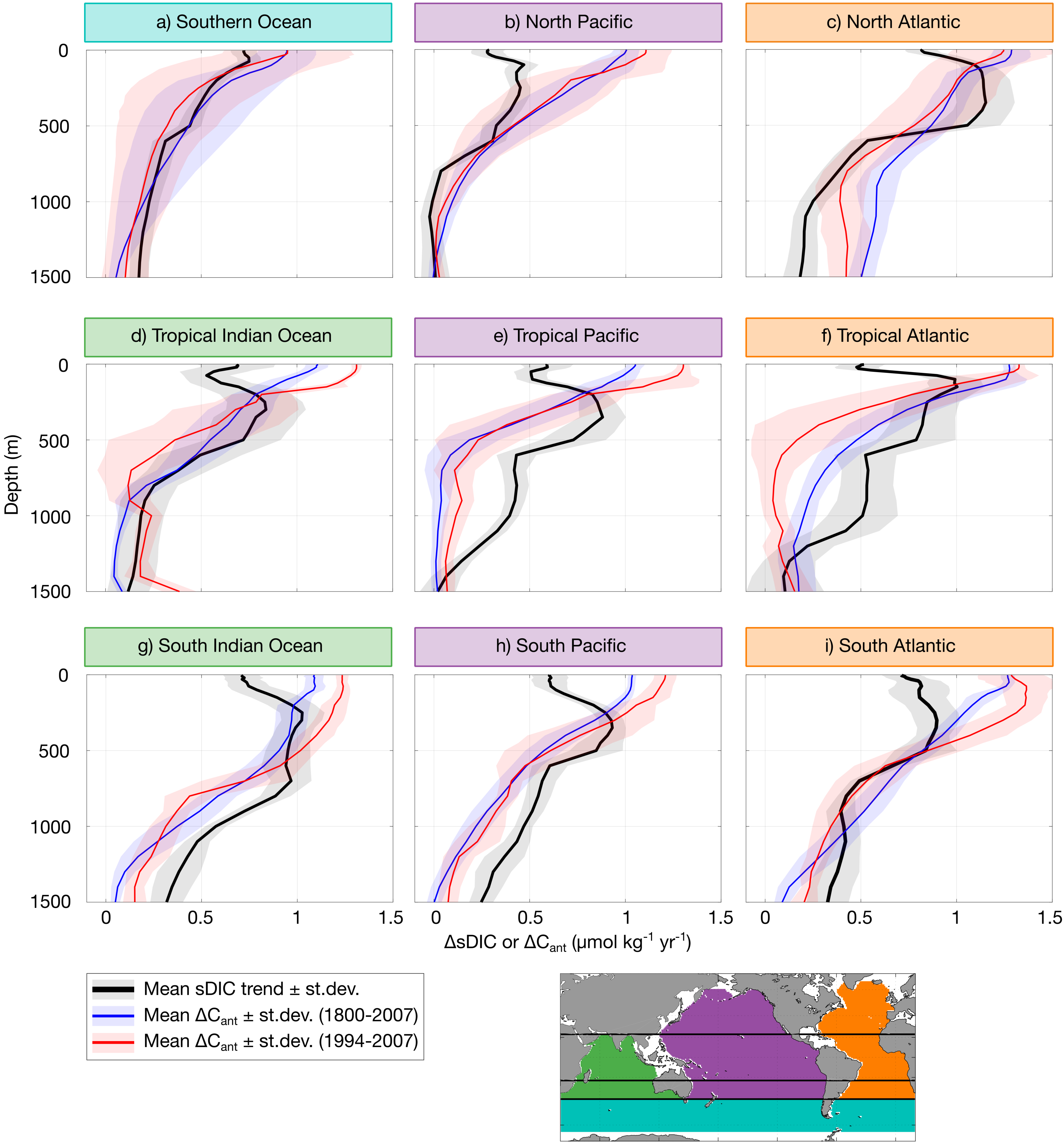
a) Southern Ocean
b) North Pacific
c) North Atlantic
d) Tropical Indian Ocean
e) Tropical Pacific
f) Tropical Atlantic
g) South Indian Ocean
h) South Pacific
i) South Atlantic
Depth (m)
0
500
1000
1500
0
0.5
1
1.5
ΔsDIC or ΔC_{ant} ($\mu mol\ kg^{-1}\ yr^{-1}$)
Mean sDIC trend ± st.dev.
Mean ΔC_{ant} ± st.dev. (1800-2007)
Mean ΔC_{ant} ± st.dev. (1994-2007)

Figure 4.

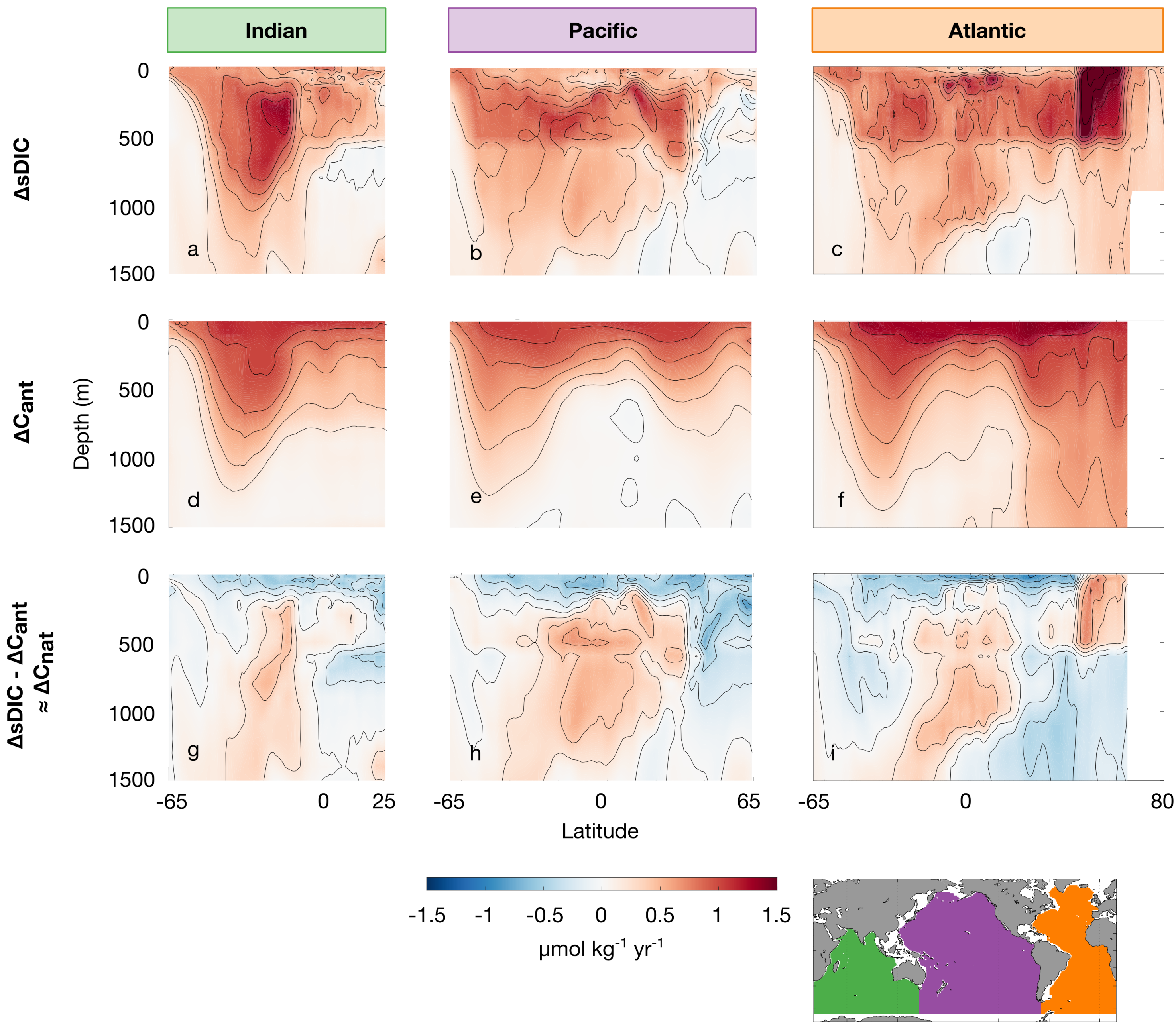

Indian
Pacific
Atlantic
ΔsDIC
ΔCant
ΔsDIC - ΔCant ≈ ΔCnat
Depth (m)
0
500
1000
1500
a
b
c
d
e
f
g
h
i
-65
0
25
-65
0
65
-65
0
80
Latitude
-1.5
-1
-0.5
0
0.5
1
1.5
μmol kg-1 yr-1

Figure 5.

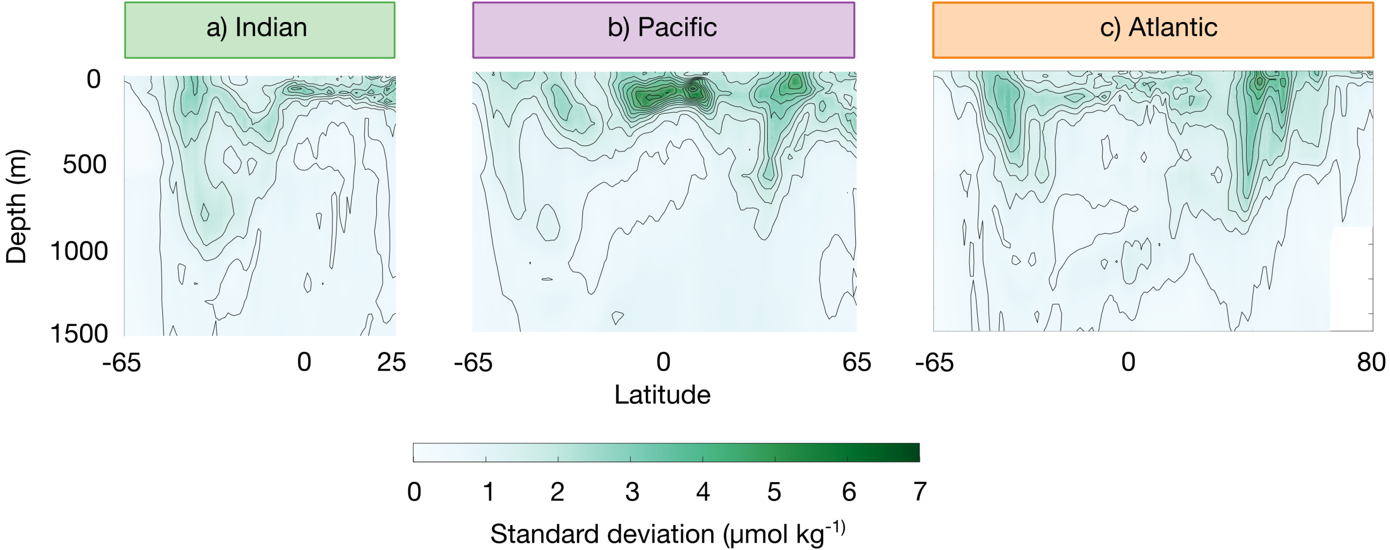

a) Indian
b) Pacific
c) Atlantic
Depth (m)
0
500
1000
1500
-65
0
25
-65
0
65
-65
0
80
Latitude
0
1
2
3
4
5
6
7
Standard deviation (μmol kg-1)

Figure 6.

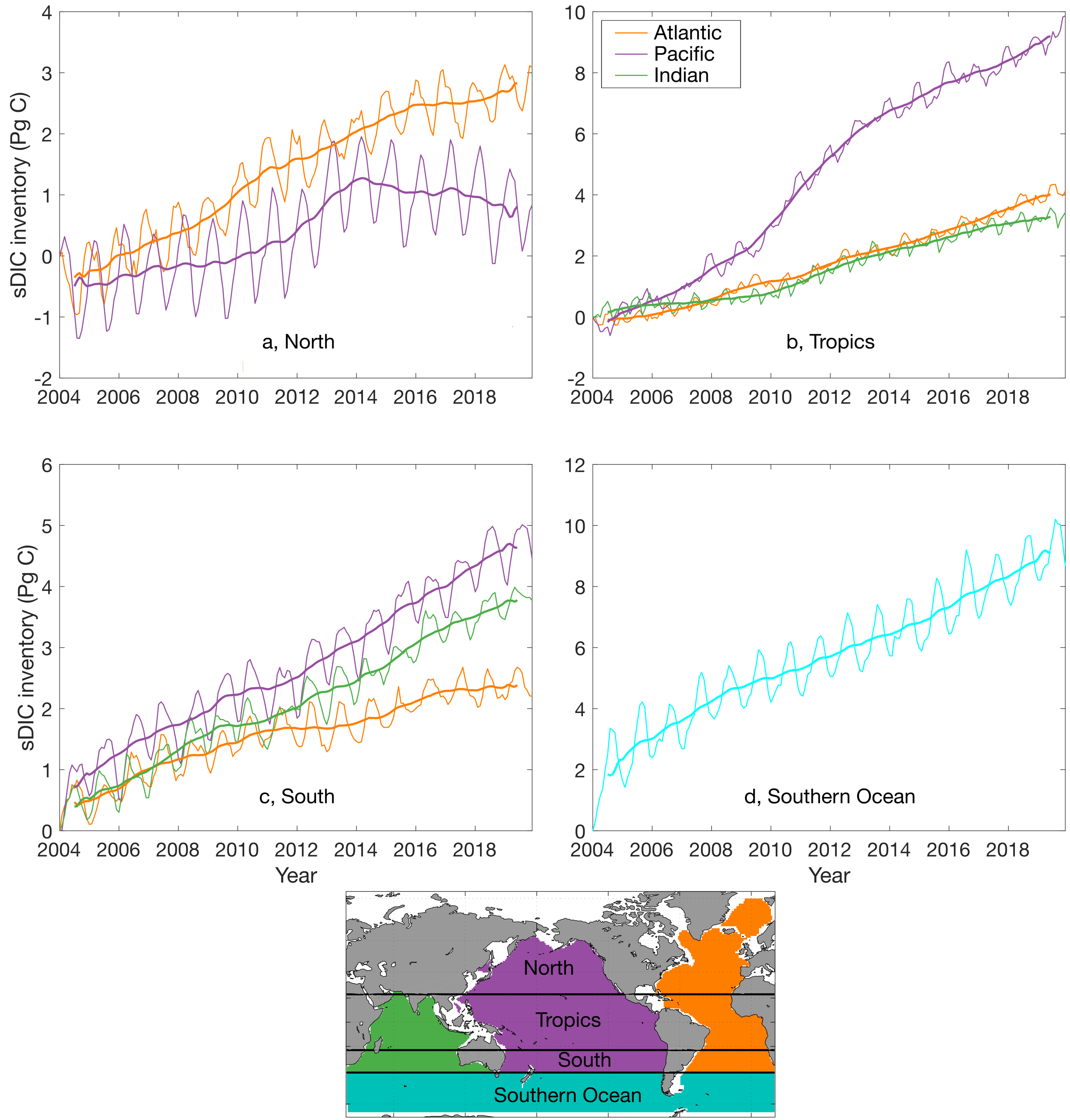
sDIC inventory (Pg C)
Year
Atlantic
Pacific
Indian
a, North
b, Tropics
c, South
d, Southern Ocean
North
Tropics
South
Southern Ocean

Table 1.

Compared data set	Type of data	Bias (µmol kg^{-1})	RMSD (µmol kg^{-1})	MOBO-DIC uncertainty (µmol kg^{-1})	Comparison uncertainty (µmol kg^{-1})
GLODAPv2.2021	Ship data, without interpolation or mapping (used to train the network)	0	16	18	2
Lauvset climatology	Global climatology (optimal interpolation)	7	17	18	7
Broullón climatology	Global monthly climatology (single-step neural network)	10	17	18	N/A
MOBO-DIC_{clim}	Global monthly climatology (cluster-regression)	11	20	18	9
HAMOCC	Synthetic data	-1	12	18	N/A
BATS	Time-series station	12	17	17	2
HOT	Time-series station	-4	15	17	2
Drake Passage	Time-series station (surface)	16	42	18	1
SOCCOM floats	Calculated DIC from BGC floats (pH) with LIAR algorithm	-5	14	17	6
OceanSODA-ETHZ	Global surface estimate (cluster-regression)	4	15	18	21

Table 2.

	Compared data set → Depth ↓	BATS	MOBO-DIC at BATS	HOT	MOBO-DIC at HOT	Drake Passage (surface)	MOBO-DIC at Drake Passage	SOCCOM floats	MOBO-DIC at SOCCOM floats
Trend	20 – 40 m	1	7	5	2	8	1	-20	-9
	100 – 150 m	3	8	13	6	N/A	N/A	3	1
	600 -800 m	16	5	4	5	N/A	N/A	19	26
IAV	20 – 40 m	5	2	11	4	9	5	4	3
	100 – 150 m	4	2	6	2	N/A	N/A	2	2
	600 -800 m	4	1	3	1	N/A	N/A	3	3

Supporting Information for

Trends and Interannual Variability in the Dissolved Inorganic Carbon Pool

S1: Domain

We demonstrate the horizontal domain of MOBO-DIC (this study) in Fig. S1, highlighting that compared to the monthly climatology of MOBO-DIC (Keppler et al., 2020), the domain has increased due to an increase in the domain of the Argo-based temperature and salinity fields we use as predictors (Roemmich & Gilson, 2009). While the monthly climatology of MOBO-DIC extended from 65° N to 65° S, MOBO-DIC extends up to 80° N in the Atlantic. Additionally, some coastal zones that were previously masked are now included.

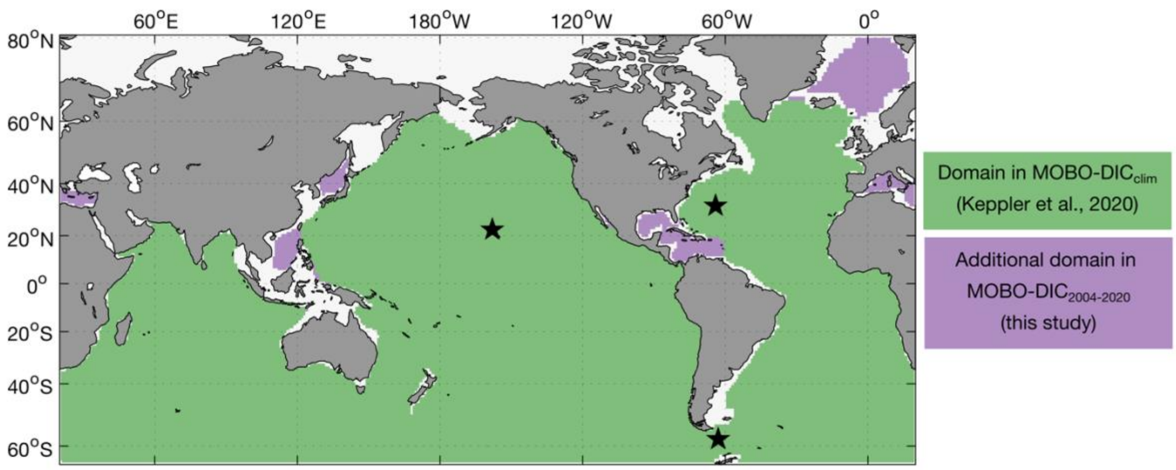

Figure S1: Horizontal domain of MOBO-DIC. Green areas illustrate the domain in the monthly climatology of MOBO-DIC, while the purple regions illustrate the additional regions in MOBO-DIC (this study). Black stars mark the location of the BATS, HOT, and Drake Passage time-series stations (from north to south), which are discussed in Section S5.2.

S2: Clusters

We apply an ensemble approach, where we create an ensemble of SOM-clusters to avoid boundary problems, following Gregor & Gruber (2021). Fig. S2 illustrates first the shape of the clusters and then demonstrates that the clusters are most variable around the boundaries.

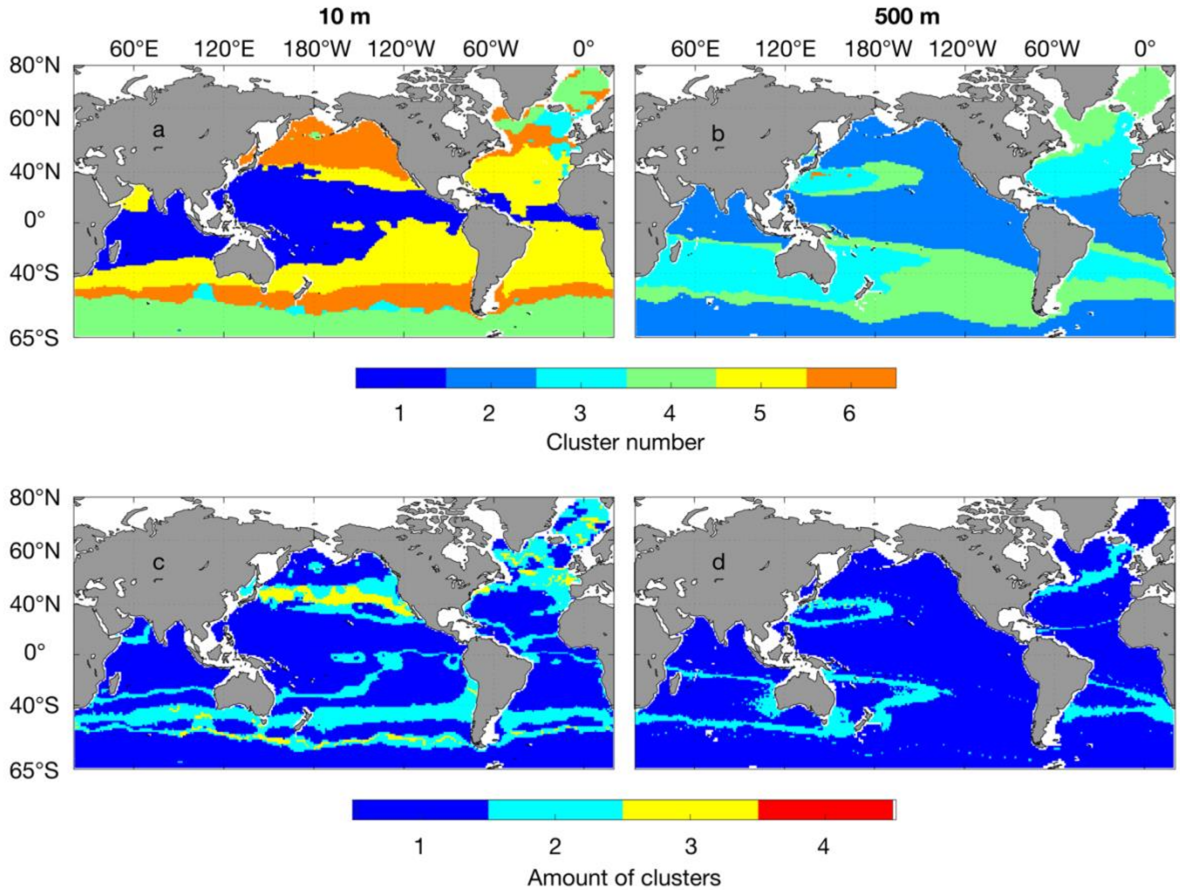

Figure S2. Shape and variability of the clusters. Maps of the clusters in January 2004 on 2 depth levels (a,b), and the number of different clusters at the same depth levels (c,d) at 10 m (a,c) and 500 m (b,d).

S3: Global upscaling of the inventory changes

After calculating the change in the integrated trend i.e., the inventory change in our study domain, we conduct an upscaling to estimate the global changes in the salinity-normalized DIC (sDIC) that includes regions beyond our domain, i.e., the high latitudes, coastal regions, and below 1500 m. For the high latitudes and coastal regions that are masked in MOBO-DIC, we take the global mean trend of MOBO-DIC at each depth level and assume the masked grid cells have the same trend at these depth levels and calculate the vertical integral in these regions. As the trend in sDIC decreases with depth in the upper 1500 m, we assume that the trend below 1500 m continues to weaken with depth and propose that between 1500 m and 4000 m the trend should be between 0 and the trend at 1500 m. We thus calculate the vertical integral between 1500 m and 4000 m, using the trend at each latitude-longitude grid cell at 1500 m in the remaining water column. We add half of that amount to our estimate and add the remaining half to the uncertainty to our global upscaled estimate. As discussed further below, our estimate of the sDIC trend between 1500 m and 4000 m yields 6±6 Pg C during our study period, i.e., 0.4±0.4 Pg C yr^{-1}. This estimate is higher than the increase in C_{ant} between 1994 and 2007 in the same depth range, which amounts to approximately 3±0.4 Pg C, i.e., 0.2±0.0 Pg C yr^{-1}. In the assumption that most of the long-term changes are anthropogenic, our estimate of the positive trend in DIC between 1500 m and 4000 m might be overestimated, but within the uncertainties. To obtain the depth until where we vertically integrate, we use the bathymetry from Etopo2 (2001). Previous studies have found that there is no significant increase in C_{ant} below 4000 m (Gruber et al., 2019). It is possible that there are changes in the natural carbon (C_{nat}) below 4000 m, however, we are unable to quantify this contribution here. As the trend in sDIC decreases with depth in the upper 1500 m, we assume no significant trend in the total sDIC below 4000 m.

S4: Uncertainties

The prediction uncertainty, which we define as the uncertainty linked to our method, is highlighted in Fig. S3. This uncertainty is estimated as the standard deviation across the 15-member ensemble from our bootstrapping approach. Note that the overall uncertainty of our product is, however, higher than the prediction uncertainty as described in Eq. 1 of the Main Text. In addition, Fig. S3 illustrates the temporal mean of the prediction uncertainty. At a single point in time, the prediction uncertainty may differ from this mean.

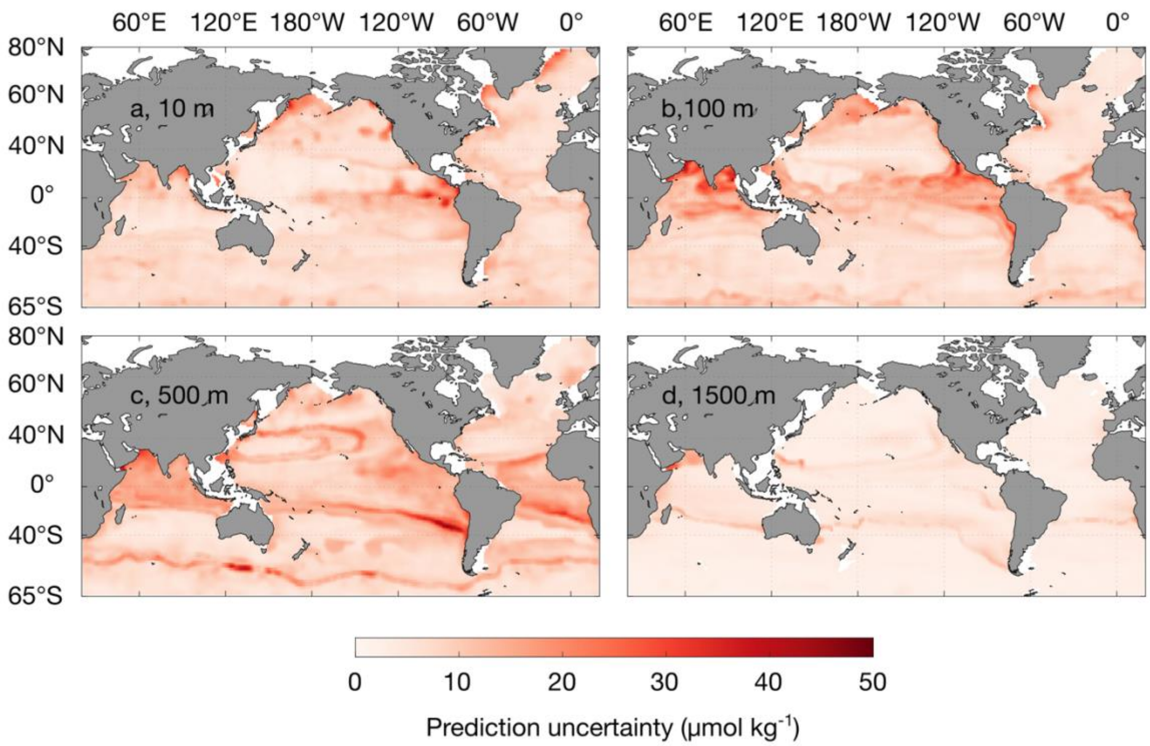

Figure S3. Maps of the prediction uncertainty of MOBO-DIC on four depth levels: (a) 10, (b) 100, (c) 500, and (d) 1500 m.

S5: Comparison with the state of the art

S5.1: Residuals from the GLODAP data

Unlike an interpolation, our mapping method estimates the target data at all grid points, while minimizing the difference between the target data (i.e., GLODAPv2.2021) and the mapped estimate (i.e., MOBO-DIC). Thus, there is a difference between the GLODAP data and MOBO-DIC. Here, we present these residuals to get a better handle on the quality of our fits (Fig. S4). We calculate the residuals by subtracting the GLODAP data at each point in time and space from our MOBO-DIC estimate. In the maps below we display the temporal mean of these residuals on different depth levels. While some regions have a positive bias, others have a negative one, leading to a global mean bias of 0. The same regions can show different residuals at different depths and there is also no indication of certain depth levels being more prone to over- or underestimate. The global mean root mean square difference (RMSD) between GLODAP and MOBO-DIC is 16 μmol kg^{-1}.

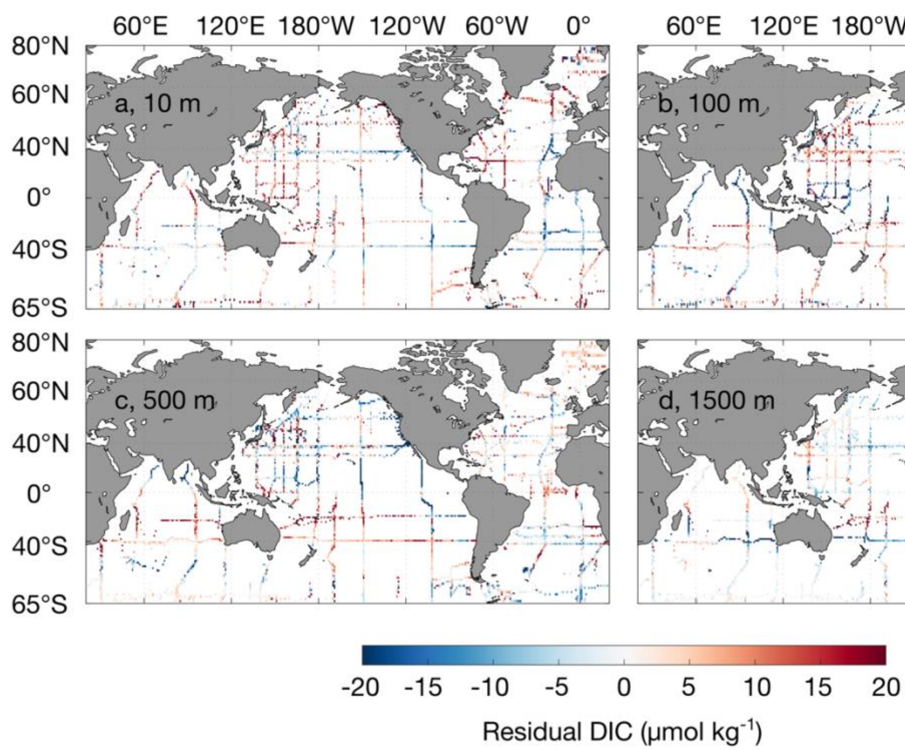

Figure S4. Maps of the temporal mean residuals (MOBO-DIC – GLODAP) at (a) 10, (b) 100, (c) 500, and (d) 1500 m.

S5.2 Climatologies (Lauvset, Broullón, climatology of MOBO-DIC)

The current state-of-the art climatology of global-scale DIC was created by Lauvset et al. (2016), who optimally interpolated GLODAPv2 ship data to create an annual-mean climatology of DIC in the upper 5500 m of the ocean. Recently, Broullón et al. (2020) and Keppler et al. (2020) used machine learning approaches to create monthly climatologies of DIC, the first global-scale time-varying DIC fields in the upper ocean. Although the climatologies cannot be used to assess the interannual variability of MOBO-DIC, we use these data sets to assess the differences in the temporal mean distribution (Lauvset et al., 2016), and the seasonal cycles (Broullón et al., 2020; Keppler et al., 2020) as a first order test of our method in comparison to the state of the art at lower temporal resolution.

In the upper ~200 m, MOBO-DIC tends to yield higher DIC concentrations than the Lauvset-climatology (differences up to ~50 µmol kg^{-1}), except for the northern Indian Ocean, which has lower values in the upper ~600 m (Fig. S5). Below ~200 m, the differences between the two products are smaller and both positive and negative. Similar differences were observed when comparing climatology of MOBO-DIC (Keppler et al., 2020) with the Lauvset climatology (Supporting Information of Keppler et al., 2020). The higher surface concentrations in both MOBO-DIC_{clim} and MOBO-DIC can be largely attributed to the fact that MOBO-DIC covers a later period (2004-2018 and 2004-2020, for the climatology and this study, respectively) than the Lauvset climatology, which is normalized to the year 2002. We expect other differences between the two products to be due to different data used (i.e., Lauvset use data from before 2004), as well as difference in the mapping method. This is further discussed in the Supporting Information of Keppler et al. (2020).

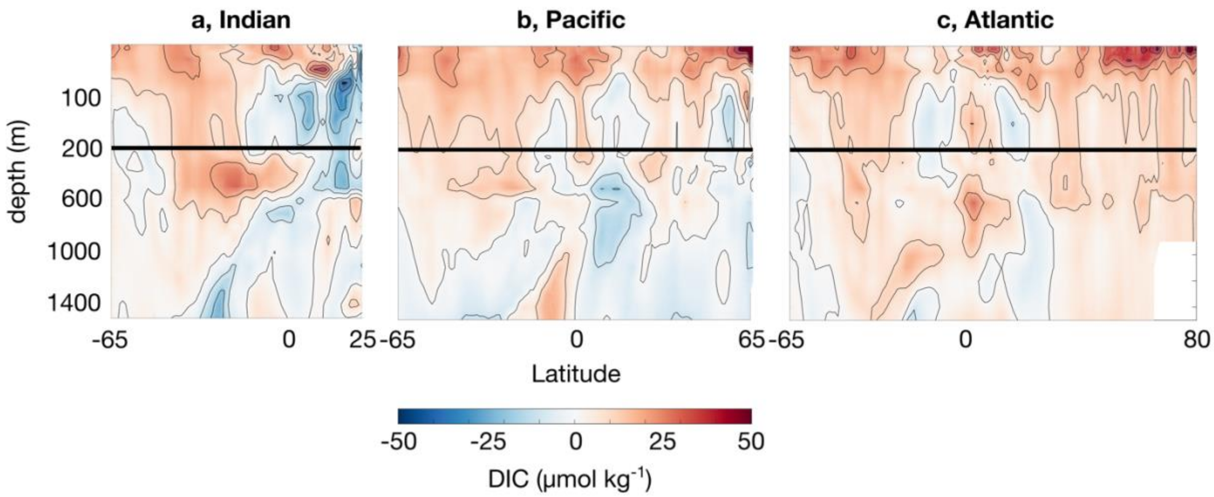

Figure S5: Zonal mean difference between the mean DIC in the climatology by Lauvset et al. (2016) and MOBO-DIC (MOBO-DIC - Lauvset) as a function of latitude (x-axis) and depth (y-axis), in the Indian (a), Pacific (b), and Atlantic Ocean (c). Zoomed into the upper 200 m.

The comparison of the seasonal cycle of DIC with the existing monthly climatologies is encouraging: the three products agree on the distribution and magnitude of the amplitude and phase (Fig. S6). In all products, the largest surface amplitudes are in the north Pacific (more than 50 µmol kg^{-1}), while the Labrador Sea, equatorial East Pacific and equatorial East Atlantic also have elevated surface amplitudes (Fig. S6 a-c). The seasonal maxima tend to be in hemispheric winter, due to deeper mixed layers in winter. The magnitude of the seasonal cycle tends to be weakest near the equator and largest near the poles due to the strength in seasonal forcing. The processes behind these patterns are described in more detail Keppler et al. (2020).

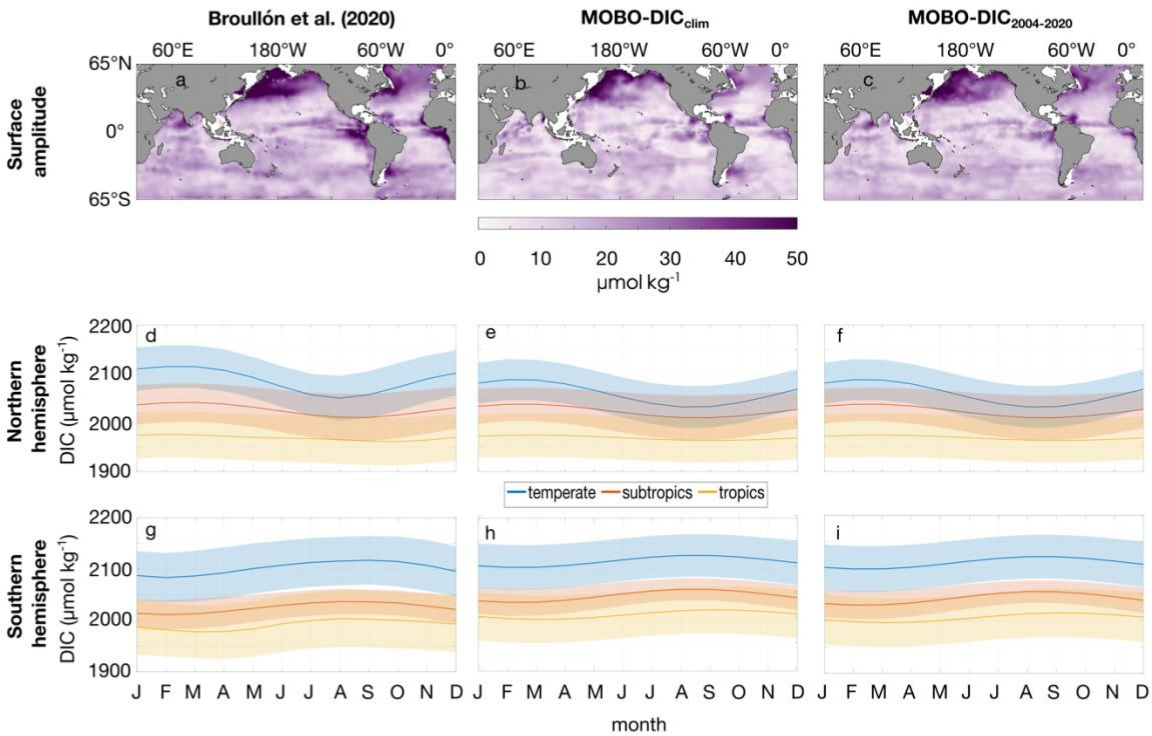

Figure S6: Amplitude of the seasonal cycle of DIC at 2.5 m in the monthly climatology by Broullón et al. (2020) (a), climatology of MOBO-DIC (b), and MOBO-DIC (c). The mean seasonal cycle in climatic zones in the northern (d-f) and southern hemisphere (g-i) for the same three datasets (Broullón et al. (2020) (d,g), climatology of MOBO-DIC (e,h), and MOBO-DIC (f,i). Temperate is from 35° to 65°, subtropics from 23° to 35°, tropics from 0° to 23°, for each hemisphere. Shading illustrates the standard deviation in the latitude-longitude space.

S6: Comparison with independent data

S6.1 Comparison with synthetic data (HAMOCC)

To date, there is no estimate of monthly inter-annually varying mapped fields of interior DIC at a global scale. We therefore conduct an assessment with synthetic data from the ocean biogeochemical model HAMOCC (Ilyina et al., 2013; Mauritsen et al., 2019). Here, we subsample the full model field of sDIC in the HAMOCC model at the time and location where we have observations of DIC in GLODAPv2.2021, and then run our cluster-regression method to recreate the full model field of sDIC. We then compare our sDIC reconstruction in HAMOCC with the actual sDIC in HAMOCC at every grid cell. Please refer to Keppler et al. (2020) and its Supporting Information for a more detailed description of this method with synthetic data.

The trend in sDIC in HAMOCC and our MOBO-DIC reconstruction of HAMOCC display very comparable spatial patterns (Fig. S7). There are both regions of under estimation and over estimation of the trend, indicating that there is no systematic bias in our method. When comparing the depth-integrated change in sDIC, we find again that in most regions, the spatial distributions agree well. However, in the eastern tropical Pacific, the trend is higher in our MOBO-DIC reconstruction of HAMOCC, than in HAMOCC. This difference mostly comes from the deep ocean between 1000 and 1500 m, where we find strong positive trends, that seem to be artifactual, possibly due to overfitting in our estimate with synthetic data (Fig. S7i). However, our estimate with real observations does not have these large positive trends at depth (see Fig. 1 in the Main Text), indicating that this is only a feature in our estimate with synthetic data. Integrated over the whole domain, the total increase in sDIC in the upper 1500 m is 1.7 Pg C yr^{-1} in the HAMOCC model, and 1.9 Pg C yr^{-1} in our MOBO-DIC reconstruction of HAMOCC. The larger increase in our MOBO-DIC reconstruction of HAMOCC is mostly due to the artifact at depth accumulating in the vertical integration.

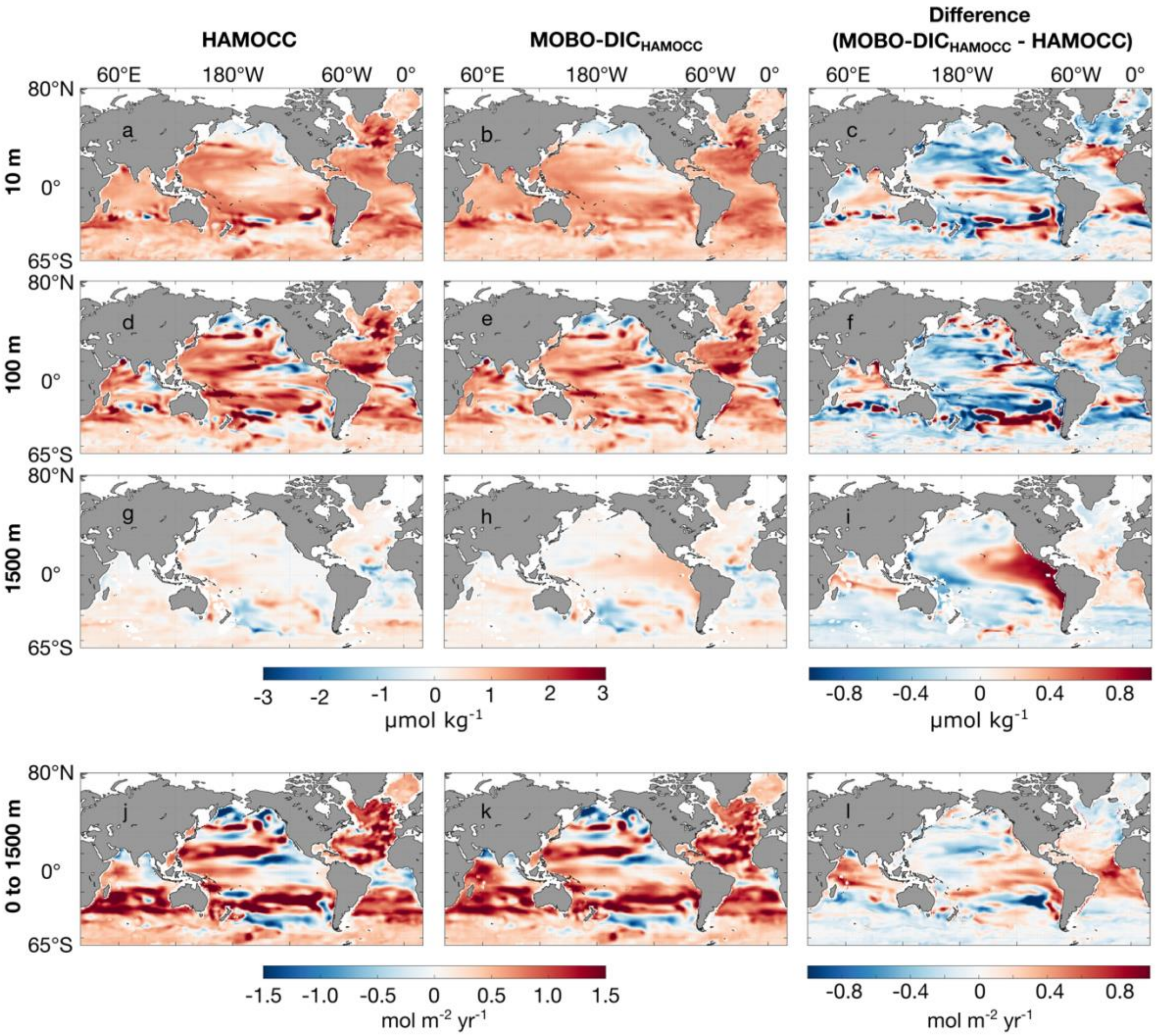

Figure S7: Spatial distribution of the decadal trend of sDIC in HAMOCC (a,d,g), our MOBO-DIC reconstruction of HAMOCC with synthetic data (b,e,h), and the difference between the two (c,f,i) at 10 m (a-c), 100 m (d-f), and vertically integrated decadal trend in the upper 1500 m (g-i).

Our MOBO-DIC method run with synthetic data also captures the patterns and magnitude of the interannual variability of sDIC in HAMOCC well (Fig. S8). Although in some regions, MOBO-DIC over- or underestimates the variability, there is no systemic bias in one direction. Similar as with the trend, we find an over estimation of the interannual variability in our MOBO-DIC reconstruction of HAMOCC. This appears to be an artifact due to overfitting, that is not found in our reconstructions based on real observations.

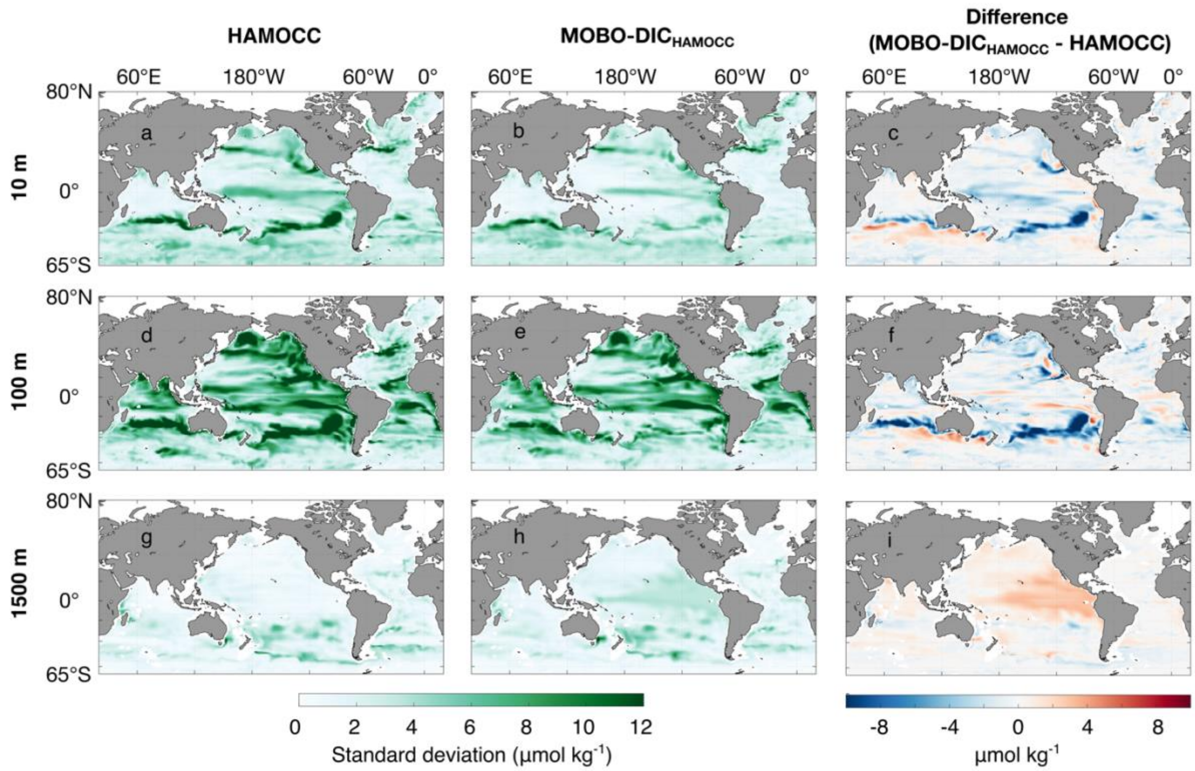

Figure S8: Spatial distribution of the interannual variability of sDIC, defined as the standard deviation in time (de-trended, seasonal cycle smoothed with a 12-month running mean) in HAMOCC (a,d,g), our MOBO-DIC reconstruction of HAMOCC with synthetic data (b,e,h), and the difference between the two (c,f,i) at 10 m (a-c), 100 m (d-f), and 1500 m (g-i).

S6.2 Independent time-series stations (BATS, HOT, Drake Passage)

DIC time-series stations are regularly visited sites, where measurements of DIC are taken. These data are independent from our mapping method, i.e., they are not used to create our data estimate, but provide a crucial basis to estimate how well our estimate compares to measured values. Independent time-series stations that overlap with our study domain and period include the Bermuda Atlantic Time-series Study (BATS; Bates et al., 2014), Hawaii Ocean Time-series (HOT; Dore et al., 2009), and Drake Passage (Munro et al., 2015). See Fig. S1 for the location of these stations.

While the in-situ observations display considerably more noise than our smooth monthly 1°x1° fields, we find that MOBO-DIC is close to the mean values at the time-series stations and captures some of the variability (Fig. S9). The RMSD between MOBO-DIC and the time-series stations range from 13 µmol kg^{-1} in the shallow waters at HOT to 42 µmol kg^{-1} at the surface of Drake Passage. Some observed values at the time-series stations seem to be outliers and may not be representative of the mean monthly field. For example, the large RMSD at Drake Passage can be at least partially attributed to some very low observed values (~200 µmol kg^{-1} lower than the mean). In addition, MOBO-DIC has a substantial offset in the deeper waters near BATS station, resulting in a large RMSD here too.

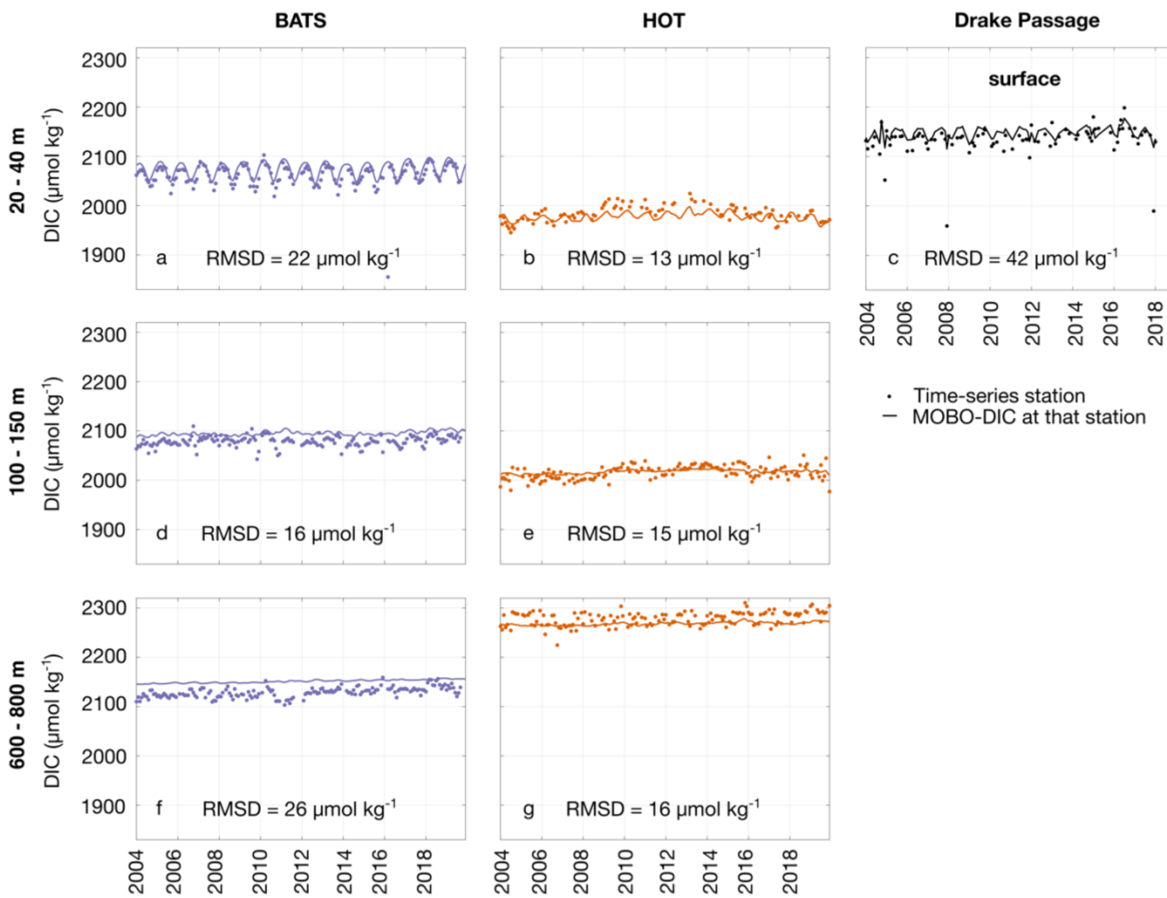

Figure S9: Timeline of DIC between 20 and 40 m (a-c), 100 and 150 m (e-g), and 600 and 800 m (h-j), BATS (a,d,f), HOT (b,e,g), and Drake Passage (surface only, c). Dots illustrate the direct measurements at these stations, solid lines show our MOBO-DIC estimate of DIC at the same month and 1°x1° grid point closest to the sites. RMSD between MOBO-DIC and the time-series stations is shown for each depth range and for each station as text. We chose to display averages over multiple depth levels here as the time-series data is often sparse at individual depth levels.

S6.3 DIC calculated from biogeochemical Argo float measurements (SOCCOM floats)

Argo floats equipped with biogeochemical sensors (BGC Argo floats) have been sampling the global ocean in recent years, supplementing the ship data (https://biogeochemical-argo.org/). They do not measure DIC directly, but several methods have been developed to estimate DIC based on the BGC float measurements of other variables. Some BGC Argo floats are equipped with pH sensors, but these floats are mostly confined to the Southern Ocean as part of the Southern Ocean Carbon and Climate Observations and Modeling project (SOCCOM, https://soccom.princeton.edu/). Here, we make use of DIC calculated based on the temperature, salinity, and pH measurements of the SOCCOM floats, in combination with the LIAR approach to estimate total alkalinity (Carter et al. 2018), and CO2SYS (Humphreys et al., 2020), available at https://soccompu.princeton.edu/www/index.html.

Our comparison with the float data shows that MOBO-DIC captures the variability in the Southern Ocean well (Fig. S10). The discrepancies that exist between MOBO-DIC and the float data can be partially explained by high frequency variability captured by the floats, that are not in our smooth 1°x1° monthly fields. In addition, in the region between the Polar Front (~55°S) and 65°S, our estimate of DIC at the time and location of the floats is substantially less than the DIC estimates by the floats, especially in the winter months (i.e., when the DIC concentrations exhibit the seasonal peak). This finding is in line with previous studies who found that SOCCOM floats report more outgassing (i.e., higher DIC concentrations) in this region in winter than ship-based estimates (Gray et al., 2018; Bushinsky et al., 2019). Notably, this known difference at the surface also exists in the interior (Fig. S10 f,i). However, the difference between the floats and our estimate south of the Polar Front (mean bias of ~8 µmol kg^{-1}) is well within the uncertainty of MOBO-DIC in this region (18 µmol kg^{-1}). Nonetheless, it confirms the known differences between float and ship-based estimates of DIC in this region and further research should be conducted to understand the processes behind that.

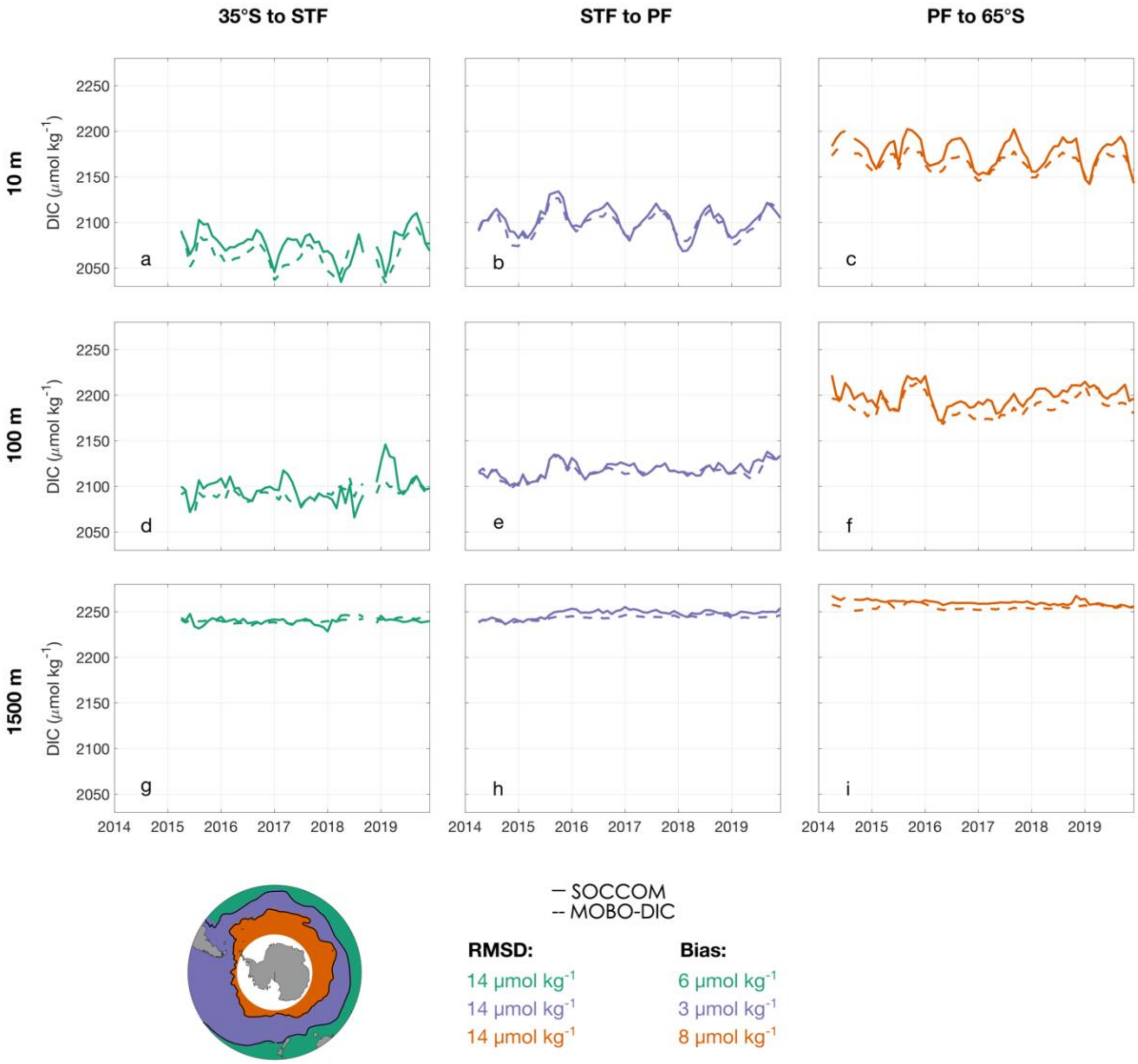

Figure S10: Timeline of mean DIC at 10 m (a-c), 100 m (d-f), and 1500 m (g-i), between 35° S and the Subtropical Front (STF, a,d,g), between the STF and the Polar Front (PF, b,e,h), and between the PF and 65° S (c,f,i). Solid lines illustrate the DIC estimated from the SOCCOM floats, dashed lines show our MOBO-DIC estimate at the same month and 1°x1° grid point closest to each float observation. The panel on the right displays the three interfrontal regions in green, purple, and orange from north to south. The fronts are based on Orsi et al. (1995).

S6.4 Global mapped surface DIC (OceanSODA-ETHZ)

To compare our estimate at a global scale, but restricted to the surface, we compare it to the surface DIC estimate OceanSODA-ETHZ by Gregor & Gruber (2021) at the time and location where the two datasets overlap (January 2004 to December 2018). The approach by Gregor & Gruber (2021) also uses a cluster-regression method with an ensemble of clusters; however, they only estimate surface values. In addition, the DIC in OceanSODA-ETHZ is not based on direct DIC measurements but is calculated based on their cluster-regression estimates of pH and total alkalinity using CO2SYS (Humphreys et al., 2020). Note that for the surface, we consider the shallowest depth level in MOBO-DIC (2.5 m), which is not at the actual surface. We do not normalize for salinity in this comparison, as their estimate uses a different salinity-product than ours.

Considering that the two estimates of DIC are based on independent datasets of measurements (SOCAT vs. GLODAP), their distribution of surface DIC compares well (Fig. S11). Overall, the global mean RMSD between the two data estimates is 15 µmol kg^{-1}, and a global mean bias of 4 µmol kg^{-1} (Fig. S11 a-c). The positive bias cannot be attributed to different periods, as here we only compare the overlap period from 2004 through 2018. A part of this bias could be linked to our shallowest depth being 2.5 m, and not the surface. Both the bias and the RMSD are, however, well within the sum of the uncertainty limits of the two datasets (21 and 18 µmol kg^{-1}, for OceanSODA-ETHZ and MOBO-DIC, respectively).

The trend (Fig. S11 d-f) and interannual variability (Fig. S11 g-i) in the two datasets are also encouragingly similar. The trend of MOBO-DIC at the surface is slightly less in most regions than the trend of the mapped surface DIC from Gregor & Gruber (2021), with global mean trends of 0.6 µmol $kg^{-1}yr^{-1}$ and 0.8 µmol $kg^{-1}yr^{-1}$, respectively (Fig. S11 d-f). The interannual variability of MOBO-DIC at the surface is also slightly smaller in most regions than the interannual variability in OceanSODA-ETHZ Gregor & Gruber (2021), with global mean standard deviations of 3 and 4 µmol kg^{-1}, respectively.

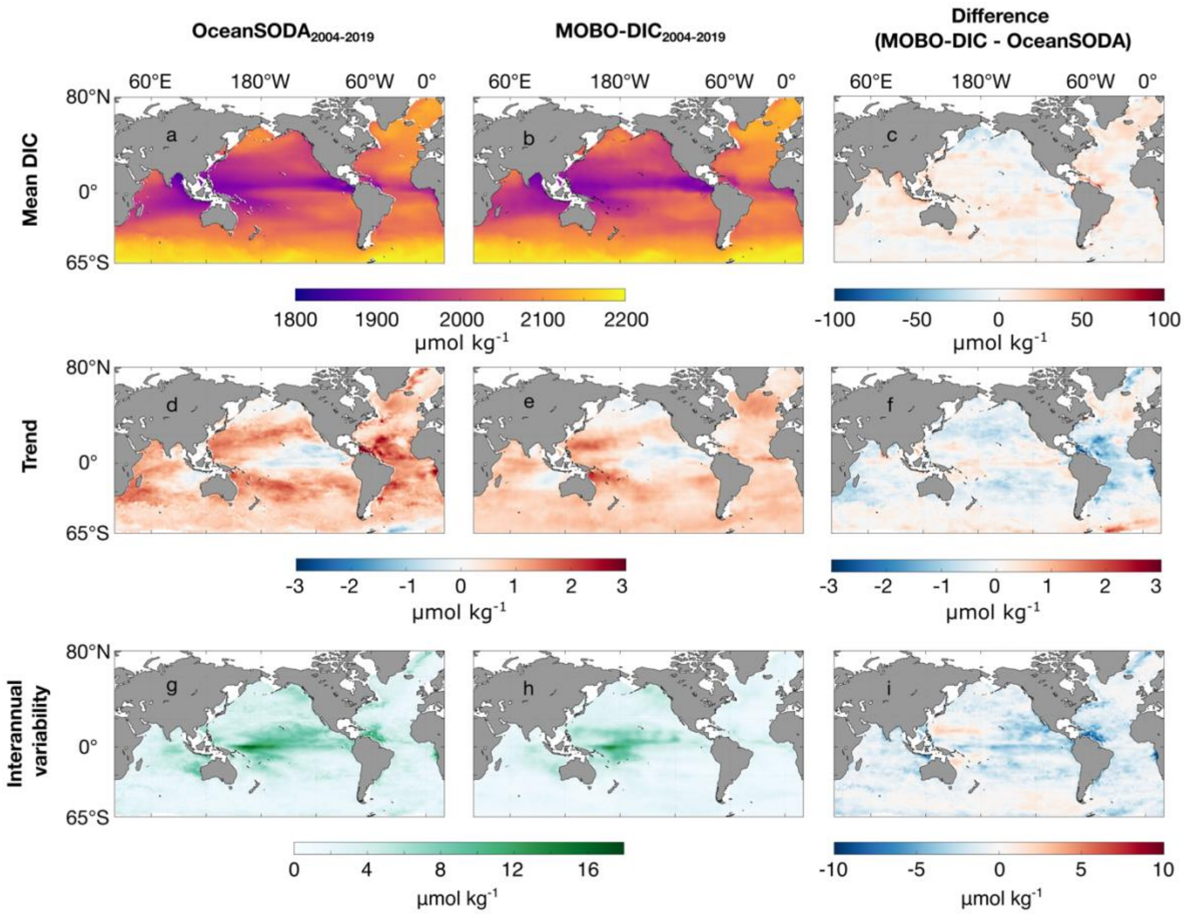

Figure S11: Mean (a-c), trend (d-f), and interannual variability (g-h) of surface DIC in OceanSODA-ETHZ (a,d,g) and MOBO-DIC at 2.5 m (b,e,h) from January 2004 to December 2018, and the difference between the two estimates (MOBO-DIC - OceanSODA-ETHZ; c,f,i).

S7 Trends in sDIC

We illustrate the vertically integrated trend in sDIC in Fig. 2a of the Main Text. Here, we demonstrate the trends on the individual depth levels (Fig. S12). We find that most of the observed negative trends are significant at the 95% confidence intervals, including some negative trends e.g., below the thermocline of the North Pacific.

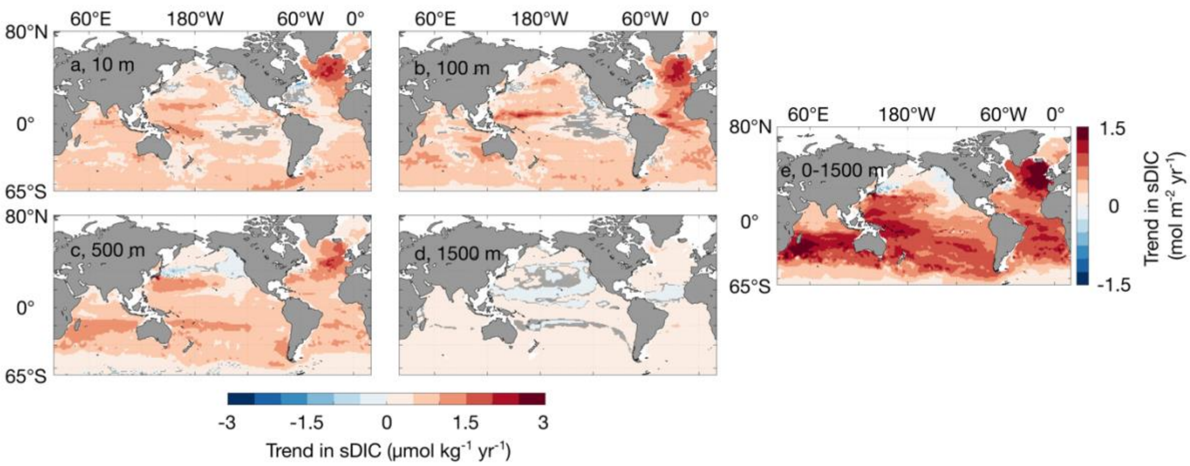

Figure S12: Maps of the trend in sDIC between 2004 and 2020 based on the linear trend at 10 m (a), 100 m (b), 500m (c), 1500 m (d), and vertically integrated over the upper 1500 m (e). In a-d, regions where the trends are not significant ($p<0.05$) are hatched. In e, we remove the trends that are not significant ($p<0.05$) before integrating.

S8 Interannual variability in the Western Equatorial Pacific

We find the largest interannual variations in sDIC below the thermocline in the Western Equatorial Pacific (here: 0.5°N to 14.5°N, 124.5°E to 179.5°E). Here, we compare the connection between the observed variations in sDIC in this region and natural climate variability, represented by the Multivariate El Niño Index (MEI; Wolter et al., 2011). During El Niño periods (positive MEI), the trade winds weaken, leading to less upwelling in the Peruvian Coastal Upwelling System (PCUS), the cold tongue in the eastern equatorial Pacific extends less far towards the west, while the warm pool in the Western Equatorial Pacific retracts eastward (Talley et al., 2011). Thus, overall sea surface temperatures tend to be warmer, and less DIC and nutrients are brought to the surface in the PCUS during El Niño periods. Concurrently, the slope of the thermocline, which has a west-east gradient across the equatorial Pacific flattens, resulting in a shallower mixed layer in the Western Equatorial Pacific. The opposite holds for La Niña periods, i.e., colder SSTs, more sDIC and nutrients in the PCUS, and a steeper slope of the thermocline.

Our results demonstrate a positive correlation between mean sDIC and MEI in the upper Western Equatorial Pacific. This correlation is moderate near the surface ($r = 0.41$ at 10 m), largest around the thermocline ($r = 0.85$ at 150 m) and decreases again below the thermocline ($r = 0.28$ at 500 m, Fig. S13). Temperature cannot be the dominant driver of this signal because the effect of decreased solubility of CO_2 would result in a negative correlation. Instead, the relationship between the sDIC in the water column of the Western Equatorial Pacific and MEI suggests that the shift in the thermocline is the dominant driver for the sDIC variations, in line with model studies from McKinley et al. (2004). The flattening of the thermocline during El Niño periods brings sDIC and nutrients stored at depth upward, explaining the strong positive correlation in the thermocline of this region. This effect diminishes with depth, and above the thermocline, the effect is reduced through outgassing and biological activity as proposed by Takahashi et al. (2002) and subsequent studies (e.g., Feely et al., 2006).

Compared to the signal in the Western Equatorial Pacific, we observe a smaller signal in the PCUS. It seems that here, opposing effects on the sDIC mostly cancel each other out, resulting in the weak interannual variability of sDIC in this region. Here, decreased upwelling during El Niño periods leads to less DIC being brought to the surface. Concurrently, less upwelled nutrients result in less biological uptake of DIC, and thus, more DIC remaining near the surface.

Our findings are consistent with the findings by McKinley et al. (2004), who used a global ocean general circulation model to link their model's variability of the air-sea CO_2 fluxes in the equatorial Pacific to ENSO-induced changes in the transport of DIC: the combined effects of the flattening of the thermocline, less upwelling, and the east-west displacement of the warm pool change how much DIC-rich water reaches the surface and affects the air-sea CO_2 fluxes. However, that study finds large variabilities across most longitudes of the equatorial Pacific, with the largest variations near the center and the east, compared to our study, where the largest variations are in the Western Equatorial Pacific. This may be linked to the recent westward shift of the El Niño phenomena also referred to as El Niño Modoki (Ashok et al., 2007).

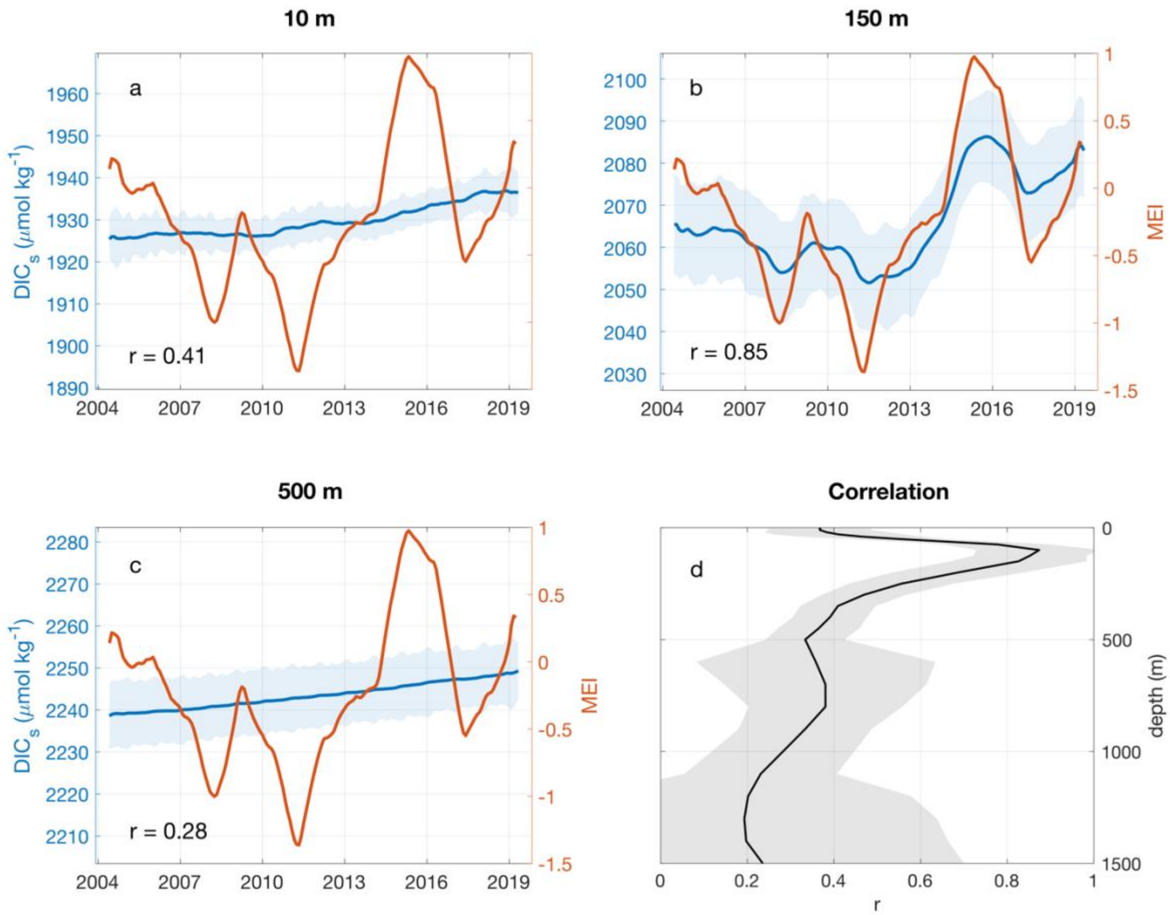

Figure S13: ENSO and sDIC in the Western Equatorial Pacific. Timelines of the mean sDIC in the western equatorial Pacific (left y-axis, blue) and the MEI (right y-axis, orange) at 10 m (a), 150 m (b), and 500 m (c) both sDIC and the MEI are smoothed with a 12-month moving average. The first and last 6 months are lost in the smoothing. The blue shading indicates the ensemble spread, i.e., the prediction uncertainty. Correlation coefficient r between sDIC in this region (seasonal cycle removed) and the MEI (seasonal cycle removed) as a function of depth (d). The correlation coefficient r between sDIC and the MEI is shown as text for each depth level in a-c.